uOttawa

L'Université canadienne
Canada's university

FACULTÉ DES ÉTUDES SUPÉRIEURES ET POSTOCTORALES

uOttawa

L'Université canadienne
Canada's university

FACULTY OF GRADUATE AND POSDOCTORAL STUDIES

Israel De Leon Arizpe

AUTEUR DE LA THÈSE / AUTHOR OF THESIS

M.A.Sc. (Electrical Engineering)

GRADE / DEGREE

School of Information Technology and Engineering

FACULTÉ, ÉCOLE, DÉPARTEMENT / FACULTY, SCHOOL, DEPARTMENT

Spectral domain analysis and application of reflection and refraction phenomena in two-dimensional dielectric periodic structures

TITRE DE LA THÈSE / TITLE OF THESIS

D. McNamara

DIRECTEUR (DIRECTRICE) DE LA THÈSE / THESIS SUPERVISOR

S. Roux

CO-DIRECTEUR (CO-DIRECTRICE) DE LA THÈSE / THESIS CO-SUPERVISOR

EXAMINATEURS (EXAMINATRICES) DE LA THÈSE / THESIS EXAMINERS

J. Albert

P. Berini

Gary W. Slater

LE DOYEN DE LA FACULTÉ DES ÉTUDES SUPÉRIEURES ET POSTDOCTORALES /
DEAN OF THE FACULTY OF GRADUATE AND POSTDOCORAL STUDIES

Spectral domain analysis and application of reflection and refraction phenomena in two-dimensional dielectric periodic structures

by

Israel De Leon Arizpe

A thesis submitted to the
Faculty of Graduate and Postdoctoral Studies
in partial fulfillment of the requirements for the degree of

Master of Applied Science
in Electrical Engineering

Ottawa-Carleton Institute for Electrical and Computer engineering
School of Information Technology and Engineering
Faculty of Engineering
University of Ottawa

September 2005

Your file Votre référence
ISBN: 0-494-11252-2
Our file Notre référence
ISBN: 0-494-11252-2

Abstract

This thesis is intended to contribute to an analytical understanding of refraction and reflection phenomena of monochromatic electromagnetic fields at the interface between homogeneous media and two-dimensional PhCs by studying the **k**-space (Fourier domain) representation of the refracted and reflected fields. The goal is to provide physical explanations of distortion effects experienced by the fields when interacting with the periodic medium, and to evaluate quantitatively such effects through the analysis of the fields' angular spectra.

The motivation for this investigation is the interesting reflection and refraction phenomena observed when light propagates across the interfaces between homogeneous dielectric regions and photonic crystals (PhCs), which is a situation often found in integrated optical systems. Such reflective and refractive phenomena play an important role in the operation of such systems.

In order to achieve the above goal a new method of analysis has been developed for studying the behavior of electromagnetic wave propagation in (and into) PhCs. A **k**-space picture of the PhC response to non-idealized finite-cross-section beams is made possible. The most important capability offered by this method is the ability to separate the field distribution into physically interpretable beams by employing useful Fourier techniques. This allows one to interpret the computed field's behavior in terms of physically meaningful incident, refracted and reflected beams. It also allows one to examine details such as beam distortion and the power carried by each of these beams. Particularly, one can obtain a clear understanding of the behavior of the field refracted into the PhC since it is possible to analyze independently the Fourier components of the refracted mode in both real space and **k**-space. The mathematical formulations that allow one to interpret the above-mentioned physical phenomena from the numerical solutions are given.

"Almighty God, Who hast created man in Thine own image and made him a living soul that he might seek after Thee and have dominion over Thy creatures, teach us to study the works of Thy hands that we may subdue the earth to our use and strengthen our reason for Thy service..."

– James Clerk Maxwell (1831-1879).

To my mother.

Acknowledgements

First and foremost I would like to express my sincere appreciation to my thesis advisor, Dr. F.S. (Stef) Roux, from whom I have learned so much. I thank Stef for his guidance and encouragement throughout my graduate studies, and for his patience and readiness while explaining complicated concepts. I am please to thank Stef for providing the financial support, without which part of my graduate work would not be possible.

I am deeply thankful to Dr. Derek McNamara, who kindly agreed to stand in for Dr. Roux when he left for the University of Pretoria, and for his valuable inputs to my research. I am also grateful to Dr. Sergey Loyka for providing the computer power, which made possible the achievement of the numerical results indispensable for the present research.

A special thank-you note goes to Pamela Qu, who kindly collaborated reading an initial draft of this thesis. I thank Pamela for her valuable comments regarding the redaction of this thesis.

I would like to thank my friends working in the electromagnetics laboratory: Paul Salem, Igor Acimovic, Dave McPhee, and Tan Quach for their critical comments regarding this work and for many hours of interesting conversations and fun non-research-related activities shared throughout my days in the University of Ottawa. I also thank Dave for taking care of my shoulder during the time I was injured.

Finally, I thank my parents, my sister Martha, and my brother David for being the source of strength and motivation that made all this possible. Thanks mother for your unconditional support and love that reinforced me to accomplish this thesis, which is fully devoted to you.

Contents

List of Figures

List of Tables

Publications

- I. De Leon and F.S. Roux, "Fourier analysis of reflection and refraction in two-dimensional photonic crystals," Phys. Rev. B, Vol. 71, 235105 (2005).
- The publication above was selected for the June 27, 2005 issue of the Virtual Journal of Nanoscale Science and Technology[1].

[1]The Virtual Journal, which is published by the American Institute of Physics and the American Physical Society in cooperation with numerous other societies and publishers, is an edited compilation of links to articles from participating publishers, covering a focused area of frontier research. You can access the Virtual Journal at http://www.vjnano.org.

Acronyms and abbreviations

2-D	Two-dimensional
3-D	Three-dimensional
BZ	Brillouin zone
1BZ	First Brillouin zone
EFC	Equifrequency contour
HAZ	Harmonic annular zone
1HAZ	First Harmonic annular zone
2HAZ	Second Harmonic annular zone
FDTD	Finite difference time domain
FFT	Fast Fourier transform
PhC	Photonic crystal
PWE	Plane-wave expansion
TE	Transverse electric
TM	Transverse magnetic

Chapter 1

Introduction

1.1 Photonic crystals

Media with periodically varying material properties, such as the refractive index, are well known for their ability to control the propagation of electromagnetic waves over specific frequency ranges. When the periodicity of the medium is on the order of optical wavelengths, these artificial composite structures receive the name of *photonic crystals* (PhCs). The control of electromagnetic radiation is restricted to the plane(s) of periodicity. Therefore, one often refers to these structures as one-, two-, or three-dimensional PhCs in accordance with the number of spatial dimensions in which the periodicity has been introduced[1]. By adequate selection of the PhC parameters, i.e., lattice geometry, periodicity scale, and refractive index, a range of forbidden frequencies in the electromagnetic dispersion relation will appear. It is referred to as the *photonic band gap*. Indispensable conditions, yet not sufficient, for the presence of a photonic band gap are strong refractive index modulation and periodicity scale on the order of the wavelength.

[1]There is a fairly extensive existing body of literature on the use of one- and two-dimensional periodic structures for applications in the microwave frequency regime, stretching from 1950's to the present. A brief review is given in Ref. [1]. However, in such applications, three-dimensional structures and two-dimensional structures periodic in the direction of propagation do not appear to have been considered.

The first complete treatment of electromagnetic waves in three-dimensional periodic dielectric structures with large refractive index modulation was formulated by Ohtaka [2], in 1979, as an extension of the KKR (Korringa-Kohn-Rokester) method [3, 4] using vector-spherical wave expansions. However, it was only after the seminal publications of Yablonovitch [5] and John [6], in 1987, that the control of electromagnetic radiation through three-dimensional periodically modulated dielectric media became popular. In his publication, Yablonovitch proposed the idea of inhibited spontaneous emission of electromagnetic waves through the photonic band gap of a three-dimensional PhC as an alternative to improve the efficiency of semiconductor lasers; John, on the other hand, demonstrated the existence of localized electromagnetic modes in certain disordered periodic structures. These publications triggered the investigation of photons in strongly modulated periodic media as an analogy to electrons in crystalline solids. Since then, researchers in diverse fields of classical electromagnetics, solid-state physics, optics, and materials science have been contributing significantly to the understanding of novel phenomena in such structures.

Early investigations in PhCs were focused on potential applications based on the inhibition of electromagnetic states. Indeed, an important property of PhCs is the emergence of localized modes in the frequency range of the photonic band gap when deliberate disorders are introduced to their periodicity. A line-defect introduced in the periodicity of a PhC provides a versatile mechanism of light-propagation control when operated at frequencies in the gap. This concept changed the paradigm of light guidance through the so-called PhC waveguides, which have demonstrated the possibility of guiding light through sharp bends [7, 8, 9]. Moreover, ultrahigh-Q PhC resonant cavities can be designed by introducing point-defects in the structure; they have been used to construct add-drop filters [10] and low-threshold lasers sources [11].

It was after the publications of Lin [12] and Kosaka [13] in 1996 and 1998, respectively, that a new exciting area of research was opened through the study of light refraction in PhCs. In his publication, Lin proposed a PhC-based prism, which provides high frequency sensitivity and compact size for frequencies in the infrared-visible regime;

Kosaka, on the other hand, reported the observation of extraordinary angle-sensitive refraction in a three-dimensional PhC, which is found as a consequence of the highly anisotropic properties of the periodic medium. The refraction phenomenon in PhC has been actively investigated since then, uncovering interesting effects. For example, a PhC can be designed to operate as a homogeneous left-handed medium, in which electromagnetic waves are refracted negatively [14, 15]. A recent investigation [16] has proposed that a slab of such a medium can amplify evanescent waves through resonant coupling mechanisms of surface-bounded electromagnetic states, suggesting the possibility to create super-lenses capable of reproducing a monochromatic image with subwavelength resolution [17]. Another interesting phenomenon is the super-collimation effect [18], which limits the divergence of light beams and serves as an efficient mechanism of light guidance in particular directions.

The difficulties in fabricating fully three-dimensional PhCs have led researchers to explore potential applications of two-dimensional PhC-slabs, which can be fabricated with the lithographic techniques presently used in microelectronics. The two-dimensional approach provides full control of electromagnetic propagation in the periodic plane, while it confines the waves in the transverse direction by means of total internal reflection. Two-dimensional PhC-slabs have been shown to be excellent candidates for integrated optics applications [11, 19, 20, 21].

It is the purpose of this thesis to investigate the refraction and reflection of monochromatic electromagnetic fields at the interface between homogeneous media and two-dimensional PhCs by studying the angular spectra of the refracted and reflected fields. The main goal of this work is to provide physical explanations of distortion effects experienced by the fields when interacting with the periodic medium, and to evaluate quantitatively such effects through the analysis of the fields' angular spectra.

1.2 Thesis organization

The remainder of this thesis is organized as follows. Chapter 2 gives the basic theoretical concepts of electromagnetic wave propagation in PhCs. It discusses the general properties of the wave equations and the characteristics of the natural modes in periodic media. It also gives insights into anomalous refraction phenomena analyzed in later chapters. Chapter 3 provides a derivation for the mathematical expression of the angular spectra of arbitrary monochromatic field distributions in PhCs. Such an expression is used to support the results generated in the following chapters. In Chapter 4, a novel method of analysis is developed to study the angular spectra of arbitrary monochromatic field distributions in periodic media. The method is employed in this chapter to describe the process of obtaining the reflectance and transmittance at the interface between a PhC and a homogeneous dielectric. Chapter 5 applies the fundamental ideas discussed in Chapters 3 and 4 to study the reflection and refraction of electromagnetic waves at the interface between homogeneous media and PhCs. Two-dimensional semi-infinite PhCs with hexagonal- and square-lattice geometries are considered in the analysis. Anomalous refraction phenomena such as negative refraction and super-collimation are studied in detail. In Chapter 6, the method of analysis is employed to characterize the performance of a PhC device. The proposed device is a PhC-based beam shifter, whose objective is to translate the beam axis of the incident beam to a different position. Quantitative results of power efficiency and beam distortion are given as a result of the analysis. The overall conclusions of this work are given in Chapter 7.

Chapter 2

Principles of photonic crystals

This chapter introduces the main mathematical tools and physical concepts that support the theory of electromagnetic wave propagation in dielectric periodic media, namely PhCs. The properties of electromagnetic waves in PhCs are exposed and described using the fundamental concepts in the band theory of crystalline solids [22]. The discussion is concentrated on the two-dimensional case. However, the concepts can be extended to three dimensions straightforwardly.

2.1 Periodic dielectric media: basic concepts

The periodic arrangement of dielectric scatterers that form a PhC resembles the atomic structure of crystalline solids. It is therefore convenient to define the structural parameters of PhCs using the concepts of crystal lattices. Thus, a PhC is regarded as a lattice of scatterers, which play the role of the atoms in the analogy with crystalline solids.

2.1.1 Real space and Bravais lattice

The mathematical domain that describes the position of the "atoms" over a space is called the *real space*. It is defined in two dimensions by the position vector $\mathbf{r} = x\hat{\mathbf{x}} + y\hat{\mathbf{y}}$.

The periodic array in which the "atoms" are arranged in the real space is described by the concept of the *Bravais lattice.* For a two-dimensional space, the Bravais lattice consists of an infinite set of points with position vectors given by

$$\mathbf{R} = \sum_{\sigma=1}^{2} p_\sigma \mathbf{a}_\sigma, \tag{2.1}$$

where $\mathbf{a}_\sigma$ are the *primitive vectors*, and p_σ are integers. Hence, it defines a set of points that remain invariant under translation through any vector $\mathbf{R}$, and so it is said to have *translational symmetry.* The Bravais lattice in the real space is called the *direct lattice*, and the vectors $\mathbf{R}$ that form it are often referred to as the *direct lattice vectors.* The distance between points in the direct lattice is called the *lattice constant*, and it is denoted by the letter a.

The area of space that, when translated from one point of the Bravais lattice to the points next to it, does not overlap or leave voids is called the *primitive cell.* There is not a unique way to choose the shape of the primitive cell; yet, its area is always given by $A = \mathbf{a}_1 \cdot (\mathbf{a}_2 \times \hat{\mathbf{z}})$. A particular choice of the primitive cell is the *Wigner-Seitz cell.* It consists of the region generated by bisecting the translation vector from a particular point of the Bravais lattice to the nearest adjacent points. The Wigner-Seitz cell has the symmetry of the Bravais lattice and it is, in general, the most widely used choice of the primitive cell.

2.1.2 Reciprocal space and reciprocal lattice

The *reciprocal space* is related to the real space by the Fourier transform. It describes a function in terms of its wave vector, $\mathbf{k}$. Hence, it also receives the name of $\mathbf{k}$-*space.*

The *reciprocal lattice* is also a Bravais lattice. It consists of the set of wave vectors, $\mathbf{G}$, that satisfy the relation $\exp(j\mathbf{G} \cdot \mathbf{R}) = 1$, for any direct lattice vector, $\mathbf{R}$. Or equivalently, $\mathbf{G} \cdot \mathbf{R} = 2\pi p$, where p is an integer. The reciprocal lattice can be defined as a linear combination of basis vectors in the following form

$$\mathbf{G} = \sum_{\sigma=1}^{2} q_\sigma \mathbf{g}_\sigma, \tag{2.2}$$

where q_σ are integers. The vectors $\mathbf{g}_\sigma$ are called the primitive vectors of the reciprocal lattice. The set of primitive vectors can be generated from the direct lattice as [22]

$$\mathbf{g_1} = \frac{2\pi}{A}\,(\mathbf{a_2} \times \hat{\mathbf{z}})\,,\;\mathbf{g_2} = \frac{2\pi}{A}\,(\hat{\mathbf{z}} \times \mathbf{a_1})\,, \tag{2.3}$$

where $\mathbf{a}_\sigma$ $(\sigma = 1, 2)$ are the primitive vectors of the direct lattice, and A is the area of the primitive cell of the direct lattice.

2.1.3 Brillouin zones

Brillouin zones are regions in the reciprocal space defined by the *Bragg planes* of reciprocal lattice. Bragg planes are perpendicular bisectors of the lines formed by the reciprocal lattice vectors, $\mathbf{G}$. The *first Brillouin zone* (1BZ) is defined to be the Wigner-Seitz cell of the reciprocal lattice centered at the origin. It consists of the set of points in $\mathbf{k}$-space that can be reached from the origin without crossing any Bragg plane. The 1BZs of the hexagonal and square reciprocal lattices, are shown in bold in Figs. 2.1(a) and 2.1(b), respectively. Particularly, the 1BZ is important because it defines the primitive cell of the reciprocal lattice. The 1BZ can be further reduced by symmetry to the so-called *irreducible Brillouin zone*, which is represented by the shaded region in Figs. 2.1(a) and 2.1(b). The symmetry points of the 1BZ are thus given by the vertices of the irreducible BZ. They are designated by the symbols Γ, M, K for the hexagonal lattice; and Γ, M, X, for the square lattice as illustrated in the figure.

In general, the n-th Brillouin zone is formed by the set of points in the $\mathbf{k}$-space that can be reached from the origin by crossing $n-1$ Bragg planes, but no fewer. Examples of the first few Brillouin zones for the two-dimensional square and hexagonal lattices are illustrated in Appendix B.

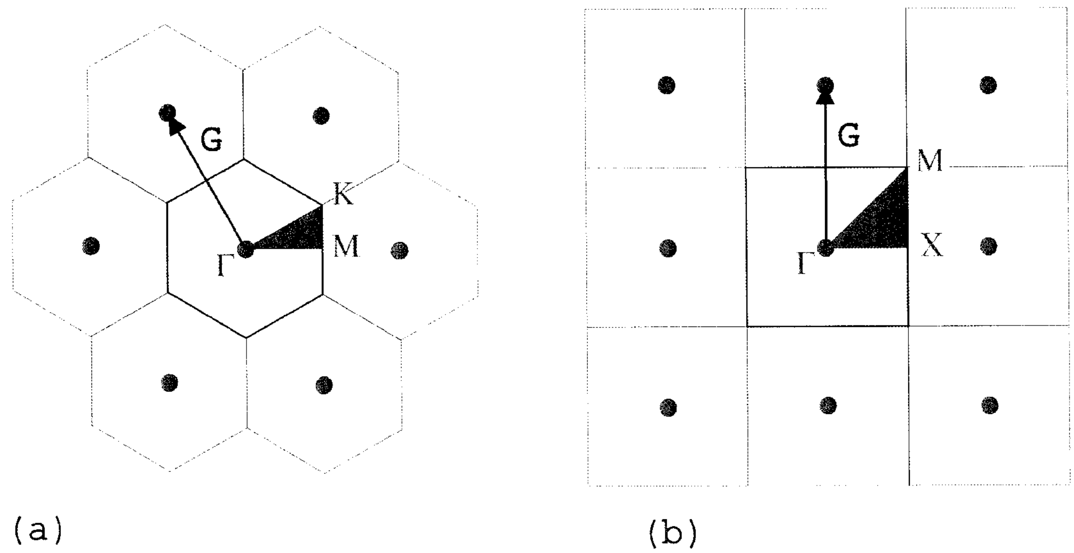

Figure 2.1: The (a) hexagonal and (b) square reciprocal lattices. The first Brillouin zone for each lattice is shown in bold with their respective symmetry points labeled. The Wigner-Seitz primitive cell is shown replicated at every point **G**. The shaded regions indicate the irreducible Brillouin zone for each lattice.

2.1.4 Dielectric function

The position-dependent relative permittivity of a PhC is denoted by the *dielectric function* $\epsilon(\mathbf{r})$, which is a periodic function. It is convenient to define this periodic function in terms of a Bravais lattice as

$$\epsilon(\mathbf{r}+\mathbf{R}) = \epsilon(\mathbf{r}), \tag{2.4}$$

where $\mathbf{R}$ denotes the direct lattice vectors and $\mathbf{r}$ is the position vector. Furthermore, we shall find it useful to represent the inverse dielectric function $(\epsilon^{-1}(\mathbf{r}))$ in terms of a "plane-wave" basis. For this, we obtain its Fourier transform, or $\mathbf{k}$-space representation,

$$\hat{\epsilon}(\mathbf{k}) = \int \epsilon^{-1}(\mathbf{r}) \exp(-j\mathbf{k}\cdot\mathbf{r})\, d^2\mathbf{r}, \tag{2.5}$$

which is also a periodic function with the periodicity of the Bravais lattice. Thus, $\hat{\epsilon}(\mathbf{k})$ also has translational symmetry under vectors $\mathbf{R}$, i.e.,

$$\hat{\epsilon}(\mathbf{k}) = \hat{\epsilon}(\mathbf{k}) \exp(j\mathbf{k}\cdot\mathbf{R}). \tag{2.6}$$

For Eq. (2.6) to hold, the exponential term must equal unity or the function $\hat{\epsilon}(\mathbf{k})$ must be zero. For a non-trivial dielectric function, this means that $\hat{\epsilon}(\mathbf{k})$ is zero everywhere except at those points $\mathbf{k}$ where $\exp(j\mathbf{k}\cdot\mathbf{R}) = 1$, which are the points of the reciprocal lattice. The inverse dielectric function is therefore represented in terms of its $\mathbf{k}$-space analogue as the Fourier series

$$\epsilon^{-1}(\mathbf{r}) = \sum_{\mathbf{G}} \hat{\epsilon}(\mathbf{G}) \exp(j\mathbf{G}\cdot\mathbf{r}), \tag{2.7}$$

where the summation is over all the vectors $\mathbf{G}$ in the reciprocal lattice.

2.2 Wave equations

The properties of electromagnetic fields are governed by Maxwell's equations. In a linear and non-magnetic dielectric medium, Maxwell's equations in (cgs) units for the source-free case are given by

$$\begin{aligned}
\nabla\times\mathbf{E}(\mathbf{r},t) &= -\frac{1}{c}\frac{\partial\mathbf{H}(\mathbf{r},t)}{\partial t} && (2.8)\\
\nabla\times\mathbf{H}(\mathbf{r},t) &= \frac{1}{c}\epsilon(\mathbf{r})\frac{\partial\mathbf{E}(\mathbf{r},t)}{\partial t} && (2.9)\\
\nabla\cdot\mathbf{E}(\mathbf{r},t) &= 0 && (2.10)\\
\nabla\cdot\mathbf{H}(\mathbf{r},t) &= 0 && (2.11)
\end{aligned}$$

where c is the speed of light in vacuum and the functions $\mathbf{E}(\mathbf{r},t)$ and $\mathbf{H}(\mathbf{r},t)$ describe, respectively, the time-dependent distribution of the electric and magnetic vector fields. Combining Maxwell's equations (2.8-2.11) to eliminate $\mathbf{H}(\mathbf{r},t)$ in Eq. (2.8), or $\mathbf{E}(\mathbf{r},t)$

in Eq. (2.9), one obtains the following wave equations:

$$\begin{aligned}\frac{1}{\epsilon(\mathbf{r})}\nabla\times\nabla\times\mathbf{E}(\mathbf{r},t)+\frac{1}{c^2}\frac{\partial^2\mathbf{E}(\mathbf{r},t)}{\partial^2 t} &= 0\\ \nabla\times\frac{1}{\epsilon(\mathbf{r})}\nabla\times\mathbf{H}(\mathbf{r},t)+\frac{1}{c^2}\frac{\partial^2\mathbf{H}(\mathbf{r},t)}{\partial^2 t} &= 0\end{aligned} \tag{2.12}$$

2.2.1 Eigenvalue problem and Bloch eigenmodes

For the time harmonic case we seek for solutions of the form $\mathbf{F}(\mathbf{r},t)=\mathbf{F}(\mathbf{r})\exp(-j\omega t)$, where ω is the angular frequency and $\mathbf{F}(\mathbf{r})$ is the complex field distribution of either the electric field, $\mathbf{E}$, or the magnetic field, $\mathbf{H}$. From Eqs. (2.12), one can readily see that the functions $\mathbf{F}(\mathbf{r})$ satisfy the following eigenvalue equations:

$$\mathcal{L}_e\mathbf{E}^{(n)}(\mathbf{r})\equiv\left\{\frac{1}{\epsilon(\mathbf{r})}\nabla\times\nabla\times\right\}\mathbf{E}^{(n)}(\mathbf{r})=\left(\frac{\omega_n}{c}\right)^2\mathbf{E}^{(n)}(\mathbf{r}) \tag{2.13}$$

$$\mathcal{L}_h\mathbf{H}^{(n)}(\mathbf{r})\equiv\left\{\nabla\times\frac{1}{\epsilon(\mathbf{r})}\nabla\times\right\}\mathbf{H}^{(n)}(\mathbf{r})=\left(\frac{\omega_n}{c}\right)^2\mathbf{H}^{(n)}(\mathbf{r}), \tag{2.14}$$

with eigenvalues $(\omega_n/c)^2$ and eigenfunctions $\mathbf{E}^{(n)}(\mathbf{r})$ and $\mathbf{H}^{(n)}(\mathbf{r})$, respectively. The differential operators $\mathcal{L}_e$ and $\mathcal{L}_h$ are defined by the terms between brackets.

When the dielectric function $\epsilon(\mathbf{r})$ is periodic, *Bloch's Theorem* states that the solutions of the wave equations (2.13, 2.14) have the form of a plane wave multiplied by a periodic function with the periodicity of the Bravais lattice,

$$\mathbf{F}^{(n)}(\mathbf{r};\mathbf{k}')=\mathbf{u}^{(n)}(\mathbf{r};\mathbf{k}')\exp(j\mathbf{k}'\cdot\mathbf{r}), \tag{2.15}$$

where $\mathbf{u}^{(n)}(\cdot)$ is a periodic function. These eigenfunctions represent the natural modes in a periodic medium. They receive the name of *Bloch modes*. Each Bloch mode is associated with a particular wave vector $\mathbf{k}'$, which is called the *Bloch vector* and is restricted to the 1BZ[1]. For a given Bloch vector, the solutions of the wave equations (2.13, 2.14) form an infinite set of discrete values. Each element in the solution set is

[1]The proof is given at the end of Section 2.2.3

denoted by the superscript (n).

In general, the characteristics of the periodic function, $\mathbf{u}^{(n)}(\cdot)$, also depend on the Bloch vector, and so it is explicitly indicated as one of its arguments. Furthermore, because it has the periodicity of the Bravais lattice, the function has translational symmetry, i.e.,

$$\mathbf{u}^{(n)}(\mathbf{r};\mathbf{k}') = \mathbf{u}^{(n)}(\mathbf{r}+\mathbf{R};\mathbf{k}'). \tag{2.16}$$

2.2.2 Orthogonality properties of the wave equations

It can be shown that the differential operator, $\mathcal{L}_h$, in the wave equation (2.14) is Hermitian [23]. Consequently, the magnetic-field eigenproblem has two important properties: (1) the eigenfrequencies, $\omega_n(\mathbf{k})$, must be real; (2) the resulting eigenfunctions form a complete set of orthogonal functions under the inner product

$$\langle \mathbf{P}(\mathbf{r}), \mathbf{Q}(\mathbf{r})\rangle = \int_{\mathcal{S}} \mathbf{P}(\mathbf{r}) \cdot \mathbf{Q}^*(\mathbf{r}) d^2\mathbf{r}, \tag{2.17}$$

where $\mathbf{P}(\mathbf{r})$ and $\mathbf{Q}(\mathbf{r})$ are complex vectorial functions, $*$ denotes complex conjugate, and $\mathcal{S}$ is the two-dimensional region where the two vectorial functions exist. From the second property, it follows that the magnetic-field eigenfunctions satisfy the expression

$$\left\langle \mathbf{H}^{(n)}(\mathbf{r};\mathbf{k}), \mathbf{H}^{(m)}(\mathbf{r};\mathbf{k}')\right\rangle = \delta(\mathbf{k}-\mathbf{k}')\delta_{n,m}, \tag{2.18}$$

where $\delta(\cdot)$ is the Dirac delta function and $\delta_{n,m}$ is the Kronecker delta function. The previous expression holds for all indices n and m, as well as all wave vectors $\mathbf{k}$ and $\mathbf{k}'$ in the 1BZ. Hence, any solution of the wave equation (2.14) can be expressed as a linear combination of its eigenfunctions.

On the other hand, the operator $\mathcal{L}_e$ in the wave equation (2.13), is not Hermitian. Hence, the eigenfunctions of the electric-field eigenproblem are not necessarily orthogonal [23]. However, Bloch modes are intrinsically orthogonal to each other if their Bloch vectors are different (see Appendix A). It follows that the electric-field eigenfunctions satisfy the expression

$$\left\langle \mathbf{E}^{(n)}(\mathbf{r};\mathbf{k}), \mathbf{E}^{(m)}(\mathbf{r};\mathbf{k}')\right\rangle = A^{(n,m)}(\mathbf{k},\mathbf{k}')\delta(\mathbf{k}-\mathbf{k}'), \tag{2.19}$$

where $A^{(n,m)}(\mathbf{k},\mathbf{k}')$ is a vectorial function, which is, in general, different than zero. Hence, provided that $\mathbf{k} \neq \mathbf{k}'$, any solution of the wave equation (2.13) can be expressed as a linear combination of its eigenfunctions.

2.2.3 Bloch space-harmonics

The Bloch wave in Eq. (2.15) can be expanded in terms of a continuous plane-wave basis. For this purpose, we represent its periodic part as

$$\mathbf{u}^{(n)}(\mathbf{r};\mathbf{k}') = \int \mathbf{U}^{(n)}(\mathbf{k};\mathbf{k}')\exp(j\mathbf{k}\cdot\mathbf{r})\, d^2\mathbf{k}, \tag{2.20}$$

where $\mathbf{U}^{(n)}(\mathbf{k};\mathbf{k}')$ is the Fourier transform of $\mathbf{u}^{(n)}(\mathbf{r};\mathbf{k}')$, and the integration is over the entire $\mathbf{k}$-space. Then we notice that, because the periodic function has translational symmetry, the previous equation can be written as follows:

$$\mathbf{u}^{(n)}(\mathbf{r};\mathbf{k}') = \sum_{\mathbf{G}} \mathbf{U}^{(n)}(\mathbf{G};\mathbf{k}')\exp(j\mathbf{G}\cdot\mathbf{r})\,. \tag{2.21}$$

Then, using Eq. (2.15) and defining $\mathbf{U}_{\mathbf{G}}^{(n)}(\mathbf{k}') \equiv \mathbf{U}^{(n)}(\mathbf{G};\mathbf{k}')$, we can express the Bloch mode as

$$\mathbf{F}^{(n)}(\mathbf{r};\mathbf{k}') = \sum_{\mathbf{G}} \mathbf{U}_{\mathbf{G}}^{(n)}(\mathbf{k}')\exp\left[\, j\,(\mathbf{k}'+\mathbf{G})\cdot\mathbf{r}\right]. \tag{2.22}$$

Hence, a Bloch mode consists of an infinite number of plane waves with wave vectors of the form $\mathbf{k}_{\mathbf{G}} = \mathbf{k}' + \mathbf{G}$ and complex amplitudes given by their respective Fourier-coefficient functions, $\mathbf{U}_{\mathbf{G}}^{(n)}(\mathbf{k})$. These plane waves are referred to as the *Bloch space-harmonics*.

Consider now a generic wave vector of the form $\mathbf{k} = \mathbf{k}' + \mathbf{G}'$, where $\mathbf{k}'$ is in the 1BZ, and $\mathbf{G}'$ is a particular reciprocal lattice vector. From Eq. (2.22), the Bloch mode associated with such a wave vector takes the form

$$\begin{aligned}\mathbf{F}^{(n)}(\mathbf{r};\mathbf{k}) &= \sum_{\mathbf{G}} \mathbf{U}^{(n)}_{\mathbf{G}+\mathbf{G}'}(\mathbf{k}')\exp\left[\,j\,(\mathbf{k}'+\mathbf{G}'+\mathbf{G})\cdot\mathbf{r}\right]\\ &= \sum_{\mathbf{G}-\mathbf{G}'} \mathbf{U}^{(n)}_{\mathbf{G}}(\mathbf{k}')\exp\left[\,j\,(\mathbf{k}'+\mathbf{G})\cdot\mathbf{r}\right].\end{aligned} \tag{2.23}$$

The second line follows after redefining $\mathbf{G}+\mathbf{G}'\to\mathbf{G}$. Thus, because $\mathbf{G}$ is an infinite set of vectors, the previous expression equals Eq. (2.22), indicating that a Bloch mode is entirely defined by a wave vector within the 1BZ – the Bloch vector.

2.2.4 TE/TM Bloch modes

In the two-dimensional case, we shall restrict the wave propagation to the (x, y)-plane. In such a case, either the electric vector, $\mathbf{E}$, or the magnetic vector, $\mathbf{H}$, lies completely in the propagation plane, forcing the polarization of the other vector field to be in the z-direction. In the PhC context, polarization with the $\mathbf{E}$ field in the propagation plane is called *transverse electric* (TE) because the electric field is transverse to the homogeneous direction. On the other hand, polarization with the $\mathbf{H}$ field in the propagation plane is called *transverse magnetic* (TM).

For a TE- or TM-polarized electromagnetic field, one can always obtain the field distribution of the transverse components from the z-polarized field. It is therefore convenient to consider the problem in terms of a scalar field, which has the form

$$F_z^{(n)}(\mathbf{r};\mathbf{k}') = u^{(n)}(\mathbf{r};\mathbf{k}')\exp(j\mathbf{k}'\cdot\mathbf{r}), \tag{2.24}$$

where $u^{(n)}(\cdot) = |\mathbf{u}^{(n)}(\cdot)|$ as defined in Eq. (2.16) and F_z represents either the scalar electric field, E_z, for a TM-polarized field, or the scalar magnetic field, H_z, for a TE-polarized field. Equivalently, the scalar Bloch wave can be expressed in terms of a plane-wave basis as

$$F_z^{(n)}(\mathbf{r};\mathbf{k}') = \sum_{\mathbf{G}} U_{\mathbf{G}}^{(n)}(\mathbf{k}')\exp\left[\, j\,(\mathbf{k}'+\mathbf{G})\cdot\mathbf{r}\right], \tag{2.25}$$

where $U_{\mathbf{G}}^{(n)}(\mathbf{k}') = |\mathbf{U}_{\mathbf{G}}^{(n)}(\mathbf{k}')|$ as defined in Eq. (2.22).

2.2.5 Plane-wave expansion

The *plane-wave expansion* (PWE) formalism consists of expressing Eq. (2.13) or (2.14) in terms of a plane-wave basis, in order to obtain a linear system of equations for the unknown eigenvalues and eigenfunctions. From Section 2.1.4, the plane-wave expansion of the inverse dielectric function is given by Eq. (2.7). In addition, from Eq. (2.25), the plane-wave expansion for the TM-polarized electric field and TE-polarized magnetic field of a Bloch mode are, respectively, given by

$$E_z^{(n)}(\mathbf{r};\mathbf{k}') = \sum_{\mathbf{G}} E_{\mathbf{G}}^{(n)}(\mathbf{k}')\exp\left[\, j\,(\mathbf{k}'+\mathbf{G})\cdot\mathbf{r}\right] \tag{2.26}$$

$$H_z^{(n)}(\mathbf{r};\mathbf{k}') = \sum_{\mathbf{G}} H_{\mathbf{G}}^{(n)}(\mathbf{k}')\exp\left[\, j\,(\mathbf{k}'+\mathbf{G})\cdot\mathbf{r}\right]. \tag{2.27}$$

Substituting Eqs. (2.26) and (2.7) into the wave equation (2.13), one obtains an infinite linear system of homogeneous equations for the electric-field eigenfunctions. It is given by

$$\sum_{\mathbf{G}'} \left\{\hat{\epsilon}(\mathbf{G}-\mathbf{G}')\,|\mathbf{G}'+\mathbf{k}|^2\right\} E_{\mathbf{G}'}^{(n)}(\mathbf{k}) = \left(\frac{\omega_n(\mathbf{k})}{c}\right)^2 E_{\mathbf{G}}^{(n)}(\mathbf{k}). \tag{2.28}$$

A similar system of equations for the magnetic-field eigenfunctions results from substituting Eqs. (2.27) and (2.7) into the wave equation (2.14). It reads

$$\sum_{\mathbf{G}'} \left\{\hat{\epsilon}(\mathbf{G}-\mathbf{G}')\,[\mathbf{G}+\mathbf{k}]\cdot[\mathbf{G}'+\mathbf{k}]\right\} H_{\mathbf{G}'}^{(n)}(\mathbf{k}) = \left(\frac{\omega_n(\mathbf{k})}{c}\right)^2 H_{\mathbf{G}}^{(n)}(\mathbf{k}). \tag{2.29}$$

By truncating the number of reciprocal lattice vectors in the two previous expressions, one can find the fields inside the periodic medium from a linear algebra eigenvalue problem over the 1BZ. It can be solved through standard eigen-decomposition, with the square matrix entries defined by the terms between brackets. The resulting eigenvalues, $[\omega_n(\mathbf{k})/c]^2$, and eigenfunctions, $[E_{\mathbf{G}}^{(n)}(\mathbf{k}), H_{\mathbf{G}}^{(n)}(\mathbf{k})]$, are discrete sets of functions that vary continuously with $\mathbf{k}$. Each function in the solution sets is labeled by the index n.

The PWE method is the workhorse for obtaining the PhC's dispersion relations. However, it is known that its accuracy diminishes when the amplitude of the spatial variation of the dielectric constant is large [24, 25]. In turn, different proposals were made recently in order to improve its convergence [26, 27, 28, 29]. Particularly, the methodology proposed by Guo [29] is employed for PWE calculations in this work. This technique reduces the computation time and improves the accuracy by obtaining analytically the Fourier transform of the dielectric-function unit cell (provided that the 'atoms' have regular shape). Hence, there is no need to use the numerical FFT routine and one can avoid the step of dividing the space into small grids.

2.2.6 Photonic band structure

The discrete set of functions described by the eigenvalues of the wave equations (2.13, 2.14), determine the dispersion relations of the PhC, i.e., $\omega = \omega_n(\mathbf{k})$. From the continuum of frequencies, only those values in the solution set can exist inside the PhC; the rest are forbidden. Thus, the functions $\omega_n(\mathbf{k})$ form a discrete set of n frequency bands, which define the structure of the allowed modes. It receives the name of *photonic band structure* in analogy to the electronic band structure of crystalline solids.

In general, the photonic band structure may present bands separated by a range of forbidden frequencies [30], which is referred to as the *photonic band gap.* For this frequency range, mode propagation is restricted in all directions, and so it is said to be a *full band gap.* Nonetheless, for some other frequencies, mode propagation may be restricted only for specific wave vectors. In such a case, one talks about a *partial band* *gap* [31].

The photonic band structure is often computed for wave vectors within the 1BZ, since the Bloch vector is limited to this region of the **k**-space. This representation is said to be in the *reduced zone scheme*. However, in some particular cases, it is necessary to emphasize the periodicity of the dispersion relations by representing the band structure over a larger range of wave vectors covering several primitive cells. Such a representation is said to be in the *repeated zone scheme*.

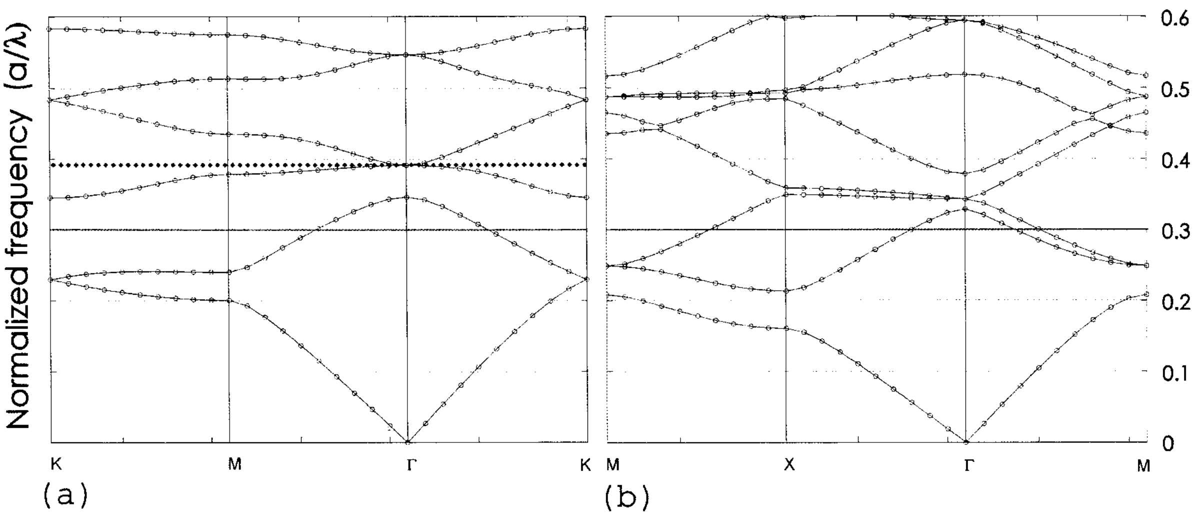

Figure 2.2: Photonic band structures of two infinite 2-D PhCs composed of air holes of radius $0.4a$ etched in a background dielectric with refractive index $n_b = 3.6$. (a) Hexagonal-lattice geometry – dotted line denotes the frequency where bands 3 and 4 degenerate at the Γ point. (b) Square-lattice geometry – solid line denotes a frequency where bands 2 and 3 overlap.

At particular frequencies some band structures can present *overlapping bands*. This is when the excited Bloch modes are associated with more than one frequency band for a single operation frequency. A special case of band overlapping occurs at *degenerate eigenfrequencies*, where two or more frequency bands present identical eigenfrequencies for the same Bloch vector.

The photonic band structures in Fig. 2.2(a) and 2.2(b) correspond, respectively, to hexagonal- and square-lattice PhCs. Their structural parameters are described in the figure's caption. Both band structures are shown in the reduced zone scheme for wave vectors along contour of the irreducible Brillouin zone. The vertical frequency axis is given in normalized units, defined as

$$\tilde{f} = \frac{a\omega}{2\pi c} = \frac{a}{\lambda},$$

where a is the lattice constant and λ is the wavelength in vacuum. The horizontal dotted line in Fig. 2.2(a) indicates the frequency at which the third and fourth bands degenerate at the point Γ. On the other hand, the horizontal solid line in Fig. 2.2(b) shows the case when the second and third bands overlap.

2.3 Refraction and reflection

Waves refracted from a homogeneous medium into a PhC must match their tangential wave vector components at the interface between the two media with those of the incident and reflected waves. This phenomenon is often referred to as the *tangential wave vector conservation condition* ($\mathbf{k}_{||}-$*conservation condition*). The perpendicular component of the wave vectors on both sides of the interface is then dictated by the contours of constant frequency of the dispersion relation in the corresponding medium [32].

In a two-dimensional, homogeneous, and isotropic medium the contour of constant frequency describes a circle of radius $k = 2\pi/\lambda$, the wave number. We will refer to this circle as the **k**-*shell.* It denotes all possible propagating wave vectors at the particular frequency. Hence, propagating waves satisfy the *shell condition*

$$k^2 = k_x^2 + k_y^2. \tag{2.30}$$

In a two-dimensional PhC, on the other hand, the contours of constant frequency are obtained from the photonic band structure by solving the equation

$$\omega_n(\mathbf{k}) = \omega_0, \qquad \omega_0 = constant, \tag{2.31}$$

independently for every frequency band, n. The solutions of Eq. (2.31) are also called the *equifrequency contours* (EFCs), and they describe the propagating Bloch modes allowed for the specific frequency ω_0. Consider for example Fig. 2.3(a) and 2.3(b), which show the three-dimensional representation of the photonic band structures in Fig. 2.2(a) and 2.2(b), respectively. They give the values of $\omega_n(\mathbf{k})$ for all the wave vectors within the 1BZ. The constant frequency planes in both band structures indicate the frequency $a/\lambda = 0.3$, or equivalently $\omega_0 = 0.6\pi$. Therefore, the values of $\omega_n(\mathbf{k})$ that intersect the constant frequency plane in each band structure give the respective EFC at ω_0.

The propagation direction and velocity of the electromagnetic energy carried by a wave is given by the energy velocity vector $\mathbf{v}_e$. In homogeneous media this quantity equals the group velocity vector [33], which is defined as the gradient of the dispersion curve, i.e.,

$$\mathbf{v}_g = \nabla_{\mathbf{k}}\omega(\mathbf{k}). \tag{2.32}$$

It can be shown that in a lossless periodic medium, the relation $\mathbf{v}_g = \mathbf{v}_e$ also holds; the mathematical proof is given in [32]. Hence, the propagation direction of a monochromatic wave refracted into a PhC is given by the direction of the vector $\mathbf{v}_g$. From

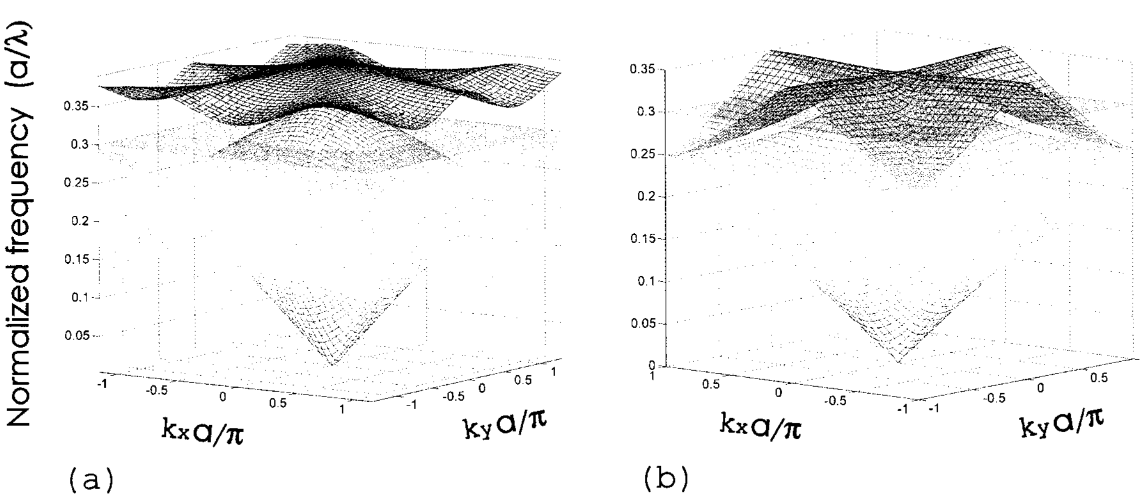

Figure 2.3: Three-dimensional representation of the photonic band structures shown in (a) Fig. 2.2(a) and (b) Fig. 2.2(b). The constant planes represent the constant frequency $a/\lambda = 0.3$.

Eq. (2.32), it follows that $\mathbf{v}_g$ is a vector perpendicular to the EFC; its magnitude is given by the slope of the dispersion curve evaluated at the particular frequency and Bloch vector, and its direction points toward the direction of positive rate of frequency increase.

An intuitive way to visualize the refraction phenomenon is given in Fig. 2.4(a) and 2.4(b), which show, respectively, the EFCs at the frequency $a/\lambda = 0.3$ associated with the photonic band structures in Fig. 2.3(a) and 2.3(b). In addition, the figures show a homogeneous medium **k**-shell at the same frequency; the orientation of the interface between the homogeneous and periodic media is indicated by the vertical dashed line. For a given wave incident from the homogeneous medium, one can easily determine the direction of the refracted Bloch wave – given by $\mathbf{v}_g(\mathbf{k})$ – simply by tracing the $\mathbf{k}_{||}$-conservation line (horizontal dotted lines) on the diagrams in Fig. 2.4. For example, consider the case for the wave vector $\mathbf{k}_2$ in Fig. 2.4(a). The wave vector represents a wave in the homogeneous medium propagating from left to right with an angle of approximately 15° with respect to the k_x axis. The wave is refracted into the PhC, and hence, the tangential components of the incident and refracted wave vectors must match at the k_y value indicated by the $\mathbf{k}_{||}$-conservation line. The direction of the refracted wave is then given by a vector perpendicular to the EFC at the point intersected by the $\mathbf{k}_{||}$-conservation line. In this case, the vector $\mathbf{v}_g$ points towards the inside of the EFC because the second frequency band has a maximum at the Γ point, which is located at the center of the EFC. This indicates that the positive rate of frequency increase is in the direction toward the inside of the EFC. Notice that, for any case, there are two possible solutions for the group velocity vector because the $\mathbf{k}_{||}$-conservation line always cuts the EFC at two points. One must always choose the solution that gives a refracted-wave propagation direction moving away from the incident wave because the other solution is not physically possible.

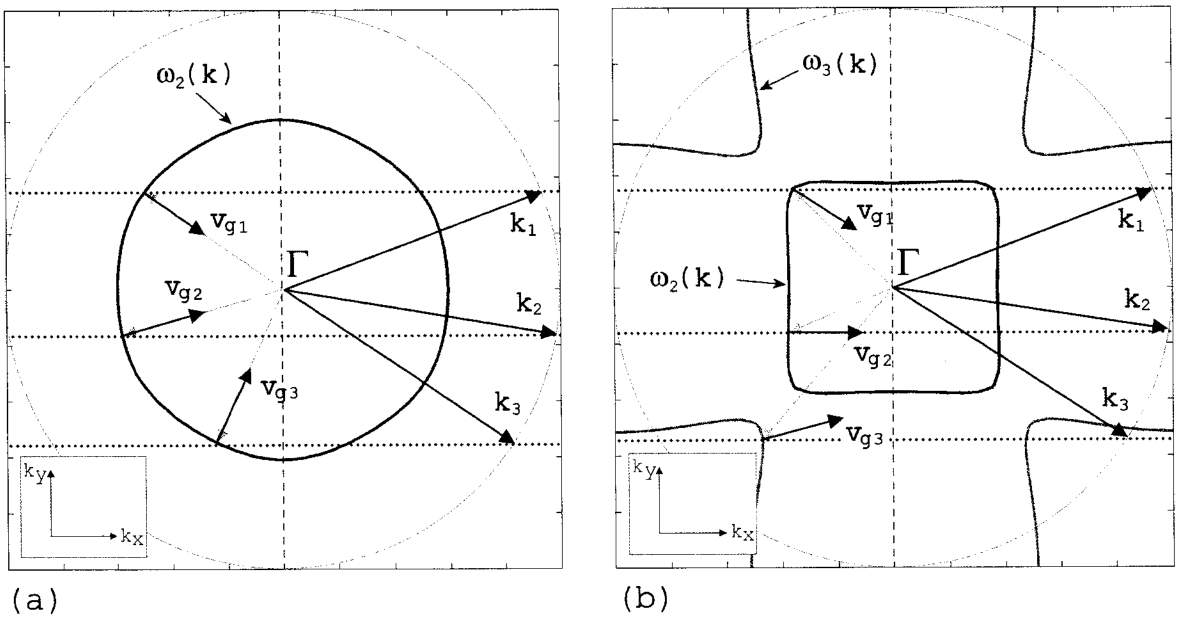

Figure 2.4: The **k**-space representation of the refraction process of three waves, $\mathbf{k}_1$, $\mathbf{k}_2$, and $\mathbf{k}_3$, incident from a homogeneous medium into (a) a hexagonal-lattice PhC and (b) a square-lattice PhC at the frequency $a/\lambda = 0.3$. The EFCs are shown in the reduced zone scheme. The thin circle in both figures represents the **k**-shell and the vertical dashed lines indicate the interface orientation.

2.3.1 Anomalous refraction

We already mentioned how the refracted-wave's propagation direction depends on the EFC at the operation frequency. In what follows we address a number of interesting anomalous-refraction phenomena observed in PhCs due to the large anisotropy generally presented by the EFC.

Negative refraction

The dispersion relations of a PhC may present negative slopes at some points of specific frequency bands. For instance, the second band in Fig. 2.3(a) resembles a negative parabola centered at the Γ point. For such cases, it follows from Eq. (2.32) that $\mathbf{v}_g$ points towards the inside of the EFC, being opposite to the case observed for normal dispersion. It is thereby said that the group velocity is *negative*. Hence, a positive slope about a point in the frequency band (the magnitude of the Bloch vector increases as the frequency increases) implies positive group velocity, while a negative slope (the magnitude of the Bloch vector decreases as the frequency increases) implies negative group velocity.

Under certain conditions, a negative group velocity implies a *negative refraction* phenomenon. This phenomenon is studied extensively by Notomi in Ref. [14]. In this publication, Notomi shows that a PhC can resemble a homogeneous medium with negative refractive index, which is obtained when the EFC is circular and the group velocity is negative. In such a medium, $\mathbf{v}_g$ points towards the inside of the isotropic EFC, being anti-parallel to the Bloch vector. This case is illustrated in Fig. 2.4(a). At the same time, these two conditions, namely circular EFC and negative group velocity, imply left-handed (LH) behavior [15], which is denoted by the relation

$$\mathbf{v}_g \cdot \mathbf{k}' \equiv \mathbf{v}_e \cdot \mathbf{k}' < 0, \tag{2.33}$$

where $\mathbf{k}'$ is the Bloch vector. If Eq. (2.33) does not hold, then the medium is said to be right-handed (RH). For the anisotropic case, on the other hand, $\mathbf{v}_g$ and $\mathbf{k}'$ are not anti-parallel (see for example Fig. 2.4(b) for the case $\mathbf{k}_1$). In such a case, Eq. (2.33) is not obvious, and hence, it is necessary to compute the scalar product numerically in order to determine whether the system is right-handed or left-handed. Alternatively, one can determine the 'rightness' of the system by following the procedure in Ref. [15].

Negative refraction can also be achieved with positive group velocity, i.e., $\mathbf{v}_g$ pointing towards the outside of the EFC. Yet, from Eq. (2.33) it is obvious that LH behavior is not possible for this case. In this case, the phenomenon is rather the result of a strong anisotropy in the EFC [34]. An example of negative refraction with positive group velocity (and hence RH behavior) is shown in Fig. 2.4(b) for the $\mathbf{k}_3$ case.

Beam steering and super-collimation

In general, the EFC can be highly anisotropic, as with the case shown in Fig. 2.4(b). This property results in *beam steering* [35], which is the manipulation of the energy propagation direction, based on the EFC shape. The phenomenon is illustrated in Fig. 2.4(b), which shows the different directions taken by $\mathbf{v}_g(\mathbf{k})$ as a consequence of the anisotropic EFC. The energy propagation direction can also be controlled by changing the operation frequency in such a way that, for a fixed angle of incidence, the EFC modifies its shape, affecting the direction of $\mathbf{v}_g$. This phenomenon is called the *super-prism effect* [36].

A case of particular importance in Fig. 2.4(b) is denoted by the wave vector $\mathbf{k}_2$. This phenomenon is referred to as the *super-collimation* effect [18, 37] and involves limiting the beam divergence in PhCs by means of a straight EFC shape. A PhC operated under super-collimation conditions can serve as an efficient waveguide that provides clean transmission over a particular direction [35]. Furthermore, efficient light coupling [38], sharp bends with nearly perfect efficiency, and optical splitters [39] have been proposed for guiding light in different directions through the super-collimation mechanism.

2.3.2 Grating-like reflection

Several reflected waves might be generated when a wave impinges onto the PhC interface from a homogeneous medium. The different reflected waves are often referred to as *backward-diffraction orders* or just diffraction orders, because they follow a similar behavior than in a diffraction grating device [40, 41]. Backward diffraction arises because at the interface between the two media, the tangential wave vectors of the Bloch space-harmonics must match similar wave vectors in the homogeneous medium. Hence, each diffraction order satisfies the $\mathbf{k}_{||}-$conservation condition

$$\mathbf{k}_{q,||}^{(r)} = \mathbf{k}'_{||} + \mathbf{G}_{q,||}, \tag{2.34}$$

where q indexes the different diffraction orders, $\mathbf{k}_{q,||}^{(r)}$ is the tangential wave vector component of the q-th diffraction order, and $\mathbf{k}'_{||} + \mathbf{G}_{q,||}$ defines the tangential wave vector component of Bloch-space harmonics with common tangential reciprocal lattice vector,

$\mathbf{G}_{q,||}$.

In general, not all the diffracted orders represent propagating waves for the magnitude of the vectors $\mathbf{k}_{q,||}^{(r)}$ can be larger than the wave number in the homogeneous medium; hence, such wave vectors do not satisfy the shell condition.

2.3.3 Evanescent waves

Evanescent waves exist in the vicinity of the interface between a homogeneous medium and a PhC in order to satisfy the boundary conditions that cannot be fulfilled by propagating waves. On the homogenous side of the interface, they are generated by Bloch-space harmonics with tangential wave vectors that do not satisfy the shell-condition, Eq. (2.30). Hence, they are represented in the $\mathbf{k}$-space by points located off the $\mathbf{k}$-shell. Furthermore, because the tangential wave vector component must be conserved across the interface, it follows from Eq. (2.30) that the resulting wave vectors in the homogeneous medium have perpendicular components with imaginary magnitudes, given by

$$|\mathbf{k}_{q,\perp}| = j\sqrt{|\mathbf{k}_{q,||}|^2 - k^2}, \qquad |\mathbf{k}_{q,||}| > k, \tag{2.35}$$

where $\mathbf{k}_{q,||}$ represents the tangential wave vector component of Bloch-space harmonics with common tangential reciprocal lattice vector, and k is the wave number in the homogeneous medium.

Similarly, on the periodic side of the interface, evanescent waves are generated by plane waves in the homogeneous medium that are unable to match their tangential wave vectors with similar vectors of propagating Bloch modes. Consequently, their wave vectors define points in the $\mathbf{k}$-space located off the EFCs. As for the case in the homogeneous medium, the wave vectors of evanescent waves inside periodic media are complex [42]. These complex wave vectors can be obtained numerically by employing the complex band structure technique [43], which is widely used in surface physics of crystalline solids [44, 45, 46].

Chapter 3

Derivation of expression for angular spectra of Bloch modes

This chapter studies the mathematical expression for the angular spectra of arbitrary monochromatic fields inside PhCs. A derivation for such an expression is given in terms of the Fourier-coefficient function, which represents the Fourier components of Bloch-modes in a particular PhC. This function is obtained numerically by employing the PWE method previously described in Chapter 2.

3.1 Fourier-coefficient function

Consider a two-dimensional periodic medium characterized by the dielectric function $\epsilon(\mathbf{r}) = \epsilon(\mathbf{r} + \mathbf{R})$ for every $\mathbf{R}$ in the Bravais lattice. The scalar component of a electromagnetic field in such a medium, restricted to the n-th frequency band, is given by Eq. (2.22) as

$$\psi^{(n)}(\mathbf{r}; \mathbf{k}) = \sum_{\mathbf{G}} U_{\mathbf{G}}^{(n)}(\mathbf{k}) \exp\left[\, j\,(\mathbf{k} + \mathbf{G}) \cdot \mathbf{r}\right], \tag{3.1}$$

where ψ is either E_z for TM-polarizations or H_z for TE-polarizations; $\mathbf{k}$ are the field's Bloch vectors, which are limited to the 1BZ; and $U_{\mathbf{G}}^{(n)}(\mathbf{k})$ is the Fourier-coefficient function associated with modes in the n-th frequency band.

The domain of the Fourier-coefficient functions is defined for values of $\mathbf{k}$ within the 1BZ, and for every point $\mathbf{G}$ in the reciprocal lattice. One can combine these Fourier-coefficient functions into a continuous function in the entire $\mathbf{k}$-space, by shifting them to their respective reciprocal primitive cells

$$U^{(n)}(\mathbf{k}) = \sum_{\mathbf{G}} U_{\mathbf{G}}^{(n)}(\mathbf{k} - \mathbf{G}). \tag{3.2}$$

Since the $U_{\mathbf{G}}^{(n)}(\mathbf{k})$ functions are zero outside of the 1BZ, their shifted versions do not overlap. The resulting combined Fourier-coefficient function, $U^{(n)}(\mathbf{k})$, represents the Fourier spectra of all the Bloch modes in the n-th frequency band.

3.2 Bloch mode expansion

The angular spectra of an arbitrary monochromatic field can be expressed in terms of the Fourier-coefficient function, $U^{(n)}(\mathbf{k})$. For this, we expand the field in terms of Bloch modes,

$$\begin{aligned} \psi^{(n)}(\mathbf{r}) &= \int_{1\mathrm{BZ}} \alpha^{(n)}(\mathbf{k}')\psi^{(n)}(\mathbf{r};\mathbf{k}')d\mathbf{k}' \\ &= \int_{1\mathrm{BZ}} \sum_{\mathbf{G}} \alpha^{(n)}(\mathbf{k}')U_{\mathbf{G}}^{(n)}(\mathbf{k}') \exp\left[j(\mathbf{G}+\mathbf{k}')\cdot\mathbf{r}\right] d\mathbf{k}', \end{aligned} \tag{3.3}$$

where $\alpha^{(n)}(\mathbf{k})$ is the Bloch-coefficient function that represents the complex amplitudes of the excited Bloch modes in the n-th frequency band. The angular spectra (spatial Fourier transform) of such a field is given by

$$\begin{aligned} \Psi^{(n)}(\mathbf{k}) &= \int_{1\mathrm{BZ}} \sum_{\mathbf{G}} \alpha^{(n)}(\mathbf{k}')U_{\mathbf{G}}^{(n)}(\mathbf{k}')\delta\left[\mathbf{k}-(\mathbf{G}+\mathbf{k}')\right] d\mathbf{k}' \\ &= \sum_{\mathbf{G}} \alpha^{(n)}(\mathbf{k}-\mathbf{G})U_{\mathbf{G}}^{(n)}(\mathbf{k}-\mathbf{G}) \\ &= \sum_{\mathbf{G}} \alpha^{(n)}(\mathbf{k}-\mathbf{G}) \sum_{\mathbf{G}} U_{\mathbf{G}}^{(n)}(\mathbf{k}-\mathbf{G}) \\ &= \alpha_p^{(n)}(\mathbf{k})U^{(n)}(\mathbf{k}). \end{aligned} \tag{3.4}$$

The third line follows from the second line because both $\alpha^{(n)}(\mathbf{k})$ and $U_{\mathbf{G}}^{(n)}(\mathbf{k})$ are only nonzero inside the 1BZ. The periodic Bloch-coefficient function,

$$\alpha_p^{(n)}(\mathbf{k}) = \sum_{\mathbf{G}} \alpha^{(n)}(\mathbf{k}-\mathbf{G}), \tag{3.5}$$

is formed by duplicating $\alpha(\mathbf{k})$, which is zero outside the 1BZ, in every primitive cell over the entire $\mathbf{k}$-space. Furthermore, for the general case, one must take into account all the bands that overlap at the operation frequency in order to represent the complete angular spectra, i.e.,

$$\Psi(\mathbf{k}) = \sum_n \alpha_p^{(n)}(\mathbf{k}) U^{(n)}(\mathbf{k}), \tag{3.6}$$

where n represents the band number of the frequency bands that overlap at the operation frequency.

At this point, we shall stress that since the electric-field eigenproblem defined in Eq. (2.28) is not Hermitian, its eigenfunctions (Fourier-coefficient functions) are not necessarily orthogonal to each other. Hence, caution must be taken when representing the electric field angular spectra with Eq. (3.6), since it is valid only when Bloch modes in different overlapping bands have distinct Bloch vectors (see Section 2.2.2). Specifically, this thesis studies the electric field of monochromatic TM-polarized waves. Further analyses are therefore limited to cases with no overlapping bands and overlapping bands with non-degenerate eigenfrequencies in order to avoid non-orthogonality.

From Eq. (3.6) one can conclude that the angular spectra of an arbitrary monochromatic field distribution inside a PhC can be expressed as the product of a periodic Bloch-coefficient function $\alpha_p^{(n)}(\mathbf{k})$, which is unique for every specific field distribution, and the Fourier coefficient function $U^{(n)}(\mathbf{k})$, which is determined by the PhC but not by the particular field distribution.

3.3 Fourier-coefficient function for the square and hexagonal lattices

We now consider two particular PhCs with important geometries: the square lattice and the hexagonal lattice. Both PhCs consist of air holes of radius $0.4a$ etched in a background dielectric with refractive index $n_b = 3.6$. We will use these two structures in the following chapters and study the fields inside them through the **k**-space analysis. It is therefore convenient to review the properties of their respective Fourier-coefficient functions.

The Fourier-coefficient function, $U^{(n)}(\mathbf{k})$, was computed for a TM-polarized electric field (E_z) for several bands. For this, we employed the PWE method described in Section 2.2.5. The magnitude of the functions obtained for the first three frequency bands are shown in Figs. 3.1(a), 3.1(b), and 3.1(c) for the hexagonal lattice and in Figs. 3.1(d), 3.1(e), and 3.1(f) for the square lattice. The primitive cells of the reciprocal lattice are shown superimposed on the figures. From these results, one can observe that the amplitudes of the Fourier coefficients for the first band, $U^{(1)}(\mathbf{k})$, are concentrated inside the 1BZ, while those in the second and third bands are mostly concentrated in the annular band of primitive cells neighboring the 1BZ. From here on, this group of primitive cells will be referred to as the *first harmonic annular zone* (1HAZ), the subsequent annular bands of primitive cells will be referred to as the *second harmonic annular zone* (2HAZ), and so forth. In particular, the amplitudes located in the 1HAZ follow closely the shape of the n-th Brillouin zone, where n indicates the band number[1]. The amplitudes peak inside the n-th BZ, decrease rapidly at the edges, and become very weak outside n-th BZ. However, one can notice that the magnitudes gradually spread out of the n-th BZ for higher frequency bands.

The magnitude of the Fourier-coefficient functions associated with the fourth and fifth bands are shown in Figs. 3.2(a) and 3.2(b) for the hexagonal lattice and in 3.2(c) and Figs. 3.2(d) for the square lattice. For these cases, although the peak amplitudes

[1]Refer to Appendix B for Brillouin zone maps.

are located in the n-th BZ, other significant amplitudes are also located outside it. In fact, one can notice for the hexagonal lattice that significant amplitudes extend over large areas that cover almost completely the 1HAZ. The amplitude variations are more abrupt for the square-lattice and the significant amplitudes rather extend over the BZs neighboring the n-th BZ. Yet, even though the significant amplitudes are distributed over broader regions than in the first three frequency bands, they all are predominantly located in the 1HAZ.

The shape and slopes of the Fourier-coefficient function play an important role in the behavior of Bloch waves. This phenomenon will be discussed in Chapter 5.

3.4 Minimum Bloch mode wavelength

Whenever one employs numerical techniques to perform a real-domain analysis of the fields inside a PhC, such fields must be sampled well below the shortest wavelength in order to obtain accurate results. It is thus necessary to know the shortest wavelength inside the periodic medium.

From the results in Figs. 3.1 and 3.2, one can approximate the shortest wavelength of a specific Bloch mode, which is deduced by the shortest wavelength of its Bloch space-harmonics. Particularly, for the two structures under analysis, the first five bands always concentrate significant spectral amplitudes in the 1HAZ, predominantly. Thus, over this range of frequencies, the shortest wavelength can be approximated by

$$\lambda_{min} \approx \frac{2\pi}{|\mathbf{k}' + \mathbf{G}_{1\mathrm{HAZ}}|}, \tag{3.7}$$

where $\mathbf{k}'$ is the Bloch vector and $\mathbf{G}_{1\mathrm{HAZ}}$ is the reciprocal lattice vector pointing to the center of one of the primitive cells forming the 1HAZ.

Furthermore, it was found that for frequencies in the first five bands the term $|\mathbf{k}' + \mathbf{G}_{1\mathrm{HAZ}}|$ is always less than the wave number of a plane wave in the unpatterned background dielectric (homogeneous background dielectric), and that these two quan-

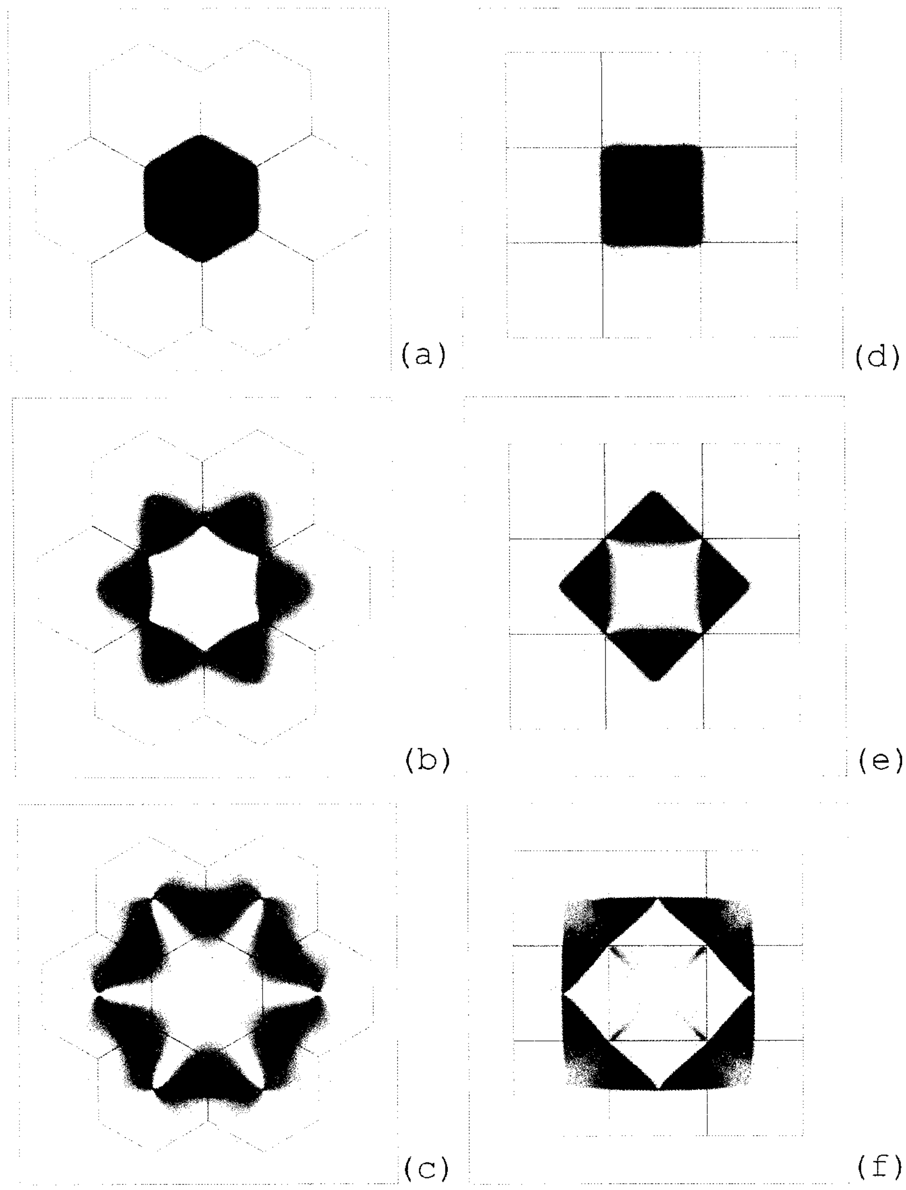

Figure 3.1: Fourier-coefficient functions for the (a) first, (b) second, and (c) third frequency bands of the TM-mode electric field in a 2-D hexagonal-lattice PhC; and for the (d) first, (e) second, and (f) third frequency bands in a 2-D square-lattice PhC. The structures are composed of air holes of radius $r = 0.4a$ etched in a background dielectric with refractive index $n_b = 3.6$.

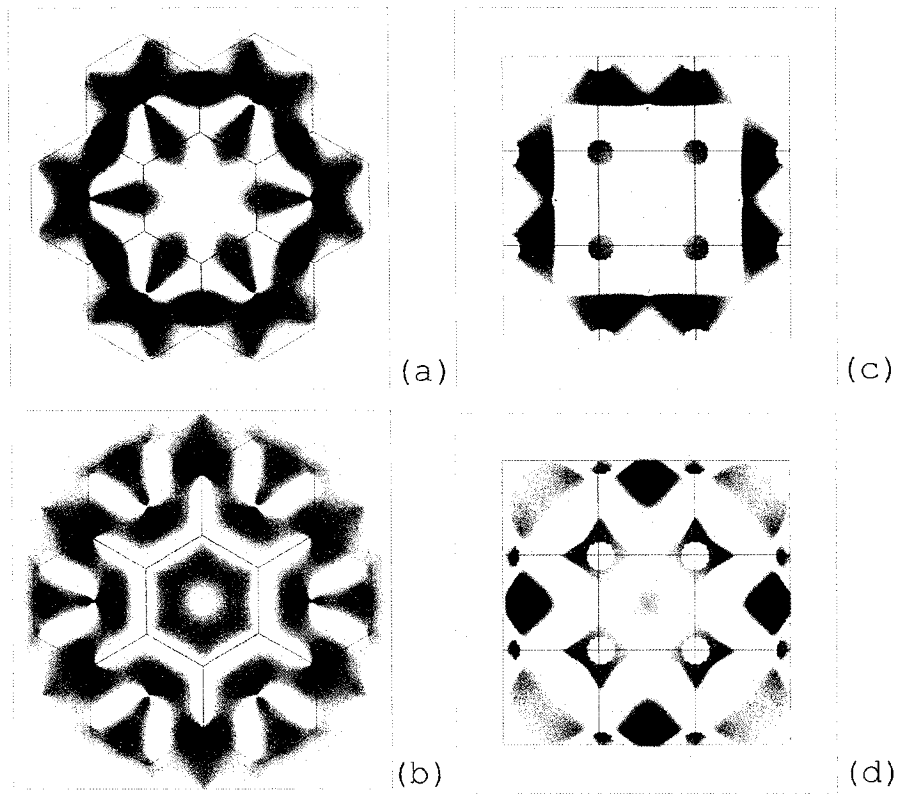

Figure 3.2: Fourier-coefficient functions for the (a) fourth and (b) fifth frequency bands of the TM-mode electric field in a 2-D hexagonal-lattice PhC; and for the (c) fourth and (d) fifth frequency bands in a 2-D square-lattice PhC. The PhCs are the same as those considered in Fig. 3.1.

tities are very close to each other. Thus, the shortest wavelength can be taken as the wavelength in the homogeneous background dielectric,

$$\lambda_{min} \approx \lambda_b. \tag{3.8}$$

3.5 Summary

The theoretical basis of a new method for examining and understanding the characteristics of propagating electromagnetic waves in a PhC has been developed in this chapter. It was shown that the angular spectra of an arbitrary monochromatic field distribution inside a PhC is given by the product of the Bloch coefficient function (which gives the expansion of the field in terms of the Bloch modes) and the Fourier coefficient function (which gives the expansion of the Bloch modes in terms of plane waves). The former is determined by the angular spectrum of the incident field and the boundary conditions imposed at the interface between the PhC and the homogeneous medium; the latter can be obtained numerically using the PWE method.

The Fourier-coefficient functions for two PhC geometries, hexagonal and square lattice, were presented. It was shown that the magnitude of these functions for the first, second, and third bands vary accordingly to the shape of the first, second, and third BZs respectively. It was also shown that, for the first five bands, the Fourier-coefficient function concentrates the significant amplitudes predominantly in the 1HAZ of the reciprocal space.

Finally, for the two PhCs under consideration, it was found that for frequencies in the first five bands, the minimum wavelength of the Bloch mode can be approximated as the wavelength in the unpatterned dielectric medium.

Chapter 4

Method of analysis

This chapter describes a practical method to study the reflection and refraction phenomena of arbitrary monochromatic fields at the interface between homogeneous and periodic media. It combines the finite difference time domain (FDTD) method [47] with Fourier analysis to study the fields in both real and reciprocal spaces. Henceforth, we shall refer to this technique as the FDTD-Fourier method.

Recently, a similar approach has been proposed by Srinivasan and Painter [48, 49] . to design high-Q PhC optical cavities. Such a method also obtains the **k**-space representation of a particular field distribution from an FDTD simulation, but the problem formulation has been limited to the analysis of resonant devices. The latter type of problem often assumes an omni-directional electromagnetic field distribution confined inside the PhC. This, in turn, excludes from the problem any refraction/refraction phenomenon and limits the **k**-space analysis to the study of the mode profiles in order to reduce radiation losses and improve the Q-factor [50, 51]. The goal of the method described in this chapter, on the other hand, is the analysis of generalized reflection/refraction phenomena with the consideration of arbitrary field distributions. The main advantage of the FDTD-Fourier method applied to this type of problem is the ability to filter specific spatial frequency components in order to analyze them separately. This feature is exploited in Section 4.4 to analyze the power-coupling parameters at the interface between a homogeneous dielectric and a PhC.

4.1 Numerical real space

When analyzing the reflection and refraction phenomena between homogeneous and periodic media, one is often interested in the near field distribution of arbitrary fields. For this type of problem, the FDTD method is an adequate tool to obtain the electromagnetic fields in real space. The proposed methodology employs the FDTD method in linear, non-magnetic, and lossless media to compute the fields in real space while interacting with a PhC.

4.1.1 FDTD formulation

This section should not be considered a comprehensive introduction to the FDTD method. For details on the numerical technique the reader is referred to the book cited in Ref. [47], which extensively covers the method as applied to electromagnetics.

A two-dimensional FDTD algorithm was developed for purposes of this work. The code was validated by comparing numerical and analytical solutions for a number of Gaussian beams with different parameters propagating in a homogeneous medium. For all the FDTD simulations in this thesis, the two-dimensional numerical space is formed by N_x and N_y rectangular cells in the x and y directions, respectively, and it is truncated using a 64-layer Berenger's perfectly matched layer (PML) absorbing boundary [52]. The PMLs are applied equally on the four sides of the numerical space. However, in order to truncate the PhC edges, when possible, one must terminate the PhC in such a way that the refractive index does not vary along the PML. The values for N_x and N_y are not necessarily equal, and vary from 2000 to 3000 cells for the different cases. On the other hand, the sampling factors (distances between samples) in the x and y directions are identical and the symbol Δ is used to denote this parameter for either direction. The time step is given by $\Delta_t = S\Delta/c$, where c is the speed of light in vacuum and $S = 0.5$ is the Courant stability factor.

4.1.2 Real space resolution

The sampling distance, Δ, must be fine enough to obtain an accurate sampling of the electromagnetic fields and to resolve satisfactorily the shape of the periodic elements. To achieve a reliable sampling of the electromagnetic field distribution the value of Δ must be less than one tenth of the shortest wavelength in the entire numerical space [53]. Such a criterion automatically sets an upper bound to the sampling distance over the periodic elements.

The FDTD simulations in this work consider homogeneous and PhC half spaces, where the PhC consists of air-holes etched in a high index background dielectric material. In such a PhC the minimum wavelength of a field can be approximated by the wavelength in the unpatterned background dielectric[1]. Thus, provided that the refractive index of the homogeneous medium is smaller than the index of the PhC background dielectric, the sampling condition for the electromagnetic field is restricted by

$$\Delta \leq \frac{\lambda_b}{10}, \tag{4.1}$$

where λ_b is the wavelength in the unpatterned background dielectric.

The sampling distance considered in the FDTD simulations presented in further chapters is $\Delta < \lambda_b/20$. For the highest frequency employed in the simulations ($a/\lambda = 0.425$) the sampling distance, $\Delta \approx \lambda_b/20$, is well below the limit dictated by Eq. (4.1). On the other hand, the periodic element (air-hole etched in the PhC background dielectric) is resolved with an array of 30×30 cells, which implies $\Delta = a/30$. This resolution is adequate to define the shape of the periodic element accurately. In addition, the staircasing edges of the air-hole that result from the discretization are smoothed by applying a dielectric-constant averaging method [53]. This reproduces the effect of a truly circular shape.

The electromagnetic field distribution of a two-dimensional TM-mode point source (a 3-D line source) is computed by applying the FDTD formulation previously described.

[1]Refer to Section 3.4 for details.

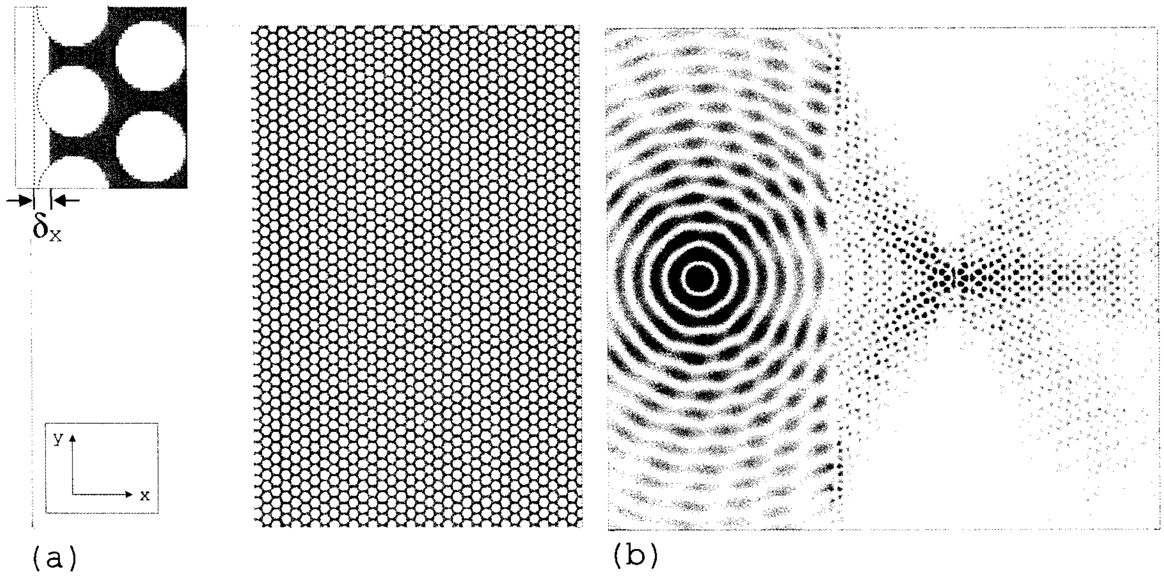

Figure 4.1: (a) Semi-infinite PhC composed of air holes of radius $r = 0.4a$ etched in a background dielectric with refractive index $n_b = 3.6$. The interface between the two media is located at $x_0 = 20a$. The PhC's surface termination is shown in the inset, where $\delta_x = 0.2a$. (b) Electric field distribution obtained with the FDTD method for a unit-amplitude 2-D point source (i.e., a line source) located at $x = 7.5a, y = 22.5a$.

The point source sits in free space and its field impinges onto a two-dimensional hexagonal lattice composed of air-holes of radius $0.4a$ etched in a background dielectric with refractive index $n_b = 3.6$. The PhC is assumed to be infinite and homogeneous in the (y, z)-plane and exists in the half space for $x > 20a$ as illustrated in Fig. 4.1(a). The PhC interface is in the Γ-K direction of the crystal and its termination is shown in the inset of Fig. 4.1(a), where $\delta_x = 0.2a$. The incident field is monochromatic with unit amplitude and free-space wavelength $\lambda = a/0.3$. Fig. 4.1(b) shows the electric field (E_z) distribution after 20000 time steps, which corresponds to $0.033\mu s$ approximately.

4.2 Numerical angular spectra

The angular spectra are obtained numerically from the FDTD data by applying a two-dimensional Fast Fourier Transform (FFT). Since the FDTD method is a time-domain solution technique, the computed field distribution is represented by a real-valued traveling-wave type function. Such a function only provides information about its amplitude distribution over the space but not about its phase. The lack of phase information results in an ambiguous angular spectrum, where each wave vector is duplicated by its complex conjugate. The first step leading us to work in **k**-space is therefore the transformation of the real-valued expression into a complex-phasor form.

4.2.1 Complex-phasor field representation

Provided that the field under analysis is monochromatic, one can recover the phase information by using two real-valued fields, one of which is delayed by a quarter-wavelength with respect to the other, i.e.,

$$\begin{aligned} \psi(\mathbf{r};t) &= \psi(\mathbf{r})\exp(-j\omega_0 t) \\ &= \tilde{\psi}(\mathbf{r};t) - j\tilde{\psi}\left(\mathbf{r};t-\frac{\lambda}{4c}\right), \end{aligned} \tag{4.2}$$

where $\tilde{\psi}(\mathbf{r};t)$ is the real-valued time dependent spatial distribution of a particular field component, λ is the free-space wavelength, and c is the velocity of light in vacuum. The angular spectra of $\psi(\mathbf{r};t)$ at a particular time $t=t_0$ are then obtained by applying a two-dimensional FFT routine,

$$\Psi(\mathbf{k}) = \mathrm{FFT}\{\psi(\mathbf{r};t_0)\}. \tag{4.3}$$

4.2.2 k-space resolution

The FFT operates on a discrete function with sampling distance Δ, bounding the **k**-space by $k_x^{max} = k_y^{max} = \pi/\Delta$. The sampling distance must satisfy the condition given in Eq. (4.1). Therefore, the resulting **k**-space has $k_x^{max} = k_y^{max} \geq 5k_b$, where k_b is the wave number in the PhC background dielectric. A considerable resolution reduction in the **k**-space follows from this fact because the region containing useful spectral information is limited by a circle of radius k_b [2]. To overcome this problem, we provide a convenient method to increase the resolution of the **k**-space without increasing the FDTD numerical data. To this end, we consider the sampling factor, Δ_k, which determines the resolution of the **k**-space. It is given by

$$\Delta_{k\xi} = \frac{2\pi}{N_\xi \Delta}, \tag{4.4}$$

where N_ξ is either N_x or N_y. From the previous expression, we note that the resolution in the **k**-space increases (i.e., Δ_k becomes smaller) when the number of sampled points increases, even if the resolution in real space is kept fixed. Hence, one can increase the resolution in the **k**-space by padding the FDTD field solution with zero-amplitude fields before applying the FFT routine. This process leads to interpolation of the **k**-space, since the FFT routine is able to resolve more precisely the propagation angles in real space. In this way, the resolution in the **k**-space is improved by a factor of N_ξ^{pad}/N_ξ, where N_ξ^{pad} is the number of cells in the FDTD grid along the ξ-direction after the padding.

4.2.3 Numerical artifacts

The angular spectra of the field in Fig. 4.1(b) are computed per Eq. (4.3) applying a padding factor of $N_\xi^{pad}/N_\xi = 4$ in both x and y directions. The results are shown in Figs. 4.2(a) and 4.2(b), which correspond to the angular spectra of the fields in the homogeneous medium and inside the PhC, respectively. The superimposed contours in Figs. 4.2(a) and 4.2(b) represent, respectively, the **k**-shell and the EFC in the repeated zone scheme, both at the operating frequency.

Whenever the analysis in **k**-space is performed through the method described above, one must consider important numerical artifacts that arise when obtaining the angular spectra or when they are processed. In what follows we discuss such artifacts and give suggestions to minimize their effects.

[2]Refer to Section 3.1 for details.

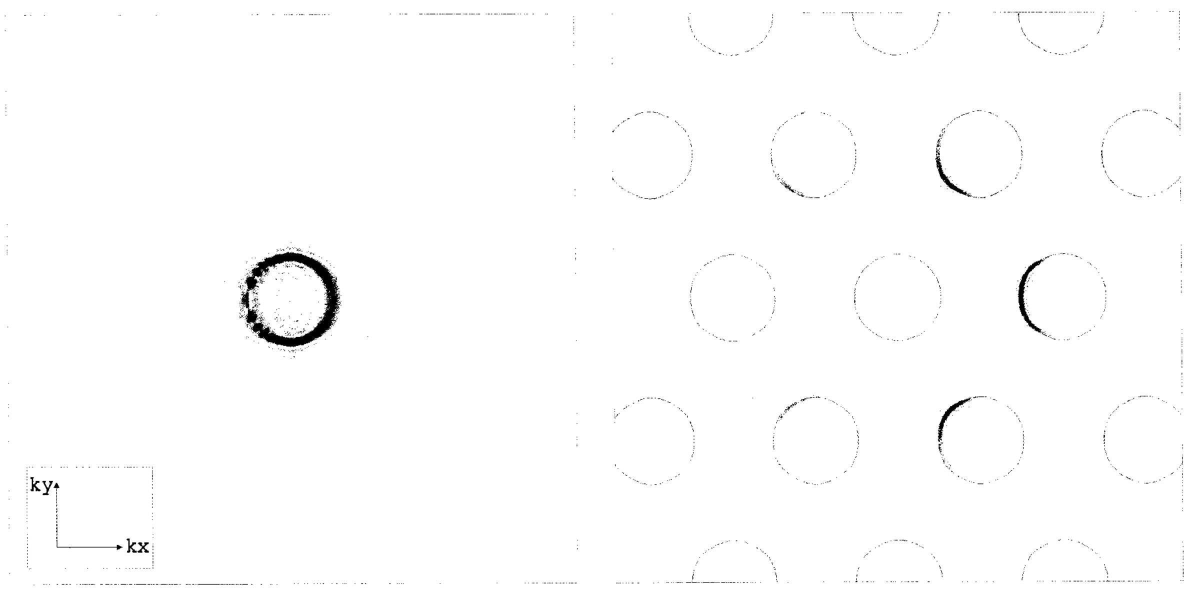

(a) (b)

Figure 4.2: Angular spectra of the field shown in Fig. 4.1(b) for (a) the field in the free-space region and for (b) the field inside the PhC. The superimposed circle in (a) represents the free-space **k**-shell and the superimposed contours in (b) represent the EFC in the repeated zone scheme.

Spectral-amplitude scaling

When computing the angular spectra, the FFT takes into account the area over which the field is distributed in order to execute the transformation. Consequently, the numerical angular spectra do not represent the true amplitudes of the Fourier components; they are proportional to the area over which the filed is distributed in the numerical space. Furthermore, if the field is not symmetrically distributed over the space, the computed angular spectra may present artificial variations on their amplitudes. To illustrate this anomaly we consider the angular spectrum in Fig. 4.2(a). We notice that the spectrum describes spatial frequencies on the free-space **k**-shell, which is superimposed in Fig. 4.2(a); yet, observe that the spectral amplitudes are not uniform for every point on the **k**-shell even though the source is a perfect point source. This is because the field in the homogeneous region is able to propagate a longer distance in the vertical direction than in the horizontal direction (see Fig 4.1(b)). Therefore, the spectra shows larger amplitudes and better angular resolution for components near the

k_y axis.

To reduce this effect, one must try to configure the problem in such a way that the field components of interest are symmetrically distributed over the space. In such a case, *the amplitudes of the angular spectra differ from the real ones by an arbitrary constant factor, which is proportional to the area covered by the field in the numerical space.*

This same artifact has a large impact on evanescent modes. The nature of evanescent modes allows them to exist only over small areas for they decay exponentially as they propagate. Therefore, their angular spectra show small amplitudes, which are not necessarily proportional to their real amplitudes. It is important to take into account this fact since it can lead to a misinterpretation of the physical phenomenon.

Spurious evanescent modes

Spurious evanescent modes are artifacts created by the finite computational domain. Such artifacts can be identified in Fig. 4.2(a) as the angular spectra located off the free-space **k**-shell, which presents decaying amplitudes that extend inside and outside its circumference.

To explore the nature of these artifacts, we take into account the finite problem space by defining a *window* transfer function with rectangular shape. Such a function has unit amplitude for points inside the rectangle and zero amplitude for points outside, i.e.,

$$h(\mathbf{r}) = \mathrm{rect}\left(\frac{\mathbf{r}\cdot\hat{\mathbf{x}}}{l_1}\right)\mathrm{rect}\left(\frac{\mathbf{r}\cdot\hat{\mathbf{y}}}{l_2}\right), \tag{4.5}$$

where l_1 and l_2 define the dimensions of the rectangle in the x and y directions, respectively. The new field distribution that explicitly takes into account the finite problem space, $\psi_h(\mathbf{r})$, is then expressed as the product of the original field distribution, $\psi(\mathbf{r})$, and the *window* transfer function, $h(\mathbf{r})$. By applying a Fourier transform to $\psi_h(\mathbf{r})$, one obtains

$$\Psi_h(\mathbf{k}) \equiv \mathcal{F}\{\psi(\mathbf{r})\,h(\mathbf{r})\} = \Psi(\mathbf{k}) * H(\mathbf{k}), \tag{4.6}$$

where the operator $*$ denotes convolution. This indicates that the $\mathbf{k}$-space representation of a plane wave is given by the Fourier transform of the window function, which reads [54]

$$H(\mathbf{k}) = |l_1 l_2| \operatorname{sinc}\left(\frac{l_1 \mathbf{k}\cdot\hat{\mathbf{x}}}{2\pi}\right) \operatorname{sinc}\left(\frac{l_2 \mathbf{k}\cdot\hat{\mathbf{y}}}{2\pi}\right). \tag{4.7}$$

Spurious evanescent modes have therefore sinc-like distributions extended in directions perpendicular to the sharp cuts that bound the problem space, and their amplitudes are proportional to those of the angular spectra that generate them. These artifacts are often produced when computing the angular spectra from fields that are isolated in the real domain, creating sharp cuts on their distributions. In order to overcome this problem, whenever possible, one should isolate the portion of the field in such a way that the sharp cuts are made in regions where the amplitudes are minima.

Spurious fields

Spurious fields are artifacts generated by the inverse FFT routine when one isolates a portion of the angular spectra and then transforms it back to the real domain. In general, spurious fields have small amplitudes and usually their impact is not significant. However, if the angular spectrum to be transformed has small amplitudes, comparable to the amplitudes of the spurious fields, then the resulting field will show distortions due to these artifacts.

4.3 Analysis of reflection and refraction

It is difficult to characterize the field refracted into a PhC, especially when the field is highly divergent as in Fig. 4.1(b). In such cases, the analysis in real space only provides qualitative conclusions in terms of the overall field profile and propagation direction. On the other hand, the angular spectra of a field distribution represent each plane-wave component in terms of its wave vector, which is a unique point in the $\mathbf{k}$-space. This feature allows one to analyze plane-wave components separately and to characterize independently their amplitude profile and propagation direction.

In later chapters the analysis of reflection and refraction phenomena is carried out based on the numerical angular spectra of arbitrary monochromatic fields obtained through the methodology previously presented. Through this technique we shall study the Fourier components of excited Bloch modes individually and characterize the complicated reflected-field pattern in both real and reciprocal spaces. Some procedures that follow from useful Fourier theorems can be applied to the numerical data in order to enrich the analysis; they are described in what follows.

4.3.1 Field isolation

The analysis of individual beams, or particular portions of the field of interest, can be achieved through field isolation. This consists of extracting part of the total field in order to study its angular spectrum individually. For example, the separated angular spectra in Fig. 4.2(a) and 4.2(b) are obtained by isolating the field distribution in the homogeneous region from the fields inside the PhC and then computing their respective angular spectra individually.

4.3.2 Spectrum isolation

The main advantage provided by the analysis in **k**-space is the ability to filter specific spatial frequency components. For example, consider Fig. 4.2(b); it shows the angular spectra of the field in the PhC. Observe that these spectra describe spatial frequencies on the EFC in the repeated zone scheme, which is superimposed in the figure. One can filter the Bloch space-harmonics located in a particular EFC and analyze their characteristics, independently from the rest, in both real and reciprocal spaces. This will be done in Chapter 5, for example.

4.3.3 Spatial demodulation

A Bloch mode consists of an infinite number of Bloch space-harmonics; each harmonic is spatially modulated by the reciprocal lattice vector. We shall find it useful to apply the shift theorem of the Fourier transforms in order to demodulate particular groups of Bloch space-harmonics and analyze their field envelope in real space.

4.4 Analysis of reflectance and transmittance

Two important parameters when analyzing the reflection and refraction phenomena are the reflectance and transmittance. They are defined as the ratio of the power fluxes of the reflected and transmitted fields, respectively, to the power flux of the incident field. These parameters characterize the power coupling across the interface between any two media. Particularly, at the interface between a homogeneous medium and a PhC, the power coupling has a complicated angular-dependent behavior [56, 57, 58, 59, 60] and, in general, such behavior cannot be described analytically. However, a number of different numerical techniques have been employed. For example, Ruan *et al.* [61] proposed a technique based on the cylindrical-wave KKR (Korringa-Kohn-Rokester) method [2, 62], and Sakoda [63, 64] introduced a general technique based on the PWE method.

In this section we develop a way to use the FDTD-Fourier method in order to obtain the power coupling parameters at the interface of between a homogeneous medium and a PhC. This methodology will be used in Chapter 6 to study the reflectance and transmittance in a real PhC device. Here, we consider the setup shown in Fig. 4.3(a), which consists of a homogeneous dielectric medium with refractive index $n_b = 3.6$ and a two-dimensional hexagonal lattice of air holes etched in the same dielectric medium. The interface between the two media is located at $x_0 = 20a$. The structural parameters of the PhC are identical to those corresponding to the PhC previously presented in this chapter, except that in this case the PhC has complete surface termination (see inset in Fig. 4.3(a)).

4.4.1 Computing the Poynting vector and power flux

Prior to obtaining the power coupling parameters we shall discuss a method for acquiring the time-averaged power flux from the FDTD data. To this end, we consider the average power density carried by an electromagnetic wave, which is represented by the time-averaged Poynting vector

$$\mathbf{S}(\mathbf{r}) = \frac{1}{2}\mathrm{Re}\{\mathbf{E}(\mathbf{r}) \times \mathbf{H}^*(\mathbf{r})\}, \tag{4.8}$$

where $\mathbf{E}$ and $\mathbf{H}$ are complex functions describing the electric and magnetic fields, respectively; it represents the average power per unit area in Watts per square-meter ($\mathrm{W/m^2}$). It is straightforward to obtain the power density from the FDTD data. For

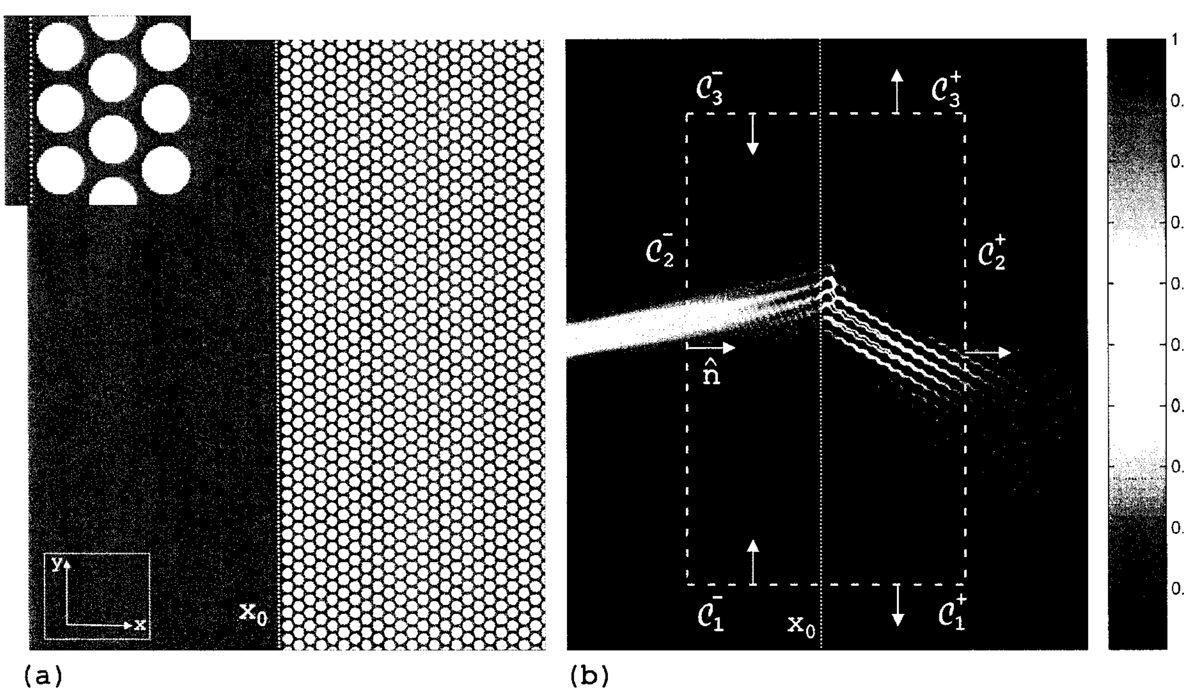

Figure 4.3: (a) Semi-infinite PhC made of air holes of radius $r = 0.4a$ etched in a background dielectric with refractive index $n_b = 3.6$. The background dielectric is extended into the homogeneous region and the PhC interface is located at $x_0 = 20a$. (b) Magnitude of the Poynting vector of a Gaussian beam impinging onto the PhC shown in (a).

example, for TM modes, the time-averaged Poynting vector is given by

$$\begin{aligned} \mathbf{S}(\mathbf{r}) &= \frac{1}{2}\mathrm{Re}\{E_z(\mathbf{r})H_x^*(\mathbf{r})\}\hat{\mathbf{y}} - \frac{1}{2}\mathrm{Re}\{E_z(\mathbf{r})H_y^*(\mathbf{r})\}\hat{\mathbf{x}} \\ &= S_y(\mathbf{r})\hat{\mathbf{y}} - S_x(\mathbf{r})\hat{\mathbf{x}}, \end{aligned} \tag{4.9}$$

where the complex fields, $E_z(\mathbf{r}), H_y(\mathbf{r})$, and $H_x(\mathbf{r})$ are obtained directly from Eq. (4.2) using the FDTD-Fourier method. On the other hand, the time-averaged power flux crossing an arbitrary contour (or a surface for 3-D distributions) is obtained through the following expression,

$$P = \int_{\mathcal{C}} \mathbf{S}(\mathbf{r}) \cdot \hat{\mathbf{n}}\, d\mathcal{C}, \tag{4.10}$$

where $\mathcal{C}$ denotes the coordinates forming such an arbitrary contour, and $\hat{\mathbf{n}}$ is a unit vector normal to $\mathcal{C}$ at every point. This expression provides the power flux in Watts/meter.

Henceforth, we shall consider average quantities assuming that the fields have reached the steady state. Therefore, the time-averaged Poynting vector and the time-averaged power flux will be simply referred to as *Poynting vector* and *power flux*. Furthermore, we will focus the discussion on TM modes with Gaussian distribution only, i.e., Gaussian beams with the magnetic vector laying in the (x, y)-plane.

4.4.2 Computing the reflectance and transmittance

In what follows, we develop a method to calculate the reflectance, $\mathcal{R}$, and transmittance, $\mathcal{T}$. For this purpose, we consider the propagation of a Gaussian beam from the homogeneous medium into the PhC shown in Fig. 4.3(a). The magnitude of its Poynting vector is shown Fig. 4.3(b) after 0.04 μs. The elapsed time corresponds to 25000 time iterations in the FDTD algorithm and is long enough for the fields to reach the steady state. The beam propagates from left to right at an angle of $\phi = 10°$ with respect to the horizontal axis. It has a waist of $w_0 = 2.7a$ and is located at the left edge of the homogeneous medium from where it is launched. The normalized frequency of the beam is $a/\lambda = 0.3$.

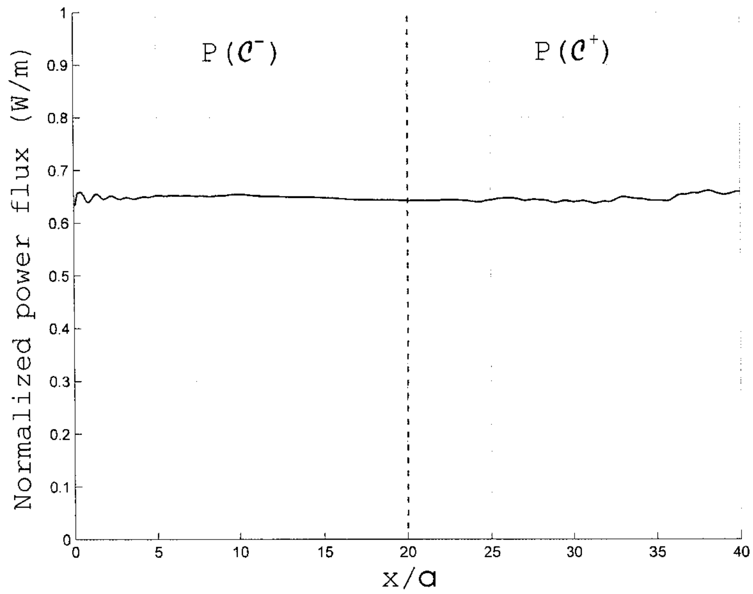

Figure 4.4: Normalized power flux as a function of x obtained from the Poynting vector distribution in Fig. 4.3(b).

The power carried by the fields is obtained directly by integrating the Poynting vector distribution per Eq. (4.10). Two contours of integration are indicated in Fig. 4.3(b). They are placed to the left and right hand sides of the interface. Both contours are divided into three segments, as indicated by the dashed lines. The contour on the left, $\mathcal{C}^- = \sum_{i=1}^{3} \mathcal{C}_i^-$, defines the integration contour used to compute the power flux in the homogeneous region; the one on the right, $\mathcal{C}^+ = \sum_{i=1}^{3} \mathcal{C}_i^+$, is used to compute the power flux inside the PhC. The definition of the contour-normal vectors ($\hat{\mathbf{n}}$) is also illustrated by the arrows, indicating the direction of the positive flux. The power flux is therefore given by the following expressions

$$\begin{aligned} P(\mathcal{C}^-) &= -\int_{\mathcal{C}_1^-} S_y(x, y_1^-)\, dx + \int_{\mathcal{C}_2^-} S_x(x_2^-, y)\, dy - \int_{\mathcal{C}_3^-} S_y(x, y_3^-)\, dx \\ P(\mathcal{C}^+) &= \int_{\mathcal{C}_1^+} S_y(x, y_1^+)\, dx + \int_{\mathcal{C}_2^+} S_x(x_2^+, y)\, dy + \int_{\mathcal{C}_3^+} S_y(x, y_3^+)\, dx. \end{aligned} \tag{4.11}$$

The power flux associated with the Poynting vector distribution in Fig. 4.3(b) is illustrated in Fig. 4.4. It is normalized to the power flux carried by the incident beam, P_i. The vertical dashed line indicates the interface between the homogeneous and periodic media. The values to the left of the vertical line represent $P(\mathcal{C}^-)$ as the contour $\mathcal{C}^-$ is swept from $x = 0$ to $x = 20a$. Similarly, the values on the right indicate $P(\mathcal{C}^+)$ as $\mathcal{C}^+$ moves from $x = 20a$ to $x = 40a$. A constant power flux of $0.64P_i$ was obtained over the entire plane, expressing the conservation of the energy in the lossless medium. The small variations in the flux are attributed to numerical errors that arise from the time-space interleaving of the electric and magnetic fields in the FDTD formulation [47, 55]. These variations represent a standard deviation of approximately 1.5%; hence, they can be considered to be small enough to be ignored. The quantity $P(\mathcal{C}^+)$ is the power transmitted into the periodic structure. On the other hand, the quantity $P(\mathcal{C}^-)$ equals the sum of the power carried by the incident beam and the power carried by the field reflected at the interface. The latter corresponds to the sum of the power fluxes of the different backward-diffraction orders that comprise the reflected field.

4.4.3 Computing the diffraction efficiencies

The diffraction efficiency measures the portion of the total power carried by the individual diffraction orders. This parameter has been obtained experimentally [40, 66] and numerically [56, 64] in the PhC context by employing a number of different techniques. Here, the power carried by individual backward-diffracted orders, and by the incident beam, can be obtained by filtering their corresponding spatial frequencies in the **k**-space and then transforming the filtered angular spectra back to the real domain in order to calculate their respective power fluxes. The magnitudes of the resulting Poynting vector distributions after the field isolation process are shown in the left pane of Fig. 4.5(a), for the incident beam, and in the left pane of Figs. 4.5(b) and 4.5(c), respectively, for the zeroth and the -1 backward-diffraction orders. The power fluxes for the isolated fields, shown on the right pane of Fig. 4.5, are obtained following the same procedure used to compute the power flux shown in Fig. 4.4.

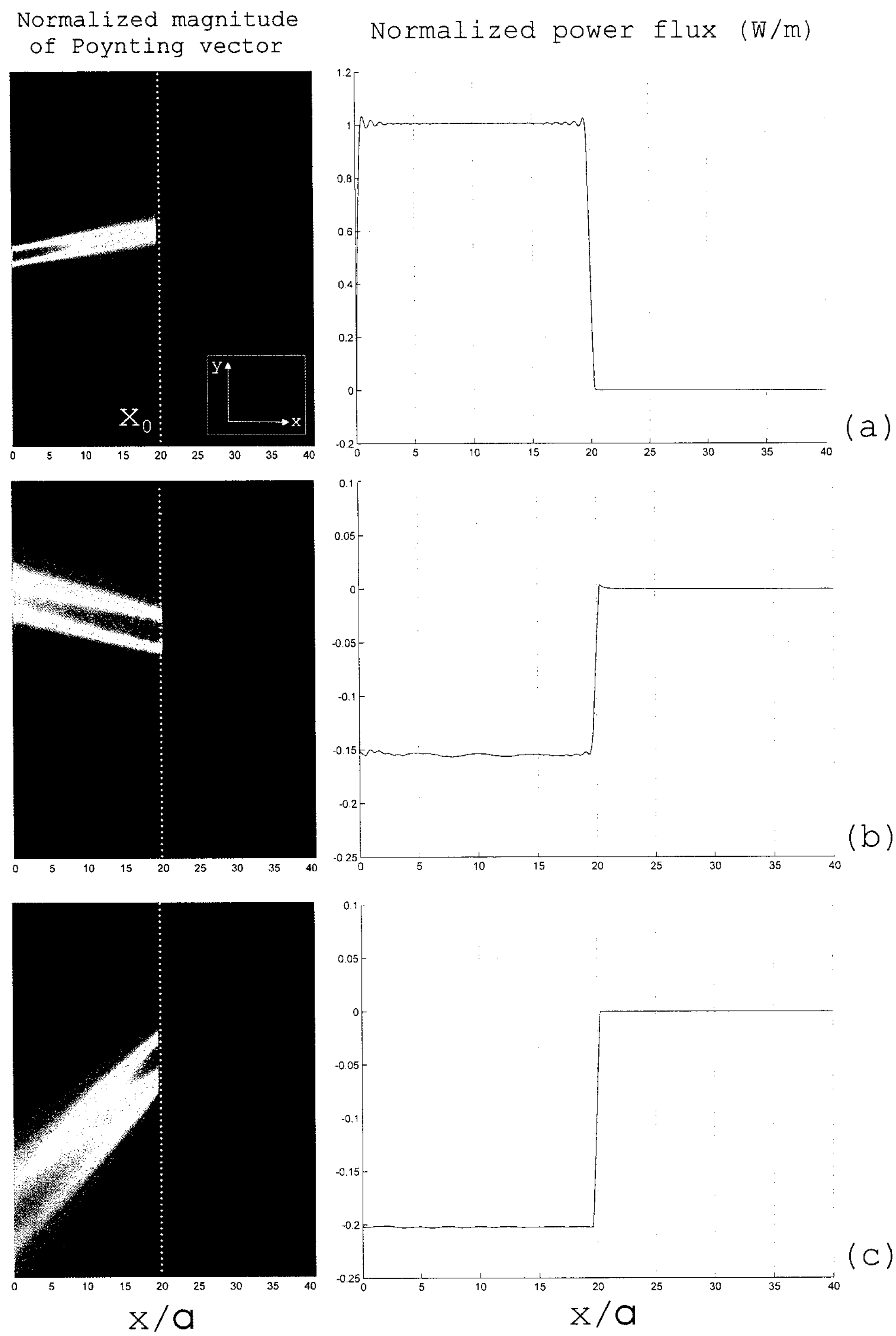

Figure 4.5: Normalized magnitude of the Poynting vector distribution and normalized power flux corresponding to (a) the incident Gaussian beam, (b) the zeroth backward-diffraction order, and (c) the −1 backward-diffraction order.

4.4.4 Quantitative results

The results in Fig. 4.4 and Fig. 4.5 are summarized in Table 4.1. The values given in the table denote the mean values of the power fluxes and their respective standard deviations. The power transmitted into the PhC and the power reflected at the interface between the two media are denoted by P_t and P_r, respectively. Moreover, the power carried by the zeroth and -1 backward-diffraction orders that comprise the reflected field are denoted by $P_r^{(0)}$ and $P_r^{(-1)}$, respectively.

Table 4.1: Calculated power fluxes of the incident, reflected, and transmitted fields. $^{(*)}$ Obtained from the result in Fig. 4.4. $^{(**)}$ Obtained as the sum of the power fluxes of the zeroth and -1 backward-diffraction orders.

Designator	Power flux	Standard Dev.
P_i	1 W	-
P_t	$0.640P_i$ $^{(*)}$	1.5%
P_r	$0.355P_i$ $^{(**)}$	1.0%
$P_r^{(0)}$	$0.155P_i$	0.8%
$P_r^{(-1)}$	$0.200P_i$	0.2%

From the results in Table 4.1, one can immediately compute the transmittance and reflectance for the TM field as,

$$\begin{aligned} \mathcal{T} &= \frac{P_t}{P_i} \approx 0.64 \\ \mathcal{R} &= 1 - \mathcal{T} \approx 0.36. \end{aligned}$$

The reflectance can also be calculated as $\mathcal{R} = P_r/P_i \approx 0.355$; the small discrepancy is due to the error involved in the power flux calculations. Moreover, the backward-diffraction efficiency of the two diffracted orders is readily obtained as

$$\begin{aligned} \mathcal{R}^{(0)} &= \frac{P_r^{(0)}}{P_i} \approx 0.155 \\ \mathcal{R}^{(-1)} &= \frac{P_r^{(-1)}}{P_i} \approx 0.2. \end{aligned}$$

4.5 Summary

This chapter introduced the FDTD-Fourier method of analysis, which is applicable to more general PhC field situations than similar approaches described by other authors. The most important capability offered by this technique is the ability to separate the field distribution into physically interpretable beams. The method consists of obtaining the angular spectra of an arbitrary monochromatic field distribution from an FDTD simulation in order to study the fields in both real and reciprocal spaces. The process to obtain the angular spectra numerically follows three main steps: (1) Compute the electromagnetic fields using the FDTD method, (2) transform the real-valued fields into a complex phasor form, and (3) apply a FFT routine to obtain its angular spectra. This methodology will be used in later chapters to study the reflection and refraction phenomena at the interface between homogeneous and periodic media.

The impact of the finite computation domain and numerical data manipulation on the resulting angular spectra were highlighted. It was indicated that the amplitudes of the angular spectra are proportional to the area covered by their respective fields in the numerical real domain. Therefore, it is important to specify the dimensions of the computation domain in such a way that the fields of interest are symmetrically distributed over the space. It was shown that spurious evanescent modes are a consequence of the finite computation domain, and that they are also generated when fields in real space are isolated in order to compute their angular spectra. Similarly, spurious fields are introduced when part of the angular spectra is isolated and transformed back to the real domain. In general, the impact of these artifacts is only significant when analyzing fields with small amplitudes that are comparable to the amplitudes of the spurious fields introduced.

The method was applied to compute the reflectance and transmittance at the interface between a homogeneous medium and a PhC. To this end, the total field obtained from an FDTD simulation was decomposed into incident, reflected, and transmitted fields by using the FDTD-Fourier method. Then the power flux carried by the three separate fields was calculated in the real domain to determine the transmittance and the reflectance, as well as the diffraction efficiencies of the different backward-diffraction orders that constitute the reflected field. This procedure will be employed in Chapter 6 to study the reflectance and transmittance in a real PhC device.

Chapter 5

Reflection/refraction analysis in square and hexagonal lattices

This chapter exploits the FDTD-Fourier method to study the reflection and refraction phenomena at the interface between homogeneous media and semi-infinite PhCs. Sections 5.1 and 5.2 present, respectively, the analysis for hexagonal and square lattices. The importance of the Fourier-coefficient function is discussed in order to understand the field inside a PhC and to evaluate the distortion on the different beams (Bloch space-harmonics) that form the overall mode profile. The analysis allows us to explain a number of interesting phenomena, and to obtain quantitative estimations of distortion on the refracted and reflected fields.

5.1 The hexagonal-lattice PhC

In this section we consider the propagation of Gaussian beams from a homogeneous dielectric medium with refractive index $n_b = 3.6$ into a two-dimensional hexagonal lattice of air-holes etched in the same dielectric medium. The holes have a radius of $0.4a$, where a is the lattice constant. The PhC has complete surface termination, as for the case shown in Fig. 4.3(a). The two-dimensional space is assumed to be infinite and homogeneous in the z-direction. For the PhC half space, the plane of periodicity is in

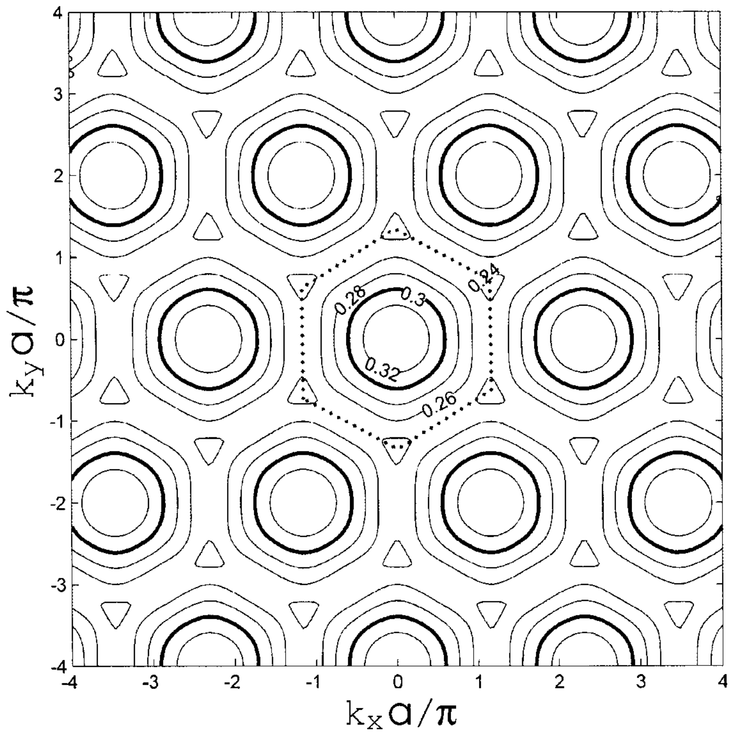

Figure 5.1: The EFC in the repeated zone scheme for several frequencies in the second frequency band of the hexagonal-lattice PhC under consideration. The 1BZ is denoted by the hexagon at the center. The normalized frequencies are indicated on the contours.

the (x, y)-plane. The interface between the homogeneous medium and the PhC is in the (y, z)-plane in the Γ-K direction of the crystal. Beams with normalized frequency $a/\lambda = 0.3$ and various propagation angles are considered for the analysis.

The photonic band structure of the PhC under consideration is shown in Fig. 2.2(a); the horizontal solid line indicates the operation frequency for the present case. The EFC in the repeated zone scheme for several frequencies in the second band is shown in Fig. 5.1. The normalized frequencies associated with the different contours are indicated on the contours located inside the 1BZ; the bold contours denote the EFC at the operation frequency. We notice that the EFC is almost a perfect circle of radius $0.6\pi/a$. Furthermore, we notice that radius of the EFC decreases as the frequency increases, which implies negative group velocity. Hence, at the operation frequency, The EFC in the 1BZ is similar to the **k**-shell of a homogeneous medium with refractive index $n_{eff} = -1$, describing an isotropic left-handed medium.

In the present setup, the refractive index in the homogeneous dielectric is much larger than the magnitude of the effective index in the PhC, $|n_{eff}|$. As a result, the boundary condition at the various possible angles of incidence can be matched by beams from different EFCs located in different primitive cells. This is illustrated schematically in Fig. 5.2(a). It shows the EFC in the repeated zone scheme (small circles) and the **k**-shell of the homogeneous dielectric (large circle) both at the operation frequency. The vertical dashed line indicates the orientation of the interface, the dashed hexagon at the center of the **k**-space represents the reciprocal primitive cell, and the parameter q on the right hand side indicates the transverse row number for the row of primitive cells perpendicular to the interface. Notice that the incident plane wave, denoted by the wave vector $\mathbf{k}^{(i)}$, is able to satisfy the $\mathbf{k}_{||}$–conservation condition with EFCs located in the row of primitive cells $q = +1$. In addition, for some ranges of incidence angle, none of the EFCs can provide propagating wave that would match the boundary condition; hence, a *partial gap* exists over this angular range. Also notice that if the PhC interface is oriented in the Γ-M direction of the crystal a partial gap will appear for incidence angles around zero degrees. This is in fact the reason why the interface was selected rather in the Γ-K direction, so refraction is also possible for waves with small incidence angles. The refraction phenomenon is therefore limited to incident waves that match their tangential wave vectors with EFCs in any of the three rows of primitive cells, $q = -1, q = +1$ or $q = 0$. We shall now study in more detail the interesting refraction phenomenon.

5.1.1 Ranges of incidence angle

Refraction at an interface between a homogeneous medium and a periodic medium is governed by Snell's law of refraction when the EFCs are circular, and the dominant wave vectors in the PhC lie inside the 1BZ. However, if the wave vectors are located beyond the 1BZ in other primitive cells, Snell's law does not always apply (as shown below). The reason is that under these conditions, the tangential components of the incident wave vector must equal the tangential component of the sum of the refracted

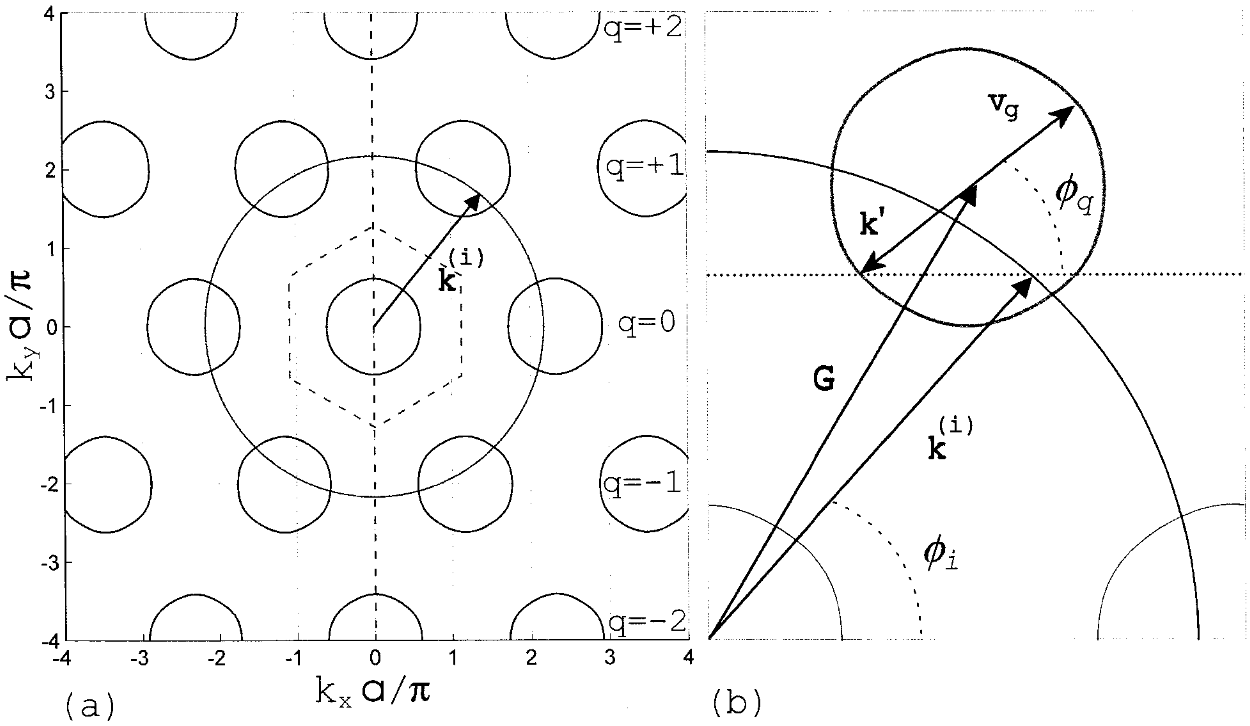

Figure 5.2: (a) The EFC in the repeated zone scheme for the hexagonal-lattice PhC under consideration and the **k**-shell for the homogeneous medium, both at the operation frequency. The vertical line indicates the orientation of the interface. (b) Definition of the incident and refraction angles and vectors in the **k**-space representation.

wave vector and the relevant reciprocal lattice vector,

$$\mathbf{k}_{||}^{(i)} = \mathbf{k'}_{q,||} + \mathbf{G}_{q,||}, \tag{5.1}$$

where $\mathbf{k}_{||}^{(i)}(= kn_b \sin\phi_i)$ is the tangential component of the incident wave vector with k being the wave vector in vacuum, n_b being the refractive index of the homogeneous medium, and ϕ_i being the incidence angle; $\mathbf{k'}_{q,||}(= kn_{eff}\sin\phi_q)$ is the tangential component of the Bloch vector with n_{eff} being the effective refractive index in the PhC and ϕ_q being the refracted angle of the q-th beam; and $\mathbf{G}$ is the reciprocal lattice vector. The definition of the angles and vectors is shown in Fig. 5.2(b). For the PhC under consideration, the tangential component of the reciprocal lattice vector is given by

$$\mathbf{G}_{q,||} = \frac{q2\pi}{a}, \tag{5.2}$$

Table 5.1: Propagation conditions and primitive cell row number as function of the incidence angle for the **k**-space diagram shown in Fig. 5.2(b).

incidence angle	Condition	q
$0^\circ < \phi_i < 16.1^\circ$	negative refraction	0
$16.1^\circ < \phi_i < 40.4^\circ$	partial gap	-
$40.4^\circ < \phi_i < 90^\circ$	anomalous refraction	1

where q is an integer indicating the row-number for the rows of primitive cells perpendicular to the interface, as shown in Fig. 5.2(a). For the row containing the 1BZ $q = 0$ (the tangential components of the reciprocal lattice vectors are zero). Only one value of q can be satisfied for each case. From Eqs. (5.1) and (5.2) a generalized refraction equation follows, namely

$$n_b \sin\phi_i = n_{eff} \sin\phi_q + \frac{q\lambda}{a}, \tag{5.3}$$

where λ is the wavelength in vacuum. In the primitive cells for which $q = 0$ the generalized refraction equation in Eq. (5.3) reduces to Snell's law, and the effect is regarded as (positive or negative) refraction. For negative refraction, n_{eff} is negative, which implies a change in the sign of the refraction angle. For $q \neq 0$ the behavior is regarded as an anomalous refraction process. The generalized refraction equation in Eq. (5.3) is valid only when the EFC is circular.

If the incidence angle is such that the condition in Eq. (5.1) cannot be satisfied (i.e., the wave vector falls in a partial gap), then all the power is reflected back into the homogeneous medium and the field inside the PhC consists only of evanescent waves.

In the case under consideration, a variety of conditions exist depending on the incidence angle. These conditions are summarized in Table 5.1 for incidence angles ranging from 0° to 90°. It also gives the value for q, the number for the row of primitive cells that contain the EFCs where the $\mathbf{k}_{||}$-conservation condition is satisfied. The behavior follows the same pattern for negative angles.

Examples of each of these conditions are now considered in more detail. In each case we have a Gaussian beam with its waist at the left-hand edge of the homogeneous medium from where it is launched. It then propagates from left to right toward the interface between the homogeneous medium and the PhC. At the interface, various refracted and reflected beams are generated. We shall study them using the FDTD-Fourier method of analysis.

5.1.2 Gaussian beam incident at 10°

The electric field distribution of the Gaussian beam is shown in Fig. 5.3(a). The beam has a waist radius $w_0 = 1.7a$ at $x = 0$. It propagates with an angle $\phi = 10°$ with respect to the horizontal axis and impinges onto the PhC surface located at $x_0 = 20a$. There are three reflected waves denoted by A1, A2, and A3. One of them, A3, is barely visible and propagates upward almost parallel to the interface. The other two have larger amplitudes and produce fringes in the incident beam. Inside the periodic medium, the field undergoes negative refraction, converges to a focal point, and then diverges faster than its homogeneous counterpart due to the smaller effective index

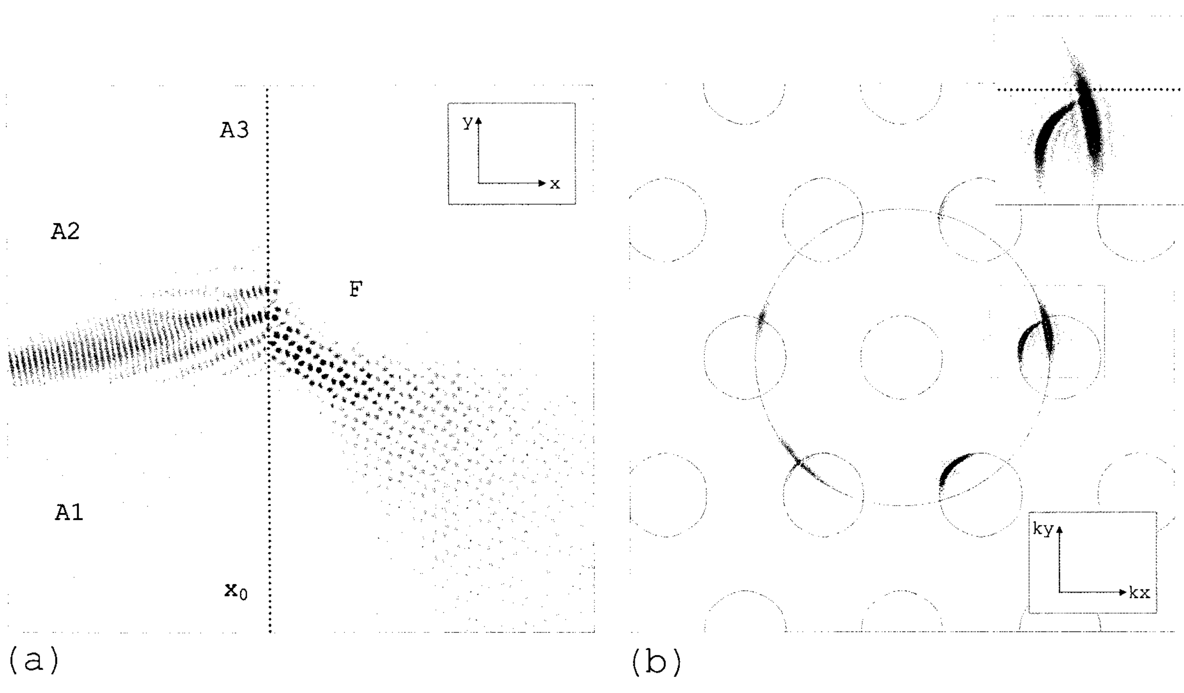

Figure 5.3: (a) Electric field distribution of the incident, reflected, and refracted fields for the $\phi = 10°$ case. The PhC interface is located at $x_0 = 20a$. (b) Angular spectra of the field distribution shown in (a).

magnitude. Moreover, the refraction angle of approximately $-42°$ is in fair agreement with the angle of $-38°$ that Eq. (5.3) predicts.

The magnitude of the angular spectra for the field distribution in Fig. 5.3(a) is shown in Fig. 5.3(b). The superimposed circles represent the **k**-shell and the EFCs in the repeated zone scheme, both at the operation frequency. One can see that the incident and reflected waves have spatial frequencies associated with the **k**-shell, and all the refracted waves have spatial frequencies associated with the EFCs of the PhC. There are also evanescent waves, which are neither located on the **k**-shell nor on the EFCs, and are very faint. These evanescent waves are generated at the interface.

We now proceed with the analysis in the Fourier domain to obtain a better understanding of the fields inside the periodic medium. We shall consider first the field refracted into the PhC.

Refracted beams

The incident Gaussian mode excites multiple Bloch modes to form the refracted field. Each Bloch mode consists of plane-wave components, or space-harmonics, located in different reciprocal primitive cells. We shall regard the group of Bloch space-harmonics located in common primitive cells as individual *beams*. These beams are not independent of each other since Bloch space-harmonics do not satisfy Maxwell's equations on their own. However, representing the fields inside the PhC as a collection of beams is useful to understand its behavior.

Fig. 5.4(a) shows the angular spectra of the field inside the PhC. Refracted beams with relevant spectral amplitudes are labeled B0, B1, B2, and B3. The location of the peak associated with the spectrum of a particular refracted beam indicates its direction of propagation, as given by the group velocity vector at that location. Since the peaks of the different beam spectra are located at more or less the same location on the respective EFCs, the different refracted beams propagate in more or less the same direction.

The angular spectra of the field inside the PhC can be represented as a Fourier-coefficient function associated with Bloch-modes in the second frequency band, $U^{(2)}(\mathbf{k})$, that modulates the periodic Bloch-coefficient function, $\alpha_p(\mathbf{k})$. The modulation effect causes the magnitude of the beam spectrum in the 1BZ to be significantly suppressed, while the magnitudes are enhanced in the 1HAZ.

The Fourier coefficient function is also responsible for other phenomena. If $U^{(2)}(\mathbf{k})$ has a large slope at the location where $\alpha_p(\mathbf{k})$ has a peak, then the product will produce a slightly shifted peak. The result is that the beam associated with that peak will propagate in a slightly different direction. This effect depends on the width of the peak in $\alpha_p(\mathbf{k})$; if the peak is very narrow (i.e., the beam is very wide), then the shift may be negligibly small. The beam spectra in Fig. 5.4(a) are wide enough to give a noticeable shift as a result of the modulation of $U^{(2)}(\mathbf{k})$. Consider, for example, the beam spectra labeled by B1, B2, and B3 in Fig. 5.4(a). These beam spectra can be separated and transformed back to the real domain. Their respective normalized field distributions are shown in Figs. 5.5(a), 5.5(b), and 5.5(c). First we note that their respective wave vectors are not parallel to their propagation directions– an effect called *walk-off*. The wave vectors are given by $\mathbf{k_G} = \mathbf{k'_G} + \mathbf{G}$, where $\mathbf{k_G}$ is the wave vector of the peak of the beam spectrum relative to the origin of the entire $\mathbf{k}$-space; $\mathbf{k'_G}$ is the wave vector of the peak of the beam spectrum relative to the origin of the particular primitive cell in which the beam spectrum is located and $\mathbf{G}$ is the reciprocal lattice vector associated with this primitive cell. The subscripts are used to distinguish the different primitive cells. The propagation directions of the beams are given by the group velocity vector, $\mathbf{v}_g(\mathbf{k_G})$. This walk-off effect can be seen as a consequence of the spatial frequency modulation introduced by shifting the spectrum by $\mathbf{G}$. One can remove this modulation to study the propagation direction, as well as the development of the envelope of the beam as it propagates through the PhC. The demodulated version of Figs. 5.5(a), 5.5(b), and 5.5(c) is shown in Figs. 5.5(d), 5.5(e), and 5.5(f), respectively. Notice that the propagation directions, as indicated by the arrows in the figures, are visibly different. These propagation directions can be compared with the $\mathbf{k'_G}$-vectors of the corresponding beam spectra shown in the insets. The propagation direction and the $\mathbf{k'_G}$-vectors point

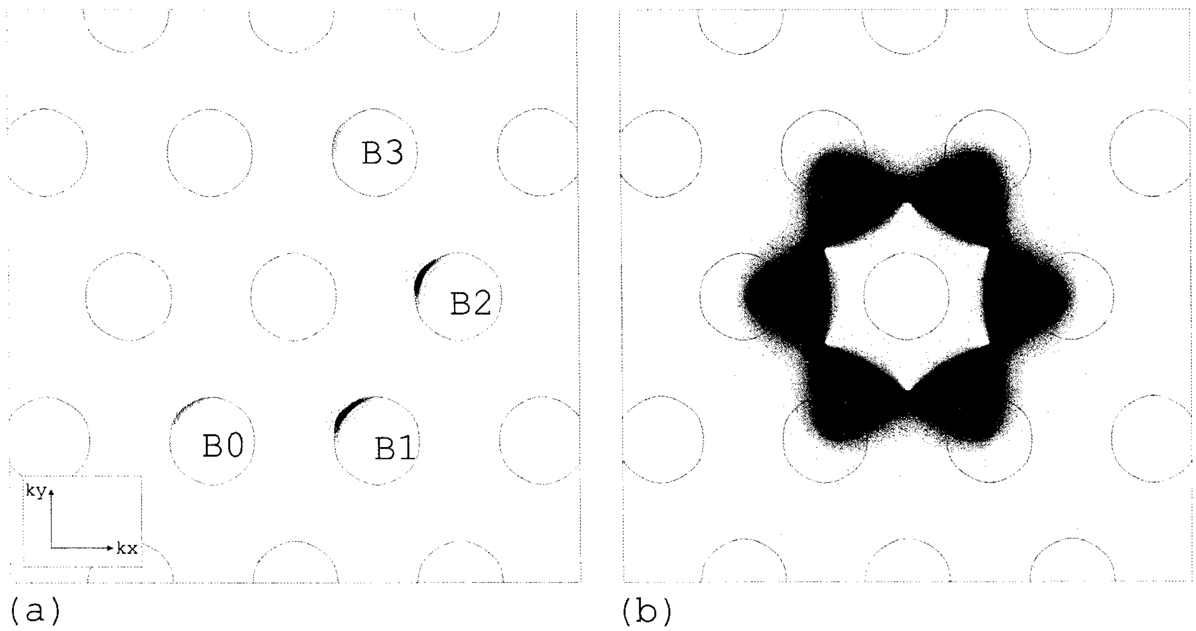

Figure 5.4: (a) Angular spectra of the refracted field for the $\phi = 10^{\circ}$ case. (b) Magnitude of the Fourier-coefficient function for the second frequency band.

in opposite directions because of the negative effective refractive index. Based on the directions of the $\mathbf{k}'_{\mathbf{G}}$-vectors, the propagation angles are estimated to be $\phi'_1 = -41 \pm 2^{\circ}$, $\phi'_2 = -32 \pm 2^{\circ}$, and $\phi'_3 = -26 \pm 2^{\circ}$ for B1, B2, and B3, respectively, where the margin of error is due to the limited resolution. Note that none of these propagation angles are in agreement with the angle predicted by Snell's law, $\phi' = -38.7^{\circ}$. The reason for the discrepancy is that the slope of the Fourier-coefficient function, $U^{(2)}(\mathbf{k})$, at the location of the peak in the beam spectrum shifts the peak to a different location. The propagation direction of the overall refracted beam is determined predominantly by the contribution of these three components.

The shapes of the beam spectra are determined (in part) by the incident Gaussian beam. However, from the envelope of the beams in Figs. 5.5(d), 5.5(e), and 5.5(f) one can see that these beams are not purely Gaussian. The distortion is, in the first place, caused by a clipping effect, which is in turn caused by the fact that the higher spatial frequency components of the incident Gaussian mode fall in the partial gap, and therefore, do not propagate inside the PhC. This effect is shown in the inset of

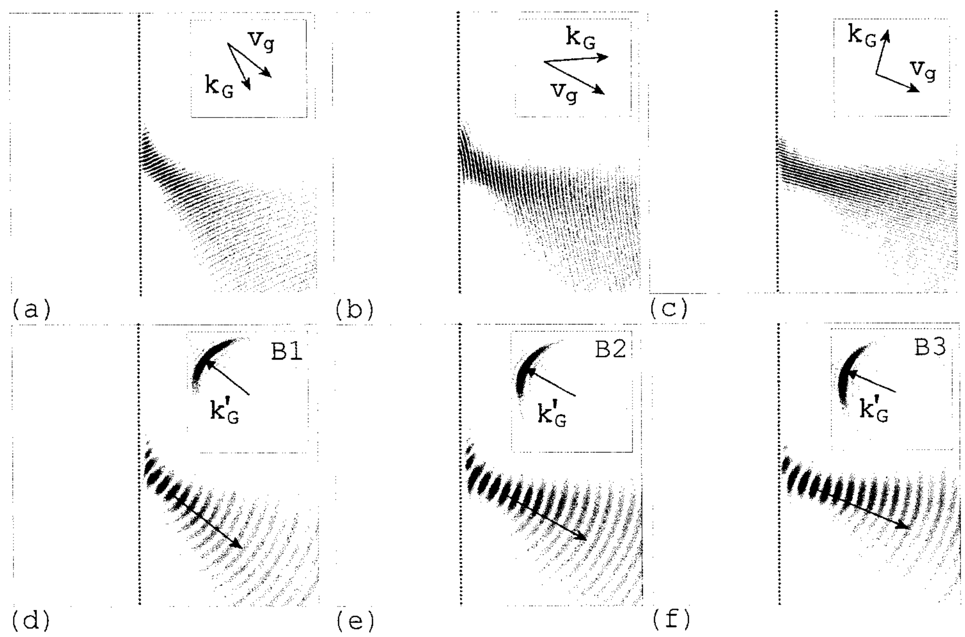

Figure 5.5: The normalized electric field distributions of the beam spectra labeled B1, B2, and B3 in Fig. 5.4(a) are respectively shown in (a), (b), and (c). The demodulated version of the fields in (a), (b), and (c) are shown in (d), (e), and (f). The insets show the associated beam spectrum for each refracted beam, with arrows indicating the corresponding wave vectors $\mathbf{k}'_{\mathbf{G}}$. The arrows in real space show the direction of propagation of the peak plane-wave component (anti-parallel to $\mathbf{k}'_{\mathbf{G}}$).

Fig. 5.3(b), where the dotted line represents the edge of the EFC, which separates it from the partial gap. Because the clipping effect is a result of the boundary condition, it determines the shape of the periodic Bloch-coefficient function $\alpha_p(\mathbf{k})$. Therefore it applies equally to all the beam spectra inside the PhC. In the second place, the distortion of the beams is also caused by the Fourier-coefficient function, $U^{(2)}(\mathbf{k})$. In addition to changing the propagation direction of the beams, $U^{(2)}(\mathbf{k})$ also distorts the beams. Contrary to the clipping effect, this distortion affects each refracted beam differently, because each beam spectrum is modulated by different parts of $U^{(2)}(\mathbf{k})$ where the magnitudes and slopes are different.

Reflected beams

Backward-diffracted waves are generated at the PhC interface to satisfy the periodic boundary condition, Eq. (2.34). The propagation direction of the different diffraction orders is obtained by substituting Eq. (2.34) into Eq. (2.30). The result is the well known grating equation

$$\sin \phi_q = \sin \phi_i + \frac{q\lambda_b}{a_{||}}, \tag{5.4}$$

where ϕ_i is the incidence angle, ϕ_q is the diffraction angle of the q-th backward-diffraction order, λ_b is the wavelength in the homogeneous medium, and $a_{||}$ is the lattice constant in the direction parallel to the interface, which is equal to a in this case. Note that the index q does not necessarily follow the numbering of the transverse rows of primitive cells as labeled in Fig. 5.2(a). This is because the zeroth backward-diffraction order must coincide with the specular reflection. Therefore, when analyzing the reflected field one must assign $q = 0$ to the row of primitive cells on which the $\mathbf{k}_{||}$-conservation condition takes place.

The reflected field at the PhC interface resembles the one generated by a one-dimensional diffraction grating. Yet the PhC interface has a peculiarity, for it can suddenly increase the reflectivity of incident waves falling within partial gaps. In such a case, one can compare the PhC interface with a reflection grating. For incident waves able to couple into the PhC, on the other hand, the reflected field is rather similar to the one generated by a transmission grating. Furthermore, in the latter case and under some circumstances, the Bloch-coefficient function may alter significantly the propagation direction of the backward-diffraction orders. We shall next analyze such phenomena.

Consider for example Fig. 5.6, which shows the spectra of the incident beam on the right-hand side on the $\mathbf{k}$-shell and the three backward-diffraction orders on the left-hand side. The spectrum of the zeroth diffraction order, which is located on the same level as the incident beam's spectrum, is much narrower than that of the incident beam, and its peak gives a diffraction angle of $\phi_0 = 17 \pm 0.5°$, which is significantly larger than the angle $\phi_0 = 10°$ predicted by the grating equation. The reason for this deviation can be found in the behavior of the fields inside the PhC. For this purpose, we consider the angular spectra shown in Fig. 5.3(b). To satisfy the boundary condition, a field is excited inside the PhC such that the tangential components of all the wave

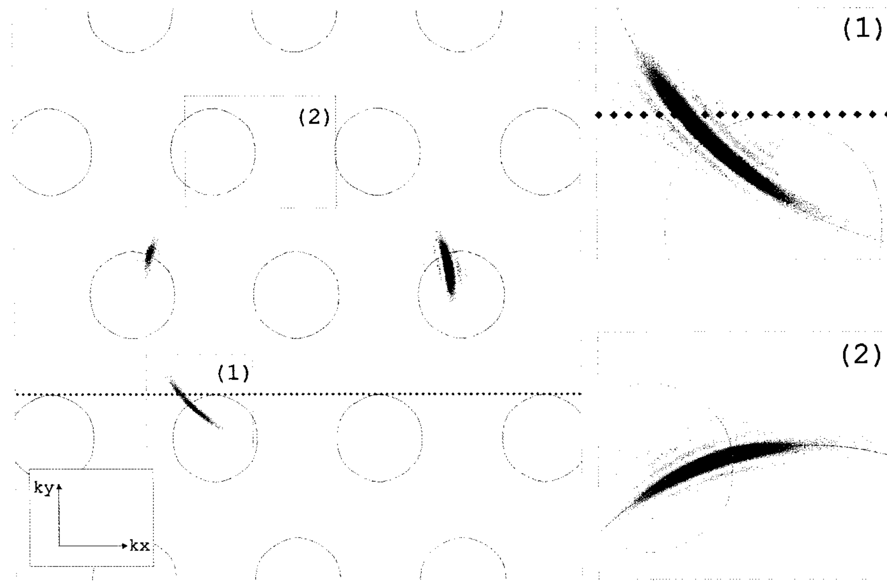

Figure 5.6: Angular spectra of the incident and reflected fields for the $\phi = 10°$ case. Insets (1) and (2) show, respectively, the spectrum of the -1 and $+1$ backward-diffraction order.

vectors are represented by similar wave vectors inside the PhC. Since the spectrum of the incident beam extends beyond the EFC (see the inset in Fig. 5.3(b)), not all of the wave vectors can match propagating plane waves inside the PhC. The result is that those plane waves with wave vectors beyond the EFC produce evanescent waves that cannot penetrate into the PhC. The wave must therefore be reflected. Those plane waves with wave vectors within the EFC can penetrate into the PhC, and they do not produce such strongly reflected waves. Therefore, the narrow zeroth order beam is mostly due to that part of the incident beam that could not penetrate into the PhC.

The peak of the beam spectrum located on the lower left-hand side on the **k**-shell represents the -1 backward-diffraction order, which is labeled A1 in Fig. 5.3(a). It gives a diffraction angle $\phi_{-1} = -46 \pm 0.5°$, which is approximately equal to the diffraction angle given by Eq. (5.4), $\phi_{-1} = -48.7°$. To explain the discrepancy we consider again the angular spectra in Fig. 5.3(b) and the angular spectra in Fig. 5.4(a). Observe that the -1 backward-diffraction order satisfies the $\mathbf{k}_{||}$-conservation condition on the refracted beam spectra in the row of primitive cells $q = -1$, which is predominantly formed by the beam spectra B0 and B1 in Fig. 5.4(a). These beam spectra are slightly shifted toward a less negative k_y value due to the slope of the Fourier-coefficient function. Consequently, the reflected beam spectrum is also shifted toward a less negative k_y value, resulting in a less negative propagation angle. In addition, we notice in Fig. 5.6 that part of the plane-wave components that form the spectrum of the -1 backward-diffraction order do not match their tangential wave-vector components with wave vectors on the EFCs in the row $q = -1$. This phenomenon is highlighted in the inset (1), where the dotted line indicates the limit between the EFC and the partial gap. The plane-wave components above the dotted line correspond to the -1 backward-diffraction order generated by the portion of the incident beam that cannot penetrate the PhC. They present strong amplitudes and so they contribute to shift the peak of this diffraction order toward a less negative k_y value. Furthermore, notice that the spectral distribution of this diffraction order looks similar to that of the incident beam; yet, it is wider. This is because the tangential components of B0 and B1 are projected onto a very oblique section of the **k**-shell, widening the spectrum of this order. This effect will be referred to as *projective beam scaling.*

One can also identify a very weak $+1$ backward-diffraction order on the upper part of the **k**-shell in Fig. 5.6, whose spectrum is enlarged in the inset (2). This diffraction order attempts to satisfy the boundary condition for the refracted beam B3 in Fig. 5.4(a), but in this case, only a small portion of the refracted beam's spectrum can be matched by components on the **k**-shell; the rest will exist as evanescent waves. Note that this diffraction order has a wide peak even though only a small portion of the refracted beam's peak is involved. The reason is that the peak is projected onto a highly oblique section of the **k**-shell. This fact agrees with the grating equation, since the $+1$ order cannot be fully generated with the incidence angle under consideration.

Note that the accuracy of the beam angle in the homogeneous medium is higher than for beams in the PhC. The reason is that the radius of the **k**-shell is larger than the radius of the EFC. As a result, the uncertainty in the beam angle for the homogeneous medium is smaller.

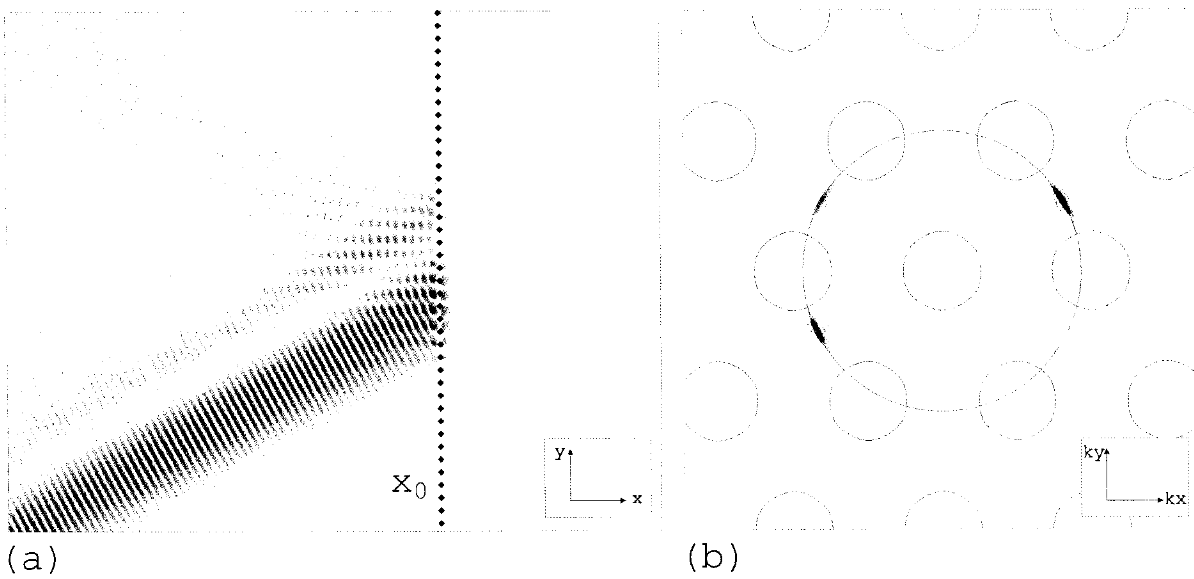

Figure 5.7: (a) Electric field distribution of the incident and scattered fields for the $\phi = 30°$ case. The PhC interface is located at $x_0 = 20a$. (b) Angular spectra of the field in (a).

5.1.3 Gaussian beam incident at 30°

Now we consider a Gaussian beam with a waist radius of $w_0 = 2.7a$, incident at an angle of $\phi = 30°$, onto the PhC interface located at $x_0 = 20a$. The incident and scattered fields obtained from the FDTD simulation are shown in Fig. 5.7(a), and the corresponding angular spectra are shown in Fig. 5.7(b), together with the EFCs. In this case, we note that the field penetrates only a small depth (on the order of a) into the PhC, forming evanescent waves at the interface to satisfy the boundary conditions. One can notice these evanescent waves in the **k**-space shown in Fig. 5.7(b) as the off-shell streaks extending inward from the incident and reflected beam spectra. The reason for the lack of penetration is that the spectrum of the incident beam is located in the partial gap between the $q = 0$ and $q = +1$ rows of primitive cells. Therefore the incident beam is completely reflected.

Because no propagating modes are excited inside the PhC, it acts purely as a reflection grating, generating the zeroth and -1 diffraction orders. The peak of the zeroth order beam spectrum gives a propagation angle of $\phi = 30 \pm 0.5°$ with respect to the normal, and that of the -1 order gives a propagation angle of $\phi = -25 \pm 0.5°$, which means that it propagates almost exactly into the incident beam. Both of these angles agree with those obtained from the grating equation, Eq. (5.4).

5.1.4 Gaussian beam incident at 55°

Finally, we consider a Gaussian beam with a waist radius of $w_0 = 2.7a$, incident at an angle of $\phi = 55°$ onto the PhC interface, which is located at $x_0 = 10a$. This gives the beams inside the PhC more room to get a better definition of their spectra, which would otherwise be rather faint. The incident, reflected, and refracted fields obtained from the FDTD simulation are shown in Fig. 5.8(a).

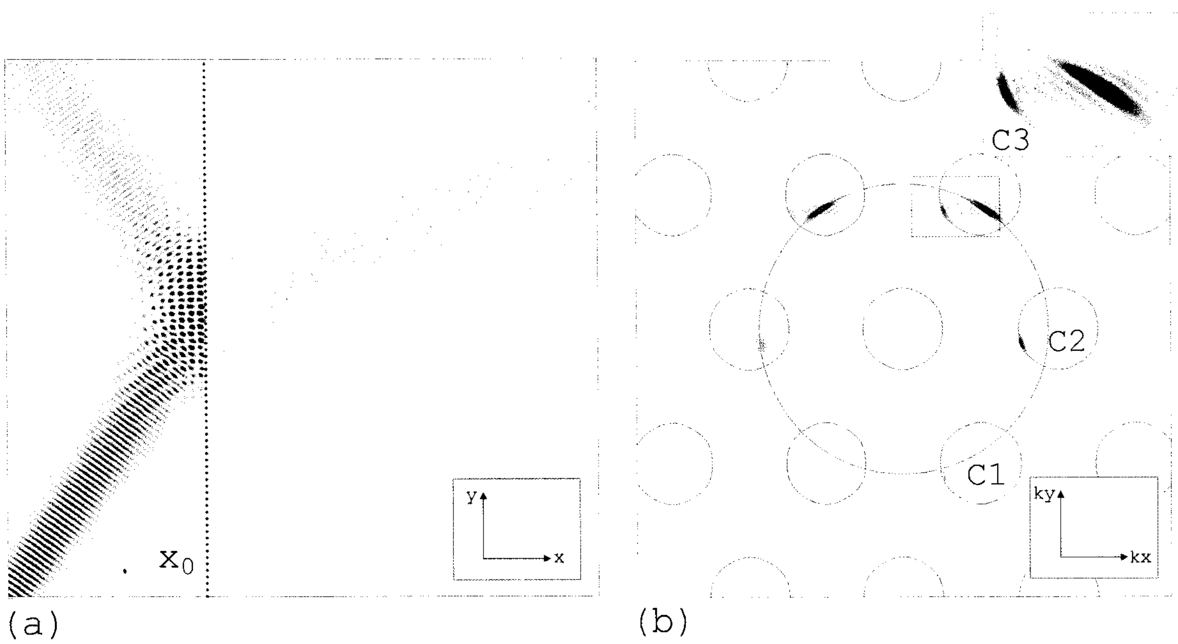

Figure 5.8: (a) Electric field distribution of the incident, reflected, and refracted fields for the $\phi = 55°$ case. The PhC interface is located at $x_0 = 10a$. (b) Angular spectra of the field in (a).

The $\mathbf{k}$-space representation of the fields is shown in Fig. 5.8(b). Note that in this case, the dominant refracted beams are C2 and C3. This differs from the 10° case, where the spectra labeled B1 and B2 in Fig. 5.4(a) dominate. This difference is caused by the magnitude of the Fourier-coefficient function (shown in Fig. 5.4(b)) at the locations of the beam spectra. Furthermore, observe that the $\mathbf{k}_{||}$-components of the incident

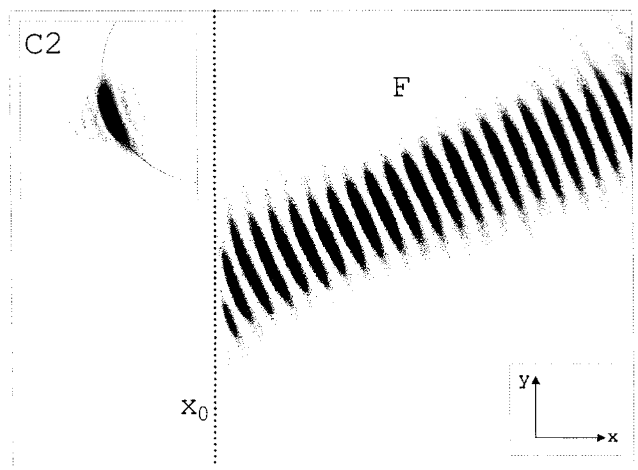

Figure 5.9: Normalized electric field distribution of the demodulated version of the beam spectrum labeled C2 in Fig. 5.8(b). The normalized beam spectrum is shown in the inset.

beam are matched by $\mathbf{k}_{||}$-components on the EFCs located in the row of primitive cells with $q = 1$, which does not include the 1BZ. The refraction of the beam in the PhC is therefore anomalous.

The spectrum of the incident beam on the $\mathbf{k}$-shell of the homogeneous medium is very oblique. Therefore, due to the projective scaling onto the EFC, it gives a much narrower peak (see inset in Fig. 5.8(b)), and thus a much wider beam inside the PhC. Since the beam spectra inside the PhC are much narrower, they are not affected as severely by the Fourier-coefficient function, $U^{(2)}(\mathbf{k})$. Therefore, the beams are less distorted, and their propagation directions are closer to the value given by Eq. (5.3) than what we had for the 10° case in Section 5.1.2. The propagation angles and the spectral distributions of the dominant refracted beams (those located in the 1HAZ) are approximately identical. The estimated refracted angle based on the beam spectra is $\phi' = 22° \pm 2°$, which is in good agreement with the result of $\phi' = 22.6°$ obtained from Eq. (5.3).

The projective scaling causes some distortion in the beams due to the curvature of the EFC. To see this, we focus our discussion on the spectrum of the refracted beam labeled C2 in Fig. 5.8(b). The normalized field distribution of its demodulated version is shown in Fig. 5.9 and the normalized spatial frequency spectrum is shown in the inset. Observe that the phase fronts above the beam axis are curved, converging to the point labeled F, while those below the beam axis remain flat. After the point F, the wave fronts both above and below the beam axis start to diverge in a non-symmetrical fashion. The distortion can also be detected in its spectral distribution. Although the spectrum is very narrow, a small asymmetry is visible in the spectral profile – the peak is slightly shifted to a larger spatial frequency. The projective scaling is a consequence of the anomalous refraction. Since it allows refraction at large incidence angles, the spectrum of the incident beam is severely modified, producing asymmetric refracted beams.

5.2 The square-lattice PhC

This section studies the propagation of Gaussian beams from a homogeneous dielectric medium with refractive index $n_b = 3.6$ into a half space PhC composed of a square lattice of air-holes of radius $0.4a$ etched in the same dielectric medium. The two-dimensional space is assumed to be infinite and homogeneous in the z-direction. For the PhC half space, the plane of periodicity is in the (x, y)-plane. The interface between the homogeneous medium and the PhC is in the (y, z)-plane in the Γ-X direction of the crystal. Beams with normalized frequency $a/\lambda = 0.3$ and various propagation angles are considered for the analysis.

The photonic band structure of the PhC under consideration is shown in Fig. 2.2(b). On it, the horizontal line indicates the operation frequency for the present case. At this frequency, the second and third bands overlap. Furthermore, notice that for frequencies around the operation frequency, the second band approaches in shape to an inverted parabola centered at Γ, having therefore negative slope; the third band is similar to a positive parabola centered at M, and hence, its slope is positive. This indicates that the group velocity is negative for Bloch modes in the second frequency band, while it is positive for those in the third band.

The EFC in the repeated zone scheme is shown in Fig. 5.10(a). It is composed of square-like contours of two different sizes. The large contours are centered at the M points of the reciprocal space and describe modes in the third band. On the other hand, the small contours are centered at the Γ points and describe modes in the second band. The circular contour stands for the homogeneous medium **k**-shell at the operation frequency. The vertical dashed line indicates the orientation of the interface, the dashed square at the center represents a reciprocal primitive cell, and the parameter q on the right-hand side indicates the transverse row-number for the row of primitive cells perpendicular to the interface.

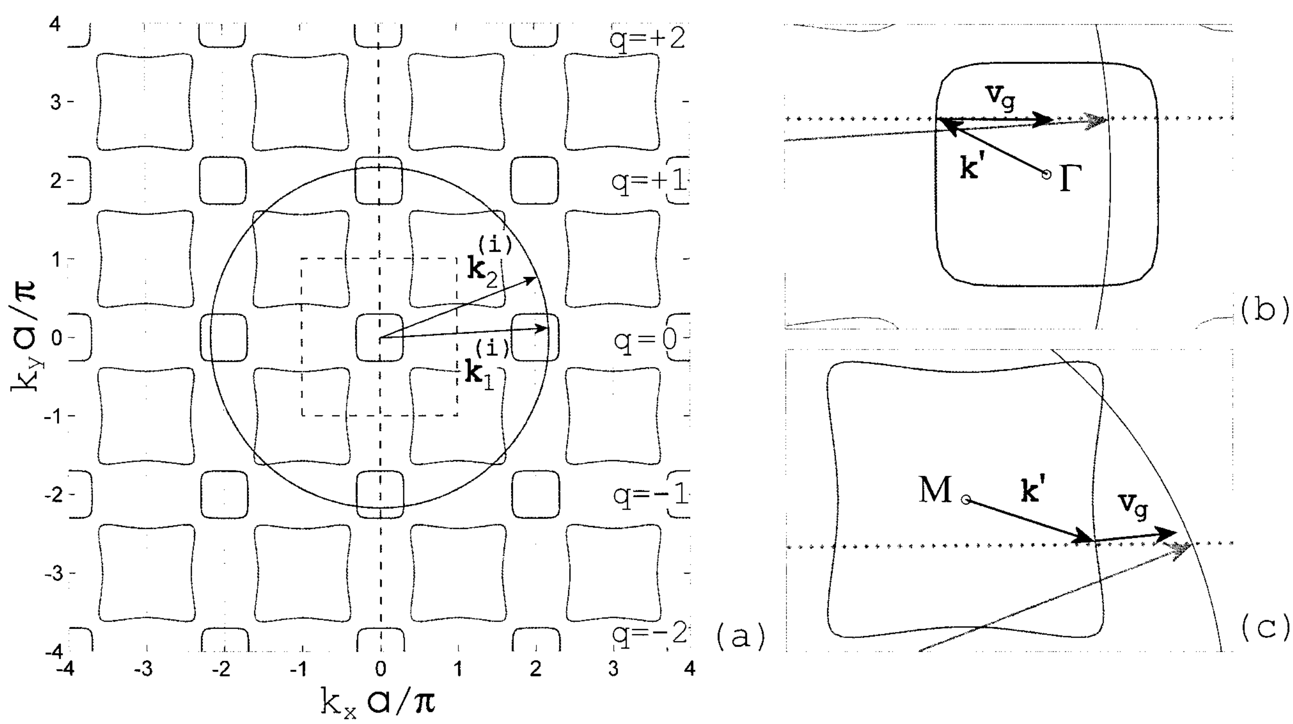

Figure 5.10: (a) The EFC in the repeated zone scheme for the square-lattice PhC under consideration and the **k**-shell for the homogeneous medium, both at the operation frequency. The vertical dashed line indicates the orientation of the interface. (b) Refraction for modes in the second frequency band. (c) Refraction for modes in the third frequency band.

5.2.1 Ranges of incidence angle

Since the EFCs are not circular the refraction phenomenon does not follow the generalized refraction equation deduced in the previous section. However, the refraction direction is easily obtained as the direction of the group velocity vector. In this case the refracted Bloch waves behave differently depending on whether they satisfy the boundary conditions with modes in the second or third frequency bands. The incident wave vectors, $\mathbf{k}_1^{(i)}$ and $\mathbf{k}_2^{(i)}$, shown in Fig. 5.10(a) illustrate the phenomenon. For example, the plane wave denoted by $\mathbf{k}_1^{(i)}$ is refracted with negative group velocity as shown in Fig. 5.10(b); hence, the vector $\mathbf{v_g}$ must be normal to a point on the left-hand side of the EFC, pointing toward the inside of the contour. On the other hand, the plane wave denoted by $\mathbf{k}_2^{(i)}$ is refracted with positive group velocity as shown in Fig. 5.10(c). The vector $\mathbf{v_g}$ is therefore normal to a point on the right-hand side of the EFC, pointing toward the outside of the contour.

The various conditions that exist depending on the incidence angle are summarized in Table 5.2 for incidence angles ranging from 0° to 90°. It also indicates the number, q, for the row of primitive cells that contain the EFCs where the $\mathbf{k}_{||}$-conservation condition is satisfied and whether the refracted wave has positive (+) or negative (-) group velocity. The behavior follows the same pattern for negative angles.

Table 5.2: Propagation conditions and primitive cell row number as functions of the incidence angle. $^{(*)}$ The boundary between $q = 0$ and $q = 1$ corresponds to $\phi = 27.5°$.

incidence angle	Condition	q	sgn(v_g)
$0° < \phi_i < 8°$	Band 2 mode	0	-
$8° < \phi_i < 10.6°$	partial gap		
$10.6° < \phi_i < 47.8°$	Band 3 mode	0,1$^{(*)}$	+
$47.8° < \phi_i < 52.3°$	partial gap		
$52.3° < \phi_i < 90°$	Band 2 mode	1	-

Examples of each of these conditions are now considered in more detail. In each case, we have a Gaussian beam with its waist at the left-hand edge of the homogeneous medium from where it is launched. It then propagates from left to right toward the interface between the homogeneous medium and the PhC. At the interface, various refracted and reflected beams are generated. We shall study them using the FDTD-Fourier method of analysis.

5.2.2 Gaussian beam incident at 0°

First, we consider a Gaussian beam with waist radius $w_0 = 2.7a$ at $x = 0$, normally incident onto the PhC interface located at $x = 20a$. The corresponding electric field distribution is shown in Fig. 5.11(a).

The incident Gaussian beam impinges onto the PhC interface and generates three reflected waves, which correspond to zeroth, -1, and $+1$ backward-diffractions of orders. The -1 and $+1$ diffraction orders are respectively labeled A1 and A2 in Fig. 5.11(a); the specular reflection falls on top of the incident beam and is not visible in the real space. The transmitted field, on the other hand, experiences *super-collimation* due to the EFC shape. The EFCs are squarish geometries composed of straight sides and rounded corners. Particularly, for the EFCs in the central row of primitive cells ($q = 0$), the vertical sides cover the range $-0.3 < k_y a/\pi < 0.3$ with straight sections ranging over $-0.2 < k_y a/\pi < 0.2$. It follows that the structure is capable of collimating plane waves with propagation angles in the range $-8° \leq \phi \leq 8°$. For the present case, the numerical aperture of the incident Gaussian beam is $NA = \sin(6.2°)$; thus, one can conclude that most of its plane-wave components are collimated into the PhC[1].

The magnitude of the angular spectra of the field distribution in Fig. 5.11(a) is shown in Fig. 5.11(b). The **k**-shell for the homogeneous dielectric is represented by the superimposed circle and the EFC in the repeated zone scheme for the second frequency band is indicated by the squarish contours. The angular spectra of the refracted beam are located on the left-hand side of the EFCs due to the negative group velocity on this section of the frequency band and the angular spectra of the three backward-diffraction orders are located on the left-hand side of the **k**-shell. We shall proceed to study in more detail the reflected and refracted beams by analyzing their angular spectra.

[1] For a numerical aperture of $\sin(6.2°)$, approximately 86% of the energy is carried by plane-wave components with propagation angles in the range $-6.2° \leq \phi \leq 6.2°$ [67]

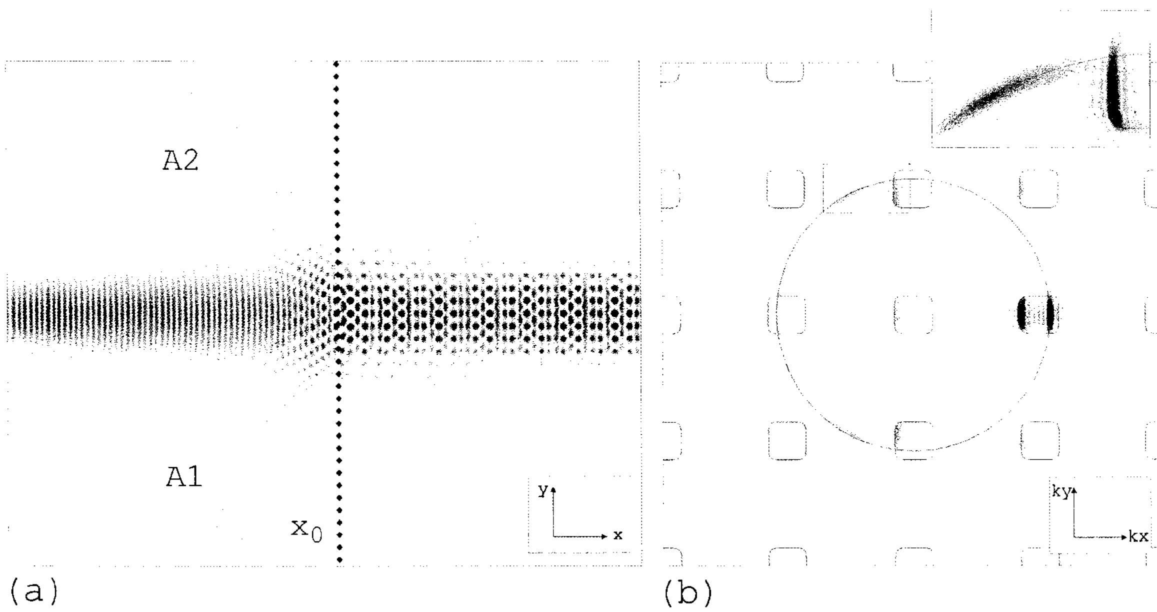

Figure 5.11: (a) Electric field distribution of the incident, reflected, and refracted beams for the $\phi = 0°$ case. The PhC interface is located at $x_0 = 20a$. (b) Angular spectra of the field in (a).

Refracted beams

The magnitude of the spectra associated with the transmitted field and the magnitude of the Fourier-coefficient function for the second band, $U^{(2)}(\mathbf{k})$, are shown in Figs. 5.12(a) and 5.12(b), respectively. In this case, the transmitted field's spectra are severely suppressed by $U^{(2)}(\mathbf{k})$ in primitive cells beyond the 1HAZ. However, spectra with noticeable amplitudes exist in the 1HAZ and the 1BZ. Here we shall limit the analysis to the dominant beam spectrum labeled B0 in Fig. 5.12(a), approximating the field inside the PhC by a single beam i.e., *single beam behavior*.

The values of the Fourier-coefficient function that determine the magnitude of the spectrum B0 are shown in the inset of Fig. 5.12(b). In the first place, we notice that the function is fairly constant along the straight part of the EFC. This fact is of great importance for it suggests that the Fourier-coefficient function does not distort significantly the collimated plane-wave components. In the second place, the function shows a sudden slope on both corners of the EFC, which indicates that not-collimated plane-wave components (in the range $0.2 < |k_y a/\pi| < 0.3$) are suppressed by the sharp

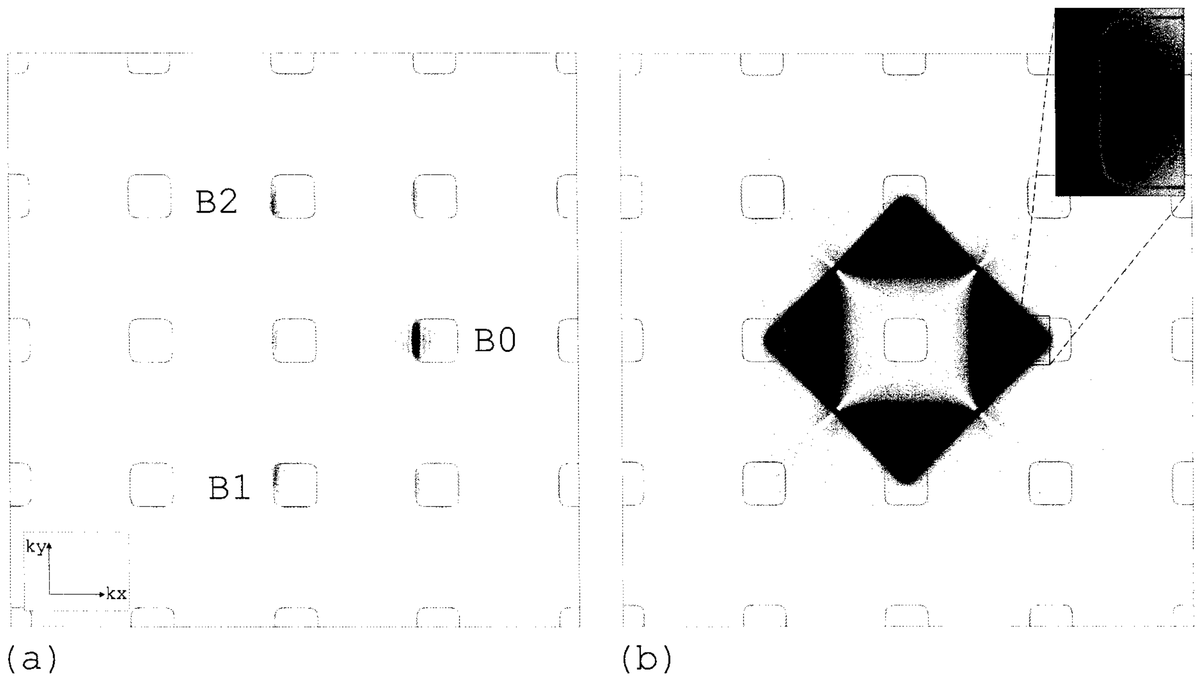

Figure 5.12: (a) Angular spectra of the refracted field for the $\phi = 0°$ case. (b) Magnitude of the Fourier-coefficient function for the second frequency band.

slope of $U^{(2)}(\mathbf{k})$. The effects of the Fourier-coefficient function on the beam spectrum B0 are clearly illustrated in Fig. 5.13(a). It shows the normalized magnitude of the spectrum B0, projected onto the k_y axis. The solid lines indicate the boundary of the EFC, the dotted lines indicate the angular range for super-collimation, and the dashed curve describes the normalized spectrum of the incident Gaussian beam projected onto the k_y axis. One can observe that the spectrum B0 conserves the Gaussian characteristics of the incident spectrum within the collimation range, $|k_y a/\pi| < 0.2$. On the other hand, for $0.3 < |k_y a/\pi| < 0.2$, the spectrum is severely attenuated by the slope of $U^{(2)}(\mathbf{k})$ and for $|k_y a/\pi| > 0.3$, the spectrum consists of evanescent modes that arise to satisfy the boundary conditions for the angular components of the incident Gaussian spectrum that fall within the partial gaps. These plane-wave components are identified in the inset of Fig. 5.11(b) as the tips of the incident Gaussian spectrum outside the EFC.

The implications in the real domain are visible in Fig. 5.13(b), which illustrates the coupling process between the incident Gaussian mode and the Bloch space-harmonics that constitute B0. The dashed line indicates the PhC interface. The beam on the left-hand side of the interface is the incident Gaussian beam; the one on the right-hand side is the real-space representation of B0. The peak amplitude of B0 in real space represents 88% of the incident beam's peak amplitude. Hence it is a reliable indicator of the field behavior inside the PhC. We notice that the bulk of the beam is collimated, keeping flat phase fronts and constant amplitude as it propagates through the PhC. The collimated portion is free of distortion, following the same Gaussian profile as the incident beam. However, one can notice that the phase fronts are curved above and below the collimated bulk. This effect is due to the plane-wave components that fall on the rounded corners of the EFC; they propagate in directions pointed by the arrows in the inset of Fig. 5.13(b) due to the negative group velocity. Notice that the plane-wave components on the lower corner of the EFC propagate upward generating the divergent field above the beam's body and those on the upper corner propagate downward producing the same effect below the beam's body. This self-interference process creates the fringes present above and below the collimated portion.

Reflected beams

In order to study the reflected beams we consider the angular spectra in Fig. 5.11(b). In the figure, the angular spectra of the +1 and −1 backward-diffraction orders are located on the left-hand side of **k**-shell at the same level as the rows of primitive cells $q = +1$ and $q = -1$, respectively. The amplitude of the zeroth diffraction order is very small, and although not visible in the real domain, it can be detected in the **k**-space as the angular spectrum located on the left-hand side of the **k**-shell at the same level as the incident spectrum.

The propagation directions of the two higher backward-diffraction orders, as obtained from the peaks of their angular spectra, are $\phi_{+1} = 63° \pm 0.5°$ and $\phi_{-1} = -63° \pm 0.5°$. They differ from the angles predicted by the grating equation, $\phi_{+1} = 67.2°$ and $\phi_{-1} = -67.2°$. This discrepancy follows the same explanation given in Section 5.1.2 for the 10° case in the hexagonal-lattice PhC. In the present case, the +1 and −1

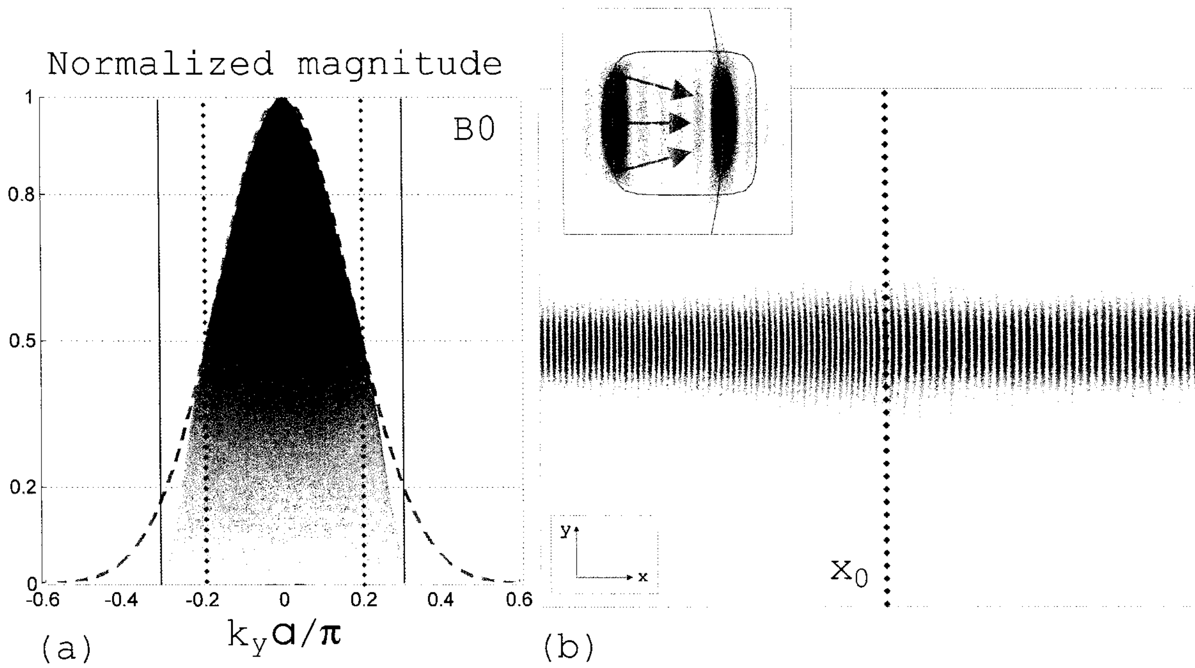

Figure 5.13: (a) Magnitude of the beam spectrum B0 projected onto the k_y axis. The dashed curve denotes the incident Gaussian beam's spectrum, the solid lines indicate the EFC boundaries, and the dotted lines indicate the range for super-collimation. (b) Electric field distribution of the incident beam and B0. The vertical line denotes the PhC interface and the inset shows the angular spectra of the field distribution.

diffraction order satisfy the boundary conditions with the refracted-beam spectra in the row of primitive cells $q = +1$ and $q = -1$, respectively. The spectra in the row $q = -1$ is mostly concentrated in the spectrum B1 and those in the row $q = +1$ are mostly concentrated in the spectrum B2; hence, the two higher diffraction orders are predominantly determined by these two spectra. The discrepancy in the diffraction angles arises because the Fourier-coefficient function shifts the spectra B1 and B2 toward a lower spatial frequency along the k_y axis. This is illustrated in the inset of Fig. 5.11(b) for B2. As a result, the peaks of the spectra of the two backward-diffraction orders are also shifted toward a smaller spatial frequency along the same direction producing smaller diffraction angles for both backward-diffraction orders.

One can also note that the angular spectra of higher backward-diffraction orders widen as a consequence of the projective scaling onto an oblique section of the **k**-shell. This phenomenon is also highlighted in the inset of Fig. 5.11(b) for the +1 diffraction order. As a result, the two higher diffraction orders have narrower beam-width than the incident Gaussian beam, and therefore, diverge faster.

5.2.3 Gaussian beam incident at 28°

Now we consider a Gaussian beam of waist radius $w_0 = 2.7a$ at $x = 0$ incident with a propagation angle of 28°. The electric field distribution is shown in Fig. 5.14(a). The Gaussian beam is launched from the lower left corner and hits the PhC interface located at $x_0 = 15a$. Two backward-diffraction orders are generated at the interface; one falls on top of the incident beam and the other is the specular reflection. The magnitude of the angular spectra of the field in Fig. 5.14(a) is shown in Fig. 5.14(b). The EFC in the repeated zone scheme for the third frequency band and the homogeneous dielectric **k**-shell, both at the operation frequency, are indicated respectively by the squarish contours and the circle superimposed on the figure. The two reflections are identified as the spectra on the left-hand side of the **k**-shell. Their angular profiles are similar to that of incident Gaussian beam. Notice that the angular spectra of Bloch modes are now located on the right-hand side of the EFCs due to the positive group velocity on this section of the frequency band.

Refracted beams

To analyze the refraction phenomenon we consider the magnitude of the angular spectra associated with the refracted field, which is shown in Fig. 5.15(a), and the magnitude of the Fourier-coefficient function for the third frequency band, $U^{(3)}(\mathbf{k})$, shown in Fig. 5.15(b). In this case, the refracted field exhibits *multiple-beam behavior* imposed by two dominating beam spectra labeled C0 and C1 – this is in contradistinction with the previous case in Section 5.2.2, where only one beam spectrum dominates. The other beam spectra are suppressed by the Fourier-coefficient function. Therefore, for the following analysis, we shall consider only the two dominant spectra, C0 and C1.

The two dominant spectra experience slight distortions due to the Fourier-coefficient

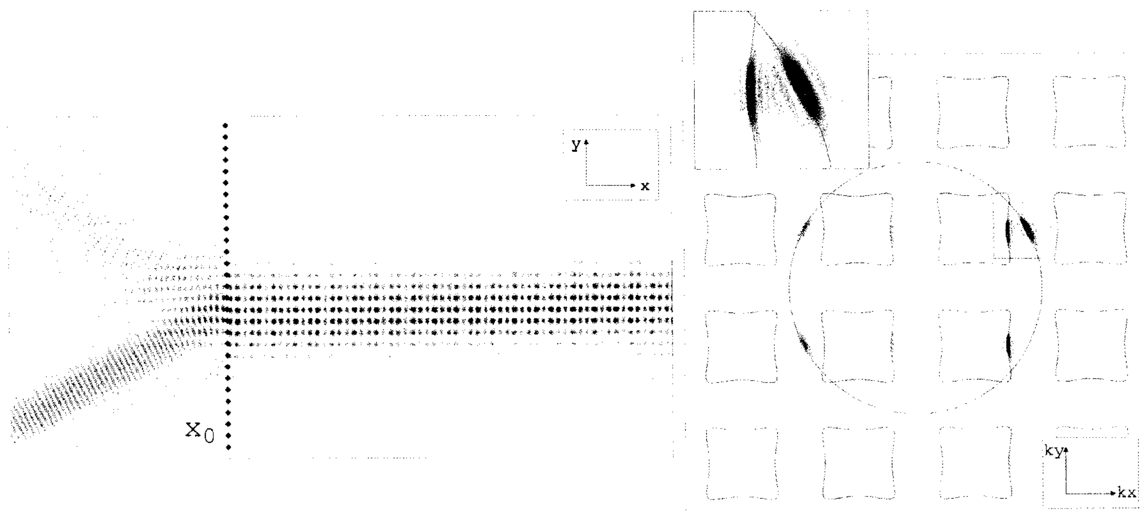

(a) (b)

Figure 5.14: (a) Electric field distribution of the incident, reflected, and refracted beams for the $\phi = 28°$ case. The PhC interface is located at $x_0 = 15a$. (b) Angular spectra of the field in (a).

function and the boundary conditions. To understand such distortions we consider Fig. 5.15(c). It shows the normalized magnitudes of the two dominant beam spectra projected onto the k_y axis. In the present case, the incident Gaussian mode satisfies the $\mathbf{k}_{||}$-conservation condition with the spectra in the same row of primitive cells as C1 (see inset of Fig. 5.14(b)). The peak of the Gaussian spectrum projected onto the k_y axis is slightly shifted toward a higher spatial frequency from the center of the EFCs in such row of primitive cells[2], which is located at $k_y = \pi/a$. However, we note that C1 does not locate its peak at the same k_y location as the incident spectrum, but it is slightly shifted toward a smaller spatial frequency from the center of the EFC. On the other hand, the peak of the spectrum C0 is shifted toward a higher spatial frequency from the center of its respective EFC, which is located at $k_y = -\pi/a$. The magnitude of the shift corresponds exactly to the relative shift of the incident Gaussian beam. In addition, we notice that the two spectra have similar shapes, describing quasi-Gaussian distributions with elongated left tail, and they have slightly different amplitudes with the peak amplitude of C0 being around 98% the peak amplitude of C1.

[2]The incident Gaussian spectrum, projected onto the k_y axis, locates its peak at the center of the EFCs in the row $q = +1$ when the incidence angle is 27.5°

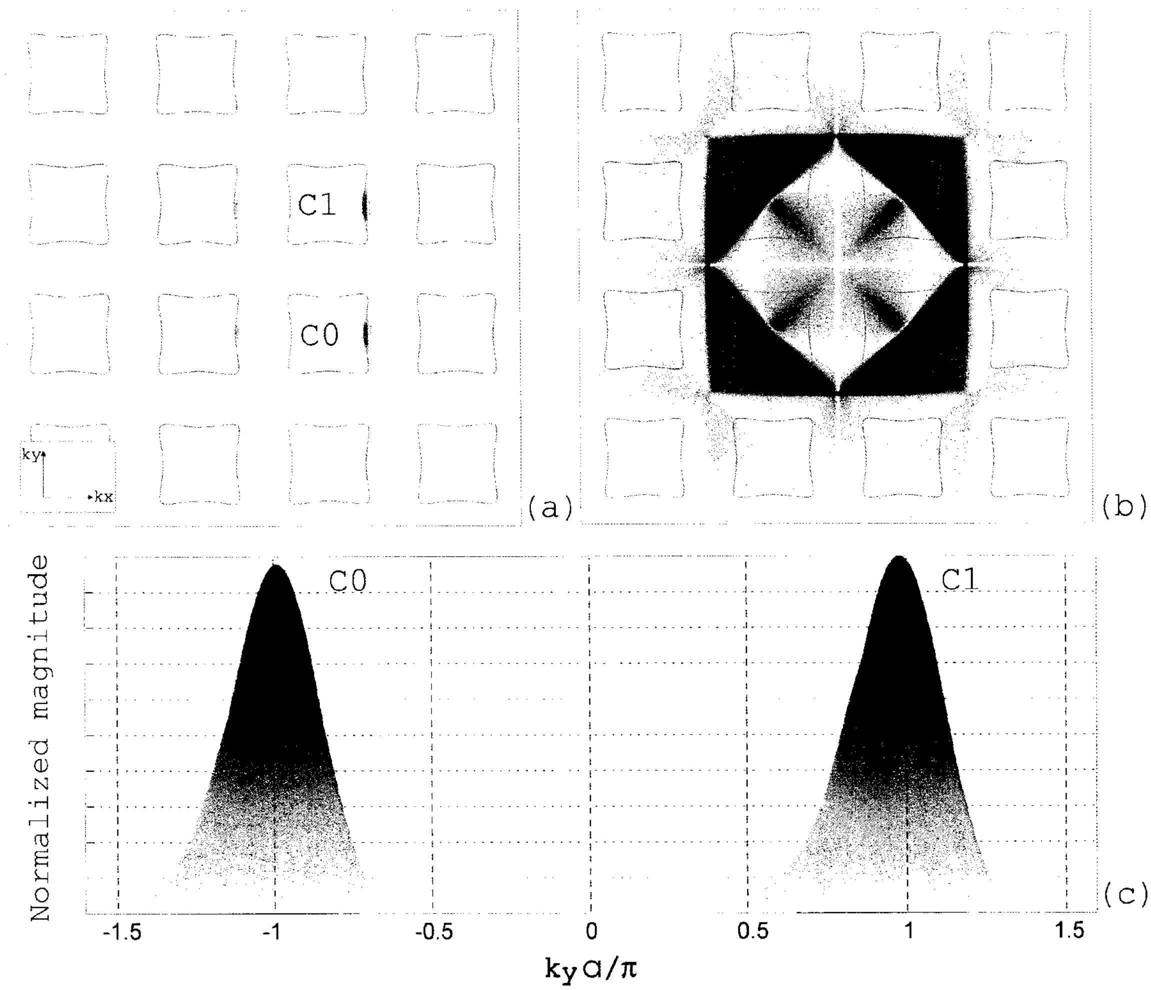

Figure 5.15: (a) Angular spectra of the refracted field for the $\phi = 28°$ case. (b) Magnitude of the Fourier-coefficient function for the third frequency band. (c) Magnitude of the dominant beam spectra C0 and C1 projected onto the k_y axis. The EFCs associated with C0 and C1 are centered at $k_y = -\pi/a$ and $k_y = \pi/a$, respectively.

In order to illustrate clearly the nature of these distortions, we first obtain numerically the Bloch-coefficient function as

$$\alpha(\mathbf{k}-\mathbf{G}_q) = \frac{\Psi_r(\mathbf{k}-\mathbf{G}_q)}{U^{(3)}_{\mathbf{G}_q}(\mathbf{k}-\mathbf{G}_q)}, \tag{5.5}$$

where $\mathbf{G}_q$ is the reciprocal lattice vector associated with a particular primitive cell and $\mathbf{k}$ takes values within the 1BZ and $\Psi_r(\mathbf{k})$ is the angular spectra of the refracted field. Eq. (5.5) follows directly from Eq. (3.4) by considering only one element of the summation, i.e., making $\mathbf{G} = \mathbf{G}_q$. The Bloch-coefficient function is obtained for the reciprocal lattice vector, $\mathbf{G}_q$, associated with the beam spectrum C1. Then, we replicate the Bloch-coefficient function in the primitive cell associated with C0 in order to reproduce the angular spectra of both C0 and C1 as

$$\Psi_{\mathrm{C0,C1}}(\mathbf{k}) = U^{(3)}(\mathbf{k}) \sum_{\mathbf{G}_q} \alpha(\mathbf{k}-\mathbf{G}_q), \qquad \mathbf{G}_q \in \{\mathbf{G}_0, \mathbf{G}_1\}, \tag{5.6}$$

where $\mathbf{G}_0$ and $\mathbf{G}_1$ are the respective reciprocal lattice vectors associated with the primitive cells where C0 and C1 are located. At this point, we shall remark that the angular spectra obtained numerically do not represent the real amplitudes. This is because the FFT routine takes into account the area over which the fields are distributed in real space in order to perform the transformation. However, the different Bloch space-harmonics are distributed over more or less the same area in the real space. Consequently, their relative amplitudes coincide with the relative amplitudes of the real angular spectra but scaled by a constant factor[3]. It follows that the values resulting from Eqs. (5.5) and (5.6) will be scaled as well. It is therefore convenient to consider normalized values in this case.

The magnitudes of the resulting spectra C0 and C1, projected onto the k_y axis, are denoted by the solid curve in Fig. 5.16. In addition, the figure shows the magnitude of the replicated Bloch-coefficient function (circular markers) projected onto the k_y axis, and the magnitudes of $U^{(3)}(\mathbf{k})$ that modulate the Bloch-coefficients (cross markers).

[3]Refer to Section 4.2.3 for details.

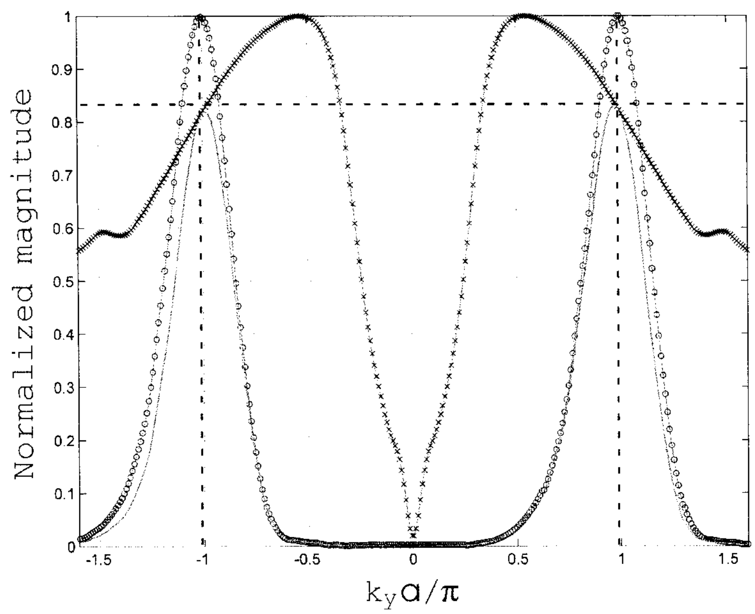

Figure 5.16: (a) Magnitude of the angular spectra C0 and C1 obtained per Eq. (5.6) (solid line), normalized magnitudes of the Bloch-coefficient function replicated at $\mathbf{G}_0$ and $\mathbf{G}_1$ (circlular markers), and normalized magnitudes of the Fourier coefficients that modulate the Bloch-coefficient function (cross markers). All functions are projected onto the k_y axis.

The vertical lines indicate the center of each EFC and the horizontal dashed line indicates the peak value of C1. These results reveal that, in this case, the shape of the beam spectra is defined essentially by the Bloch-coefficient function. That is, the left tail elongation on C0 and C1 is predominantly the result of the projective scaling and the effect of the boundary conditions that define the overall Bloch-mode profile, $\alpha(\mathbf{k})$. The Fourier-coefficient function, on the other hand, produces slight changes on their amplitudes and positions. For instance, the tail elongation in C0 is less pronounced than in C1 because the amplitudes of $U^{(3)}(\mathbf{k})$ rather suppress the tail effect. Furthermore, the Fourier-coefficient function also causes the peak amplitude of C0 to be smaller than the peak of C1.

We now proceed to analyze the distortion effects in the real domain. The demodulated versions of the normalized electric field distributions associated with the spectra C0 and C1 are shown in Figs. 5.17(a) and 5.17(b), respectively. The insets illustrate the normalized magnitude of their angular spectra with the EFC superimposed. The EFC has concave curvature (curves outwards) on the central section. The approximate

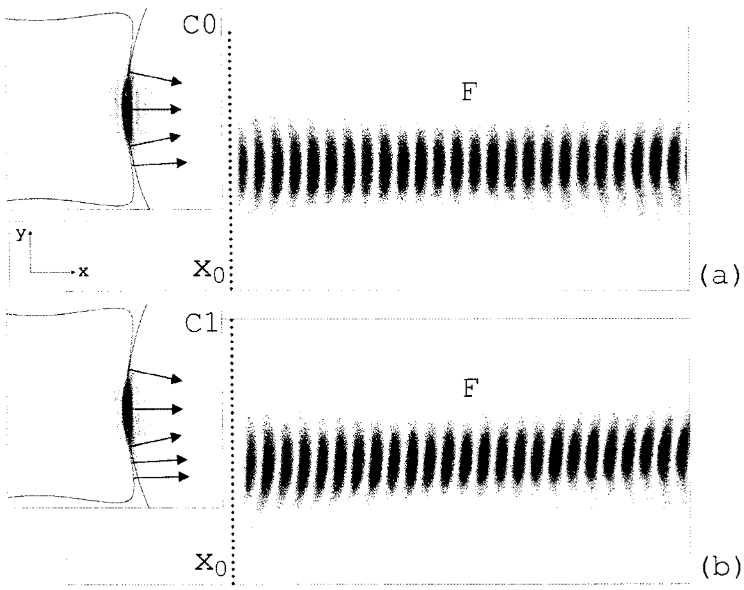

Figure 5.17: Electric field distribution of the two dominant beam spectra (a) C0 and (b) C1. The normalized magnitudes of their respective angular spectra are shown in the insets. The concave curvature shown with the EFC denotes its radius of curvature.

radius of curvature is $2.5a/\pi$. Therefore, for propagation toward the right, the angular components on the curved section behave as if they were located on the left hand side of an homogeneous **k**-shell, which indicates negative refraction. This is therefore an example of negative refraction without negative effective refractive index [68].

The focusing effect due to the negative refraction phenomenon can be observed in the figures. Notice that the wave fronts above the beam axis are curved converging slowly to the point labeled F and then diverge in the same fashion. The slow convergence is due to the large radius of curvature of the EFC. The wave fronts below the beam axis also converge to the point F; yet, they present distortion caused by the angular components that fall out of the concavely curved region of the EFC. These angular components experience a sudden change of direction due to the inflection point on this section of the contour. This phenomenon is illustrated by the arrows in the insets, which indicate the direction of the group velocity vector at the different points on the EFC. The angular components responsible for such distortion correspond precisely to the elongated tails of both spectra. Hence the distortion is more pronounced in C1 for its tail goes further beyond the section defined by the radius of curvature.

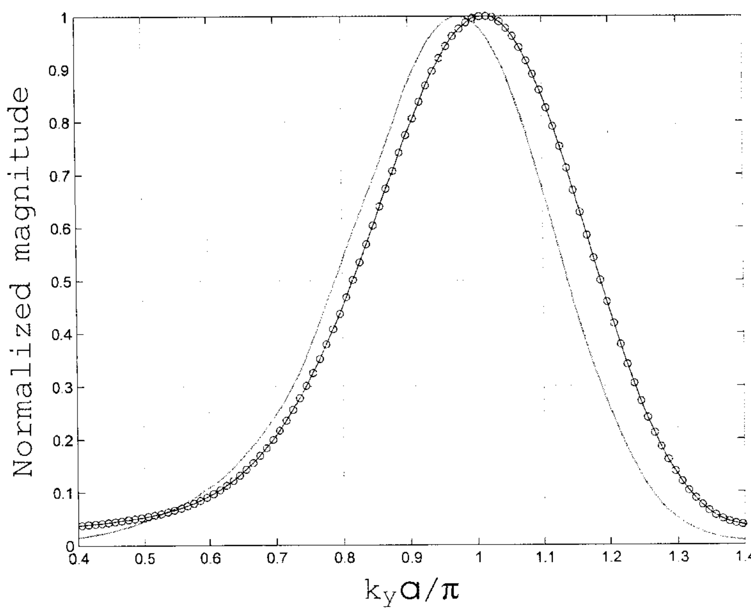

Figure 5.18: Magnitude of the incident beam's angular spectrum (circular markers) and normalized magnitude of the angular spectrum C1 (solid line), both projected onto the k_y axis.

Reflected beams

We shall continue with the analysis of the reflected beams. We first notice that because the EFCs are centered at the M point of the reciprocal primitive cell, they are shifted in the k_y axis by a factor of π/a from the center of their corresponding row of primitive cells, q. This can be seen in Figs. 5.10(a) and 5.10(c). However, the reciprocal primitive cell is not unique and one can redefine it by redefining the reciprocal lattice vector. Hence, we can add a fixed vector to the reciprocal lattice vectors, $\mathbf{G}$, in order to shift all the primitive cells in the k_y axis by an amount of π/a so each EFC is contained in a single primitive cell. Furthermore, to be consistent with the grating equation, the row of primitive cells $q = 0$ must correspond to that of the refracted-beam spectra matching their tangential wave vectors with the incident beam and the zeroth backward-diffraction order. By doing so, the predicted propagation angles from Eq. (5.4) are $\phi_0 = 28°$ and $\phi_{-1} = -27.1°$. On the other hand, the propagation directions as obtained from the angular spectra in Fig. 5.14(b) are $\phi_0 = 29° \pm 0.5°$ and $\phi_{-1} = -27° \pm 0.5°$. We notice that theoretical and numerical results are in good agreement for ϕ_{-1} with a small discrepancy for ϕ_0. In order to explain the reason for such a discrepancy one needs to analyze the behavior of the incident Gaussian beam and the refracted beams with angular spectra located in the row of primitive cells $q = 0$. In the present case C1 dominates over the other spectra in the row $q = 0$; hence, we shall consider only C1 for purposes of this explanation. The normalized magnitude of C1 and the magnitude of the incident Gaussian beam's spectrum are denoted in Fig. 5.18, respectively, as the solid curve and the circular markers. Observe that the peak of the spectrum C1 is shifted to the left; this indicates a larger reduction in the amplitudes of angular components with higher spatial frequencies along the k_y axis (those on the right tail of the spectrum). However, the electric fields of the incident beam, the zeroth backward-diffraction order, and the group of Bloch space-harmonics in the row of primitive cells $q = 0$ must be continuous across the interface. Consequently the zeroth backward-diffraction order must have larger amplitudes in angular components with higher spatial frequencies along the k_y axis. This causes a slight shift in its peak amplitude, and hence, the diffraction angle is slightly larger than the one predicted by the grating equation.

5.3 Summary

This chapter studied the refraction and reflection at an interface between a homogeneous medium and two-dimensional PhCs. The analysis was carried out in the **k**-domain from the results obtained using the FDTD-Fourier method. The analysis reveals a number of interesting phenomena and helped to clarify them. This appears to be the first time that a detailed study of beam behavior (i.e., angular profile, distortion, and propagation angle) in PhCs has been given.

It was found that the various beams that form the overall Bloch mode experience a number of distortions, some of which are caused by the shape of the Fourier-coefficient function of the Bloch modes. Distortions that are caused by boundary conditions are the same for all the beams. An example is the clipping effect mentioned in Section 5.1.2, and the projective scaling mentioned in Section 5.2.3. On the other hand, those distortions that are caused by the Fourier-coefficient function are different for the different beams because of the different values and slopes of the Fourier-coefficient function at the locations of the different beams. The effect is that the Fourier-coefficient function causes the multiple beams to behave differently.

For the cases considered here, the magnitude of the effective refractive index is much smaller than the background refractive index. As a result, the boundary condition at the various possible incidence angles are matched by beams from different EFCs located in different primitive cells. In addition, for some range of incidence angles, none of the EFCs can provided propagating wave that would match the boundary condition. Therefore a partial gap exists over this range of angles. The propagation of light through the PhC was analyzed for the different ranges of incidence angle.

It was shown that the characteristics of the refracted beam into the PhC strongly depend on the propagation angle and spectral width of the incident beam. When the plane-wave spectrum of the incident beam is wide, the resulting refracted beams' spectra broaden due to the scaling on the EFCs. Under such conditions, the Fourier-coefficient function distorts the spectral profiles of the refracted beams more severely, producing asymmetrical distributions. Moreover, when the angle of incidence approaches the edge with the partial-gap, the beam spectrum is cut off, causing a spectral clipping effect, which leads to additional distortion. At large incidence angles, anomalous refraction occurs. In this case, projective scaling may narrow (widen) the refracted beam spectra, producing wider (narrower) refracted beams. Moreover, the refracted beams often suffer from distortions caused by projective scaling, which results in asymmetrical beams. The reflection behavior was also studied. For incident plane waves that match modes inside the PhC the reflections behave as expected according to the grating equation. However, the shapes and diffraction angles of the reflected beams are modified when the spectra of the refracted beam that satisfy the baoundary conditions are distorted by the Fourier-coefficient function. Similarly, for incidence angles falling in the partial-gap, the reflections also behave according to the grating equation;

yet, the shapes and diffraction angles of the reflected beams can be severely modified depending on whether or not the planes waves can penetrate the PhC.

Chapter 6

A photonic-crystal-based beam shifter

A beam shifter is an optical device that translates the axis of a given light beam to a different position. The beam-shift effect can be obtained with slabs of birefringent material [69] or left-handed meta-materials [70]. These devices are used as beam routers in free-space optical switching networks [71]. This chapter proposes a photonic-crystal-based beam shifter, which operates based on the beam-steering properties of the periodic medium. This particular structure can be used as an optical nano-switch for monochromatic beams. The device's performance is studied by employing the FDTD-Fourier method of analysis.

6.1 Device description

A top view of the beam shifter analyzed in this chapter is shown in Fig. 6.1. It consists of a hexagonal-lattice PhC made of air holes of radius $0.4a$ etched in a dielectric material with refractive index $n_b = 3.6$. The PhC structural parameters are identical to those of the structure previously analyzed in Chapter 5. The plane of periodicity is the (x, y)-plane. The PhC's width in the x-direction is $26.6a$ and its height in the y-direction is $60a$. The PhC background dielectric, denoted by the gray areas in the figure, is

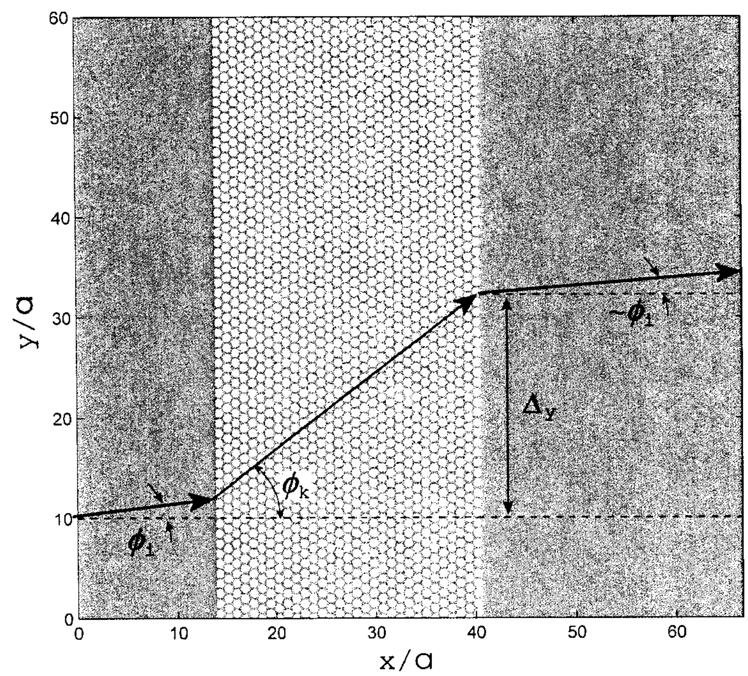

Figure 6.1: Top view of the proposed beam-shifter device embedded in a homogeneous dielectric medium with refractive index $n_b = 3.6$. The beam-shift effect is shown schematically by the arrows.

extended into the two homogeneous regions that surround the PhC. The interfaces between the PhC and the homogeneous dielectrics are in the (y, z)-plane in the $\Gamma - K$ direction of the crystal. Furthermore, we shall assume that the structure has finite thickness in the z-direction and sits in free space. The effect of the finite thickness will be explained in the following section.

The proposed device operates on TM-polarized monochromatic waves with free-space wavelength of $\lambda = a/0.425$. For telecommunication frequencies, say $\lambda = 1550$nm, this means that the PhC's lattice constant is $a = 658.75$nm. The shift effect follows from a simple, yet peculiar, refractive principle. It is shown schematically by the arrows in Fig. 6.1. An incident wave propagating from left to right in the first homogeneous medium impinges onto the input interface at an angle ϕ_i. Subsequently, the refracted wave propagates in the periodic medium with an angle ϕ_k and reaches the output interface after being displaced a distance Δ_y in the y-direction. The wave is then transmitted into the second homogeneous medium with the same angle as the incident wave. At the operation frequency, the PhC's effective refractive index is much smaller than the index of the homogeneous dielectric. As a result, the incident wave is refracted with a relatively large propagation angle enhancing the beam-shift effect. Furthermore, due to the anisotropy of the PhC's dispersion relation, the refractive phenomenon is fairly insensitive to variations in the incidence angle over certain range. It provides a fairly uniform beam displacement for waves with incidence angles in such range. This effect would not be possible with a simple homogeneous medium of smaller refractive index.

6.2 Two-dimensional analysis

In this case, we consider a three-dimensional device in which waves propagate in the (x, y)-plane and are confined in the z-direction via of total internal reflection. The different components of a Bloch mode are no longer plane waves; they are now defined by the guided modes in the slab which depend on the slab thickness and the incidence angle in the (y, z)-plane, $\phi_\perp$. The guided Bloch-mode is obtained as

$$\begin{aligned} \psi(\mathbf{r}; \mathbf{k}'_{||}, k_z) &= \psi(\mathbf{r}; \mathbf{k}'_{||}) \left[\exp(jk_z z) + \exp(-jk_z z)\right] \\ &= 2\cos(k_z z)\psi(\mathbf{r}; \mathbf{k}'_{||}), \end{aligned} \tag{6.1}$$

where $\psi(\mathbf{r}; \mathbf{k}'_{||})$ is the Bloch mode in the (x, y)-plane, and the cosine factor is the mode profile in the z-direction. The Bloch vector of a guided mode, $\mathbf{k}'_{||}$, is smaller than its counterpart in an unbounded two-dimensional PhC, $\mathbf{k}'$, and they are related per

$$\mathbf{k}'_{||} = \mathbf{k}' \cos(\phi_\perp). \tag{6.2}$$

It has been shown that the dispersion characteristics of a PhC-slab and its pure two-dimensional analogue differ merely in a frequency shift [37]. This frequency shift can be understood from the Bloch vector scaling given in Eq. (6.2). Additionally, in a PhC-slab, some Bloch-mode components may leak out. For example, in the present case,

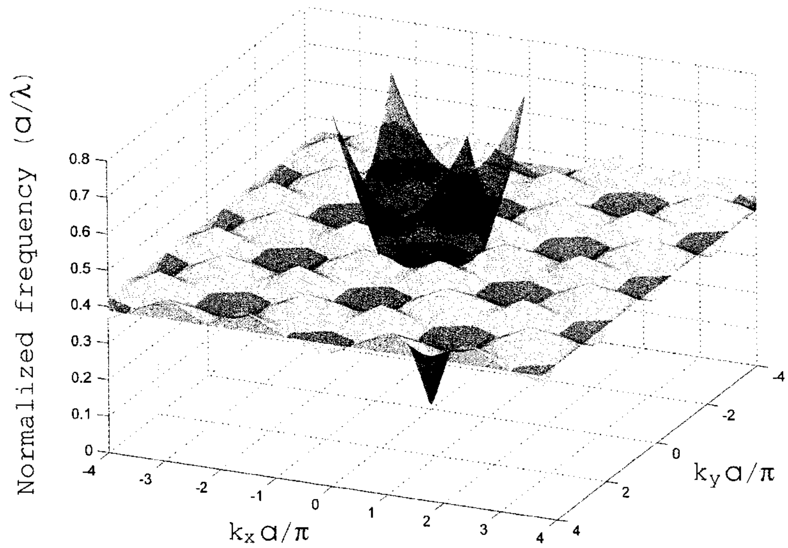

Figure 6.2: Fourth band of the PhC's dispersion relations and the light cone. The constant frequency plane represents the operation frequency.

the PhC-slab sits in free space. Hence, the guided modes must lie below the light cone [72], which represents the dispersion relation of modes in free space[1]. Fig. 6.2 shows the fourth frequency band of the PhC's dispersion relations; the light cone, located at the center of the **k**-space; and the constant-frequency plane, which denotes the operation frequency. Observe that the fundamental Bloch space-harmonic (the one in the 1BZ) is located above the light cone, and hence it leaks into free space; the rest of the Bloch space-harmonics are guided in the slab. There will always be a certain amount of loss due to the Bloch-mode plane-wave components above the light cone if the amplitudes of such plane-wave components are not identically zero. This loss is often referred to as *out-of-plane radiation loss* [73].

The analysis of effects due to the finite thickness in the z-direction is considered out of the scope of this thesis. Therefore, for the present analysis, we shall consider a paraxial approximation for which $\cos(\phi_\perp) \approx 1$ in Eq.(6.2). In such a case, $\mathbf{k}'_{||} \approx \mathbf{k}'$, and hence, the Bloch-vector scaling can be neglected. Furthermore, the out-of-plane radiation shall be considered only qualitatively. Thus, we will proceed with the analysis of the beam shifter assuming that it is a pure two-dimensional structure.

[1] The light cone is formed by **k**-shells of increasing radius for increasing frequencies.

6.3 Principle of operation

In order to describe the principle of operation, we consider the EFC at the operation frequency, which describes modes in the fourth frequency band. The EFC is shown in the repeated zone scheme in Fig. 6.3(a) together with the **k**-shell associated with the light cone (small circle) and the **k**-shell of the homogeneous dielectric medium (large circle). The wave vector $\mathbf{k}^{(i)}$ represents a wave with propagation angle ϕ_i incident from the homogeneous dielectric into the PhC. It satisfies the $\mathbf{k}_{||}$-conservation condition on EFCs in the row of primitive cells $q = 0$, exciting a Bloch mode with group velocity vector $\mathbf{v}_g$, as shown in Fig. 6.3(b). In this case, the refraction angle is relatively larger than the incidence angle because the EFC size is much smaller than the **k**-shell size. Moreover, the flat contours of the EFC provide a collimation effect for a specific range of incidence angles, which results in a fairly insensitive refraction angle to incidence angles in such range.

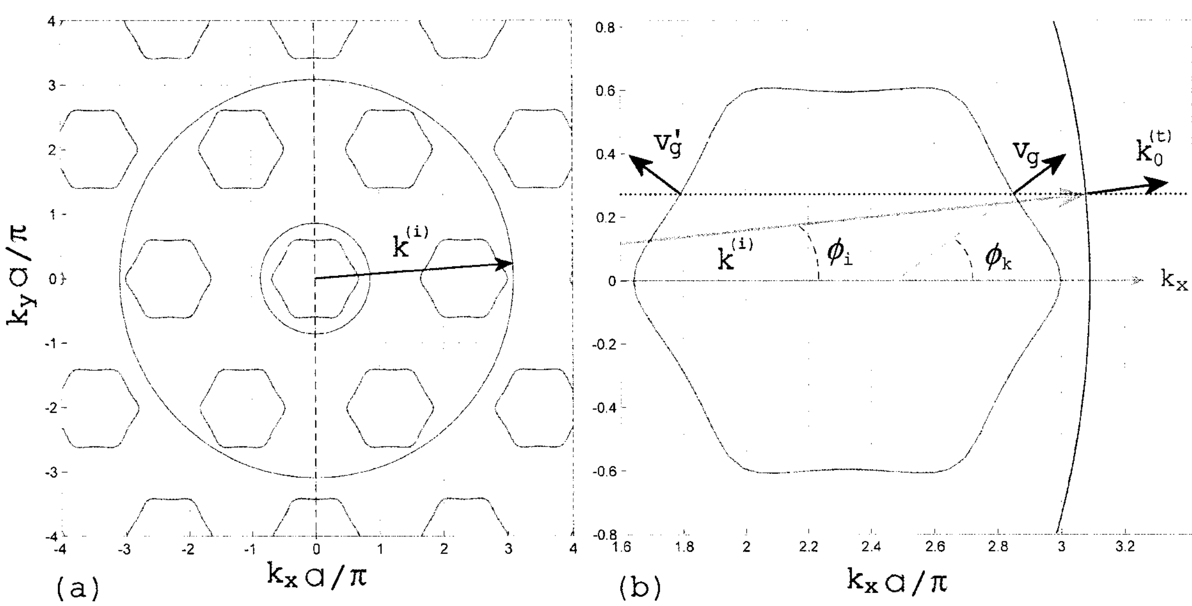

Figure 6.3: (a) The EFC in the repeated zone scheme at the operation frequency for the PhC under consideration. The small and large circles denote, respectively, the free-space **k**-shell and the homogeneous dielectric **k**-shell; the vertical dashed line indicate the orientation of the interface; and $\mathbf{k}^{(i)}$ is a wave incident into the PhC from the first homogeneous dielectric. (b) Description of the group velocity vectors for the forward-propagating Bloch mode ($\mathbf{v}_g$) and the Bloch mode reflected at the output interface ($\mathbf{v}'_g$).

The refracted wave propagates inside the PhC and reaches the output interface after being shifted in the y-direction by $\Delta_y = w \tan(\phi_k)$, where w is the width of the PhC. At that point, a reflected mode with group velocity vector $\mathbf{v}'_g$ is generated inside the PhC. On the other hand, the field transmitted into the second homogeneous dielectric consists of a number of diffraction orders with the tangential wave vector of the q-th diffraction order being $\mathbf{k}^{(t)}_{q,||} = \mathbf{G}_{q,||} + \mathbf{k}^{(i)}_{||}$. The zeroth diffraction order, denoted by $\mathbf{k}^{(t)}_0$ in the figure, propagates in the same direction as the incident wave, representing its shifted version.

Since the EFC has mirror symmetry about the k_x axis, the same mechanism follows for negative incidence angles. Hence, by providing an incident wave with propagation angle of $-\phi_i$ one obtains a negative shift in the y-direction. The device can therefore be used to construct an optical selector-switch triggered by a fairly small change in the incidence angle (around $\pm 5°$).

6.4 Device specifications

The device performance is (in part) limited by the size and location of the EFCs, implying that the incident beam's angular spectrum is restricted to a range of propagation angles. For example, from Fig. 6.3(b) we note that the incident beam must restrict its tangential wave-vector components to match points on the EFC, otherwise they fall in a partial gap and are reflected. The EFC is extended over the range $-0.6\pi/a < k_y < 0.6\pi/a$. However, since it has mirror symmetry about the k_x axis, we shall consider only positive k_y values. Furthermore, the device must steer the incident beam's plane-wave components rather uniformly over a wide enough range of wave vectors in the adequate direction to achieve the beam-shift effect. Hence, we must further restrict their tangential components to fall within a range where the EFC is to some extent straight.

6.4.1 Angular operation range

To specify the operation parameters for this device one must face a trade-off between variation of ϕ_k and permitted range for the incidence angle, ϕ_i. For example, consider Fig. 6.4, which shows the refracted beam propagation angle, ϕ_k, obtained as the gradient of the EFC. Notice that ϕ_k presents small variations about $k_y = 0.3\pi/a$ and these variations increase as the angular range becomes broader. Hence, if the variation of ϕ_k is intended to be very small, then one must restrict the angular spectrum of the incident beam to a very narrow range of angular components. For the present design, the maximum variation of ϕ_k has been restricted to $\pm 5°$. This is with the purpose of presenting clearly the **k**-space analysis using wide angular spectra. For such a specification, the allowed tangential wave-vector range is $0.06\pi/a < k_y < 5.4\pi/a$, which is denoted by the shaded region in Fig. 6.4. We shall refer to this range as the *angular operation range.* The values of ϕ_k vary from 25° to 35° over the entire range of operation. This indicates that angular components within this range are steered more or less uniformly with a propagation angle of approximately 30°. Moreover, note that the EFC has a slight concave curvature, which provides a slight focusing effect for angular components on the concave section. This is represented in the inset by the group velocity vectors indicated by the arrows.

By providing an incident beam such that its plane-wave components have tangential wave vectors within the angular operation range, the proposed device shifts the beam's plane-wave components by a distance

$$\Delta_y = 26.6a \tan(30 \pm 5°). \tag{6.3}$$

6.4.2 Input source

It is important to consider the fact that incident waves with tangential wave-vector components out of the angular operation range may lead to power loss and beam distortion. In the first place, this is because those tangential wave vectors beyond the

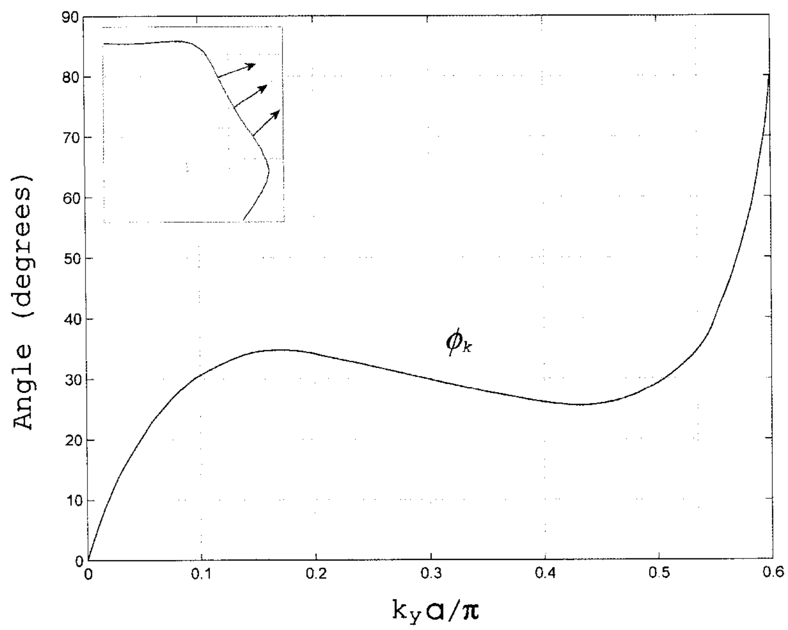

Figure 6.4: Bloch-mode propagation angle, ϕ_k, as a function of the tangential wave vector component, k_y. The shaded region denotes the angular operation range.

range covered by the EFC are unable to match propagating Bloch modes; therefore, the waves are completely reflected. In the second place, the refraction angle, ϕ_k, increases (decreases) rapidly as the tangential wave vector goes beyond the upper (lower) limit of the angular operation range (see Fig. 6.4). Those excited Bloch modes with large propagation angles reach the output interface with different shifts, Δ_y, causing distortion that generates losses when the output beam couples to a subsequent device. Hence, we shall specify parameters for the input beam such that most of the beam's energy is contained in plane-wave components within the angular operation range.

We shall consider a Gaussian beam to model the input source. For this example, the specification requires the Gaussian spectrum, projected onto the k_y axis, to be centered in the angular operation range. In addition, the spectrum's width must allow the angular components that form the beam radius to fall in such a range. We must also consider a tolerance for possible variations in the incidence angle. Taking into account a tolerance of $\pm 1°$, the incident Gaussian beam must have a waist and an incidence angle according to the following expression:

$$w_0 > 3.3a \ \text{ for } \ \phi_i = 5.6° \pm 1°. \tag{6.4}$$

Following this specification, at least 86% of the optical power is contained in plane-wave components within the angular operation range.

6.4.3 Frequency/lattice-constant deviation

In practical situations the incident beam may have deviations from the operation frequency, or equivalently, the lattice constant may have certain deviation due to fabrication issues. To determine the effect of such deviations on the device's performance, one must consider the shape of the EFC at frequencies neighboring the operation frequency. Fig. 6.5 shows the EFC for different frequencies, which are labeled accordingly on each contour. The bold EFC denotes the operation frequency.

As the frequency decreases the EFC size decreases and the collimation effect is gradually lost because the shape becomes rounded. As a result, a refracted beam would experience a large divergence. On the other hand, for larger frequencies, the EFC becomes larger and their segments develop with concave curvature. At those frequencies for which EFCs have pronounced concave curvature the refracted beam would experience a focusing effect with large divergence after the focal point. Large divergence effects are undesirable for this application because they lead to large modifications of the beam profile in the real space. Therefore, we must restrict the acceptable frequency (or lattice constant) deviation to those values describing EFCs with rather straight shapes.

An adequate frequency range that conserves the PhC's collimation properties is $0.42 < a/\lambda < 0.43$. This is, for example, 1532nm $< \lambda <$1568nm or 651nm$< a <$667nm if the operation frequency is λ = 1550nm. However, to conserve the variation of ϕ_k within the specification of $\pm 5°$, the angular operation range must be reduced to $0.2\pi/a < k_y < 0.4\pi/a$. This range is denoted by the shaded region in Fig. 6.5.

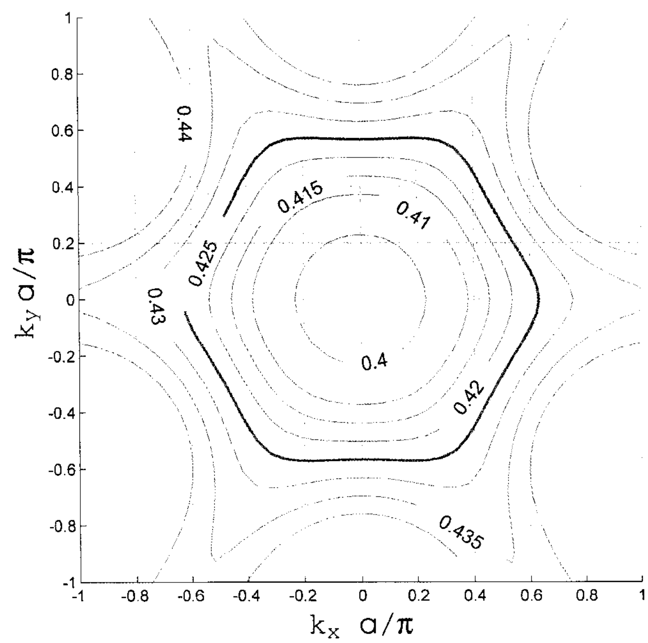

Figure 6.5: The EFC at different frequencies around the operation frequency. The EFC at the operation frequency is shown in bold.

For purposes of the following analysis, we shall employ an ideal monochromatic source applying the specifications defined in the two previous subsections, i.e., the angular operation range as denoted by the shaded region in Fig. 6.4 and the Gaussian beam parameters as given in expression 6.4. In practical situations, however, it is convenient considering the effect of a deviation in the operation frequency by using the reduced specification for the angular operation range.

6.5 Performance

To study the device's performance, we use a Gaussian beam with waist $w_0 = 3.3a$ incident at an angle $\phi_i = 4.6°$. These conditions are for the extreme case where the angular components that form the beam's radius fall just above the lower limit of the angular operation range. The peak of the Gaussian beam's angular spectrum projected onto the k_y axis is located at $k_y = 0.25\pi/a$, and its magnitude reduces to 36% of the peak value at the lower limit of the operation range.

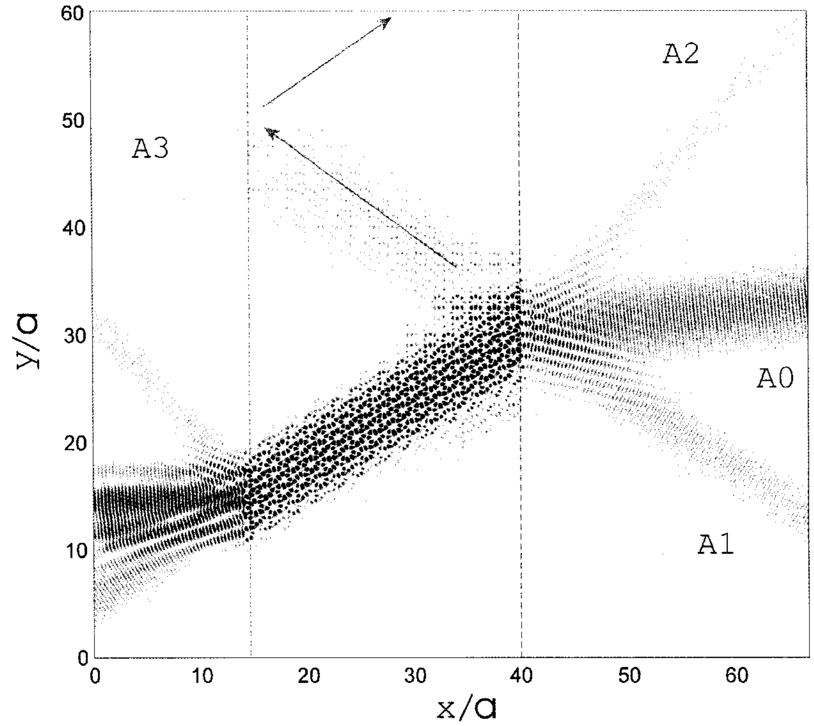

Figure 6.6: Electric field distribution after $0.057\mu s$ of a Gaussian beam incident onto the beam-shifter's interface. The beam propagates with an angle of 4.6°. The vertical dashed lines denote the interfaces of the beam shifter. The shifted version of the incident beam is labeled A0.

The electric field distribution after $0.057\mu s$ is shown in Fig. 6.6. The incident Gaussian beam impinges onto the PhC interface and is refracted with an angle $\phi_k \approx 30°$. At the same time, three backward-diffraction orders are generated at the input interface. The refracted wave reaches the output interface, then part of the energy is transmitted into the second homogeneous medium and the rest is reflected inside the PhC. The reflected Bloch wave eventually reaches the input interface and couples into the first homogeneous medium, generating the weak field labeled A3. Subsequently, another forward-propagating Bloch wave, with very weak amplitude, is generated at the input interface. Such a wave is then absorbed by the upper FDTD boundary. On the other hand, the field transmitted into the second homogeneous medium consists of three diffraction orders, labeled A0, A1, and A2. The zeroth diffraction order, A0, represents the shifted version of the incident beam. The shift distance at the output is $\Delta_y \approx 17a$. This value is in good agreement with the value $\Delta_y = 16.6a$ predicted by

Eq. (6.3) when $\phi_k = 32°$, which corresponds to the refraction angle for $\phi_i = 4.6°$ (see Fig. 6.4).

The magnitudes of the refracted and transmitted fields' angular spectra are shown in Fig. 6.7(a). The magnitudes are normalized to the overall peak value, which corresponds to the peak of the spectrum labeled B1. The angular spectra of the incident and reflected beams that exist in the first homogeneous dielectric have been omitted for clarity. The magnitude of the Fourier-coefficient function, $U^{(4)}(\mathbf{k})$, is shown in Fig. 6.7(b). The EFC in the repeated zone scheme and the free-space **k**-shell at the operation frequency are superimposed in both figures. Furthermore, the **k**-shell for the homogeneous dielectric at the operation frequency is denoted by the large circle in Fig. 6.7(a). We shall study the characteristics of the refracted and transmitted beams in the **k**-space in order to evaluate the performance of the device.

6.5.1 Refracted beams

At the operation frequency, Bloch waves propagate with positive group velocity. Therefore, the angular spectra of forward-propagating beams are represented by the spectra on the right-hand side of the EFCs, whereas the spectra on the left-hand side correspond to the Bloch modes reflected at the output interface. Leaky Bloch-mode components are represented by the angular spectra that lie above the light cone, or equivalently, inside the free space **k**-shell. Their amplitudes are severely suppressed by the Fourier-coefficient function, and therefore, they do not represent a significant part of the guided mode. The weak angular spectra streaking off the EFCs from the propagating-beam spectra are spurious evanescent modes[2] created by removing the incident and reflected fields prior to the **k**-space transformation.

The angular spectra presents five dominant beams, which are labeled B0 to B4 in Fig. 6.7(a). Their magnitudes are shown in Fig. 6.7(c) projected onto the k_y axis. The vertical lines in this figure indicate the spatial frequency at the peak-location of the incident Gaussian spectrum and the shaded regions denote the angular operation range.

[2]Refer to Section 4.2.3 for details.

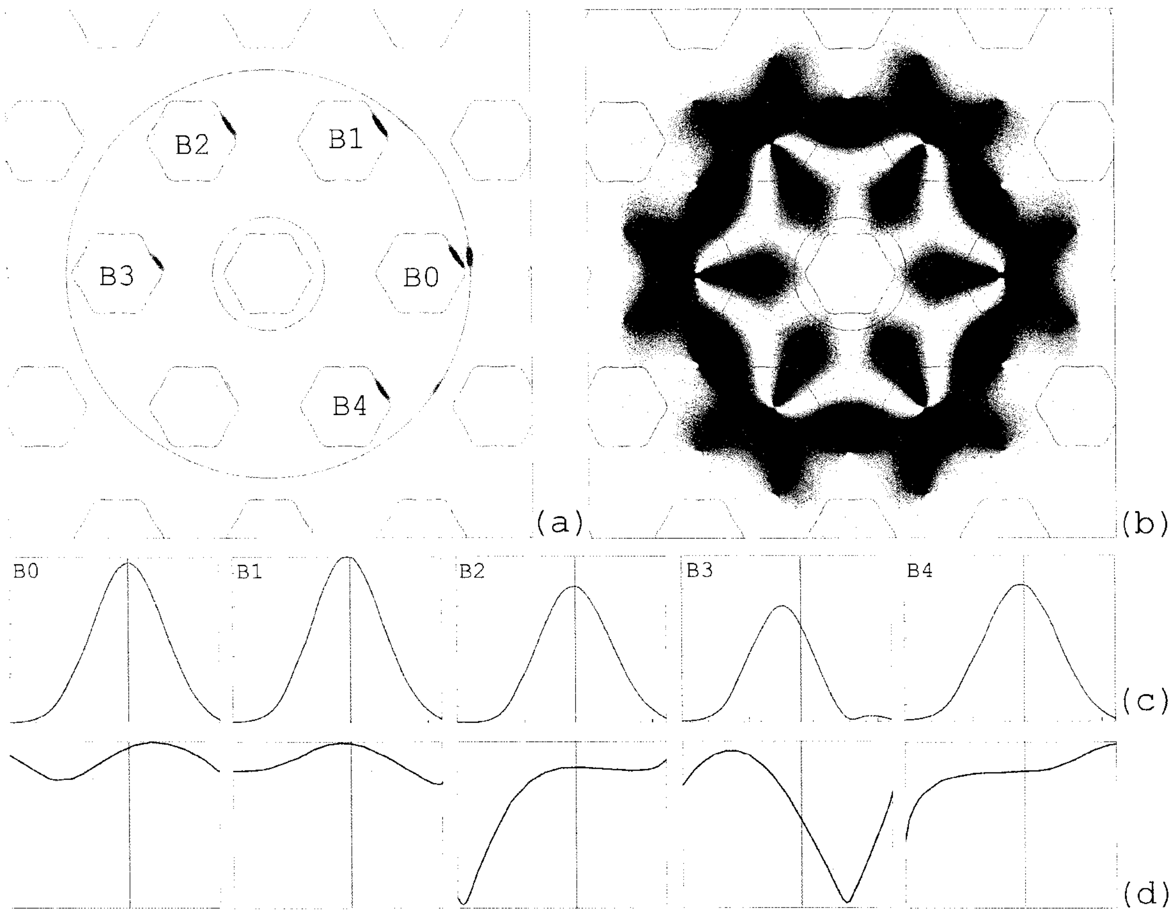

Figure 6.7: (a) Magnitude of the angular spectra of the refracted and transmitted fields in Fig. 6.6. (b) Magnitude of the Fourier-coefficient function for the fourth frequency band. (c) Magnitudes of dominant beam spectra projected onto the k_y axis. (d) Normalized magnitudes of the Fourier coefficients that modulate the dominant beam spectra projected onto the k_y axis. Each curve in (d) is associated with the beam spectrum above it.

The normalized magnitudes of the Fourier-coefficient function at the locations of the dominant beam spectra are shown in Fig. 6.7(d). Here, each curve is associated with the beam spectra above it and the shaded region denotes the angular operation range. Note that the Fourier-coefficient function has small gradual variations at the locations of B0, B1, B2, and B4 over the angular operation range. Hence, the amplitude profiles of these spectra are not significantly distorted regardless of their wide distribution. On the other hand, the slope of the Fourier-coefficient function at the location of B3 presents considerable variations that noticeably shift the peak of B3 toward a lower spatial frequency. Moreover, all the dominant beam spectra extend amplitudes below the lower limit of the angular operation range. These amplitudes are more or less the same for the different spectra, representing plane-wave components with amplitudes of around 36% of the overall peak amplitude. These plane-wave components propagate with smaller angles, ranging between 0° to 25° (see Fig. 6.4), and are visible in the real domain as the weak field distribution that appears below the collimated beam in Fig. 6.6.

6.5.2 Transmitted beams

The energy transmitted into the second homogeneous medium is concentrated in three diffraction orders. In Fig. 6.7(a) one can identify the +1, −1, and zeroth diffraction-orders as the spectra located on the right-hand side of the homogeneous dielectric **k**-shell at the same level as the rows $q = +1$, $q = -1$, and $q = 0$, respectively. These three beam spectra are respectively associated with the beams A2, A1, and A0 in the real space field distribution, shown in Fig. 6.6.

Note in the real-space field distribution that the zeroth diffraction order contains the majority of the energy, followed by the −1 and +1 diffraction orders. To explain the physical phenomenon that determines the distribution of the transmitted energy in the different forward-diffraction orders we explore the mechanism of light transmission at the output interface. It follows from the $\mathbf{k}_{||}$-conservation condition and the continuity of the tangential electric field across any interface that the phase matched electric fields at the output interface are given in terms of their angular spectra per

$$A_q(\mathbf{k}_{t,q}) = \alpha_q^{(f)}(\mathbf{k}_f)U_q^{(4)}(\mathbf{k}_f) - \alpha_q^{(b)}(\mathbf{k}_b)U_q^{(4)}(\mathbf{k}_b), \qquad \mathbf{k}_{t,q,||} = \mathbf{k}_{f,||} = \mathbf{k}_{b,||}, \tag{6.5}$$

where $\mathbf{k}_f$ and $\mathbf{k}_b$ are, respectively, the Bloch vectors of the forward- and backward-propagating modes; $A_q(\cdot)$ is the electric-field angular spectrum of the q-th diffraction order with $\mathbf{k}_{t,q}$ denoting its wave vectors; $\alpha_q^{(f)}(\cdot)$ and $\alpha_p^{(b)}(\cdot)$ are the respective Bloch-coefficient functions of the forward- and backward-propagating Bloch modes replicated over the primitive cells in the q-th row, this is, $\alpha_q(\mathbf{k}) = \sum_{\mathbf{G}_{||,q}} \alpha(\mathbf{k} - \mathbf{G}_{||,q})$; and

$U_q^{(4)}(\mathbf{k}) = \sum_{\mathbf{G}_{||,q}} U_{\mathbf{G}}(\mathbf{k} - \mathbf{G}_{||,q})$ is the Fourier-coefficient function over the q-th row of primitive cells.

We note from Eq. (6.5) that the amplitude of the q-th diffraction order is given by the amplitudes of both forward- and backward-propagating Bloch space-harmonics in the q-th row of primitive cells. Therefore, the amplitude of such a diffraction order varies depending on whether the Fourier-coefficient function, $U_q^{(4)}(\mathbf{k})$, has small or large amplitudes for the different Bloch vectors of the reflected mode. If the amplitudes of $U_q^{(4)}(\mathbf{k})$ suppress the reflected Bloch space-harmonics, then the q-th diffraction order is more intense. Conversely, if $U_q^{(4)}(\mathbf{k})$ allows reflected Bloch space-harmonics with large amplitudes, then the q-th diffraction order is weaker. For example, from Fig. 6.7(a) and 6.7(b) one can deduce that the amplitude of the -1 diffraction order is larger than the amplitude of the $+1$ diffraction order because the Fourier-coefficient function reduces the amplitudes of reflected beams in the row of primitive cells $q = -1$ in larger extent than for the reflected beams in the row $q = +1$.

6.5.3 Shifted-beam distortion

The shifted-beam is distorted due to the reflections at the input and output interfaces. To analyze such a distortion we shall consider its angular spectrum. At this point we must remark that in order to give a correct interpretation to the beam distortion in terms of the angular spectrum, it is important to consider that the angular spectrum represents the amplitudes of the plane-wave components regardless of their spatial distribution in the real space. For example, consider the electric field distribution in the real space, shown in Fig. 6.6. The field below the collimated bulk reaches the output interface and couples to the second homogeneous medium generating three diffracted waves with weak amplitudes. These waves are spatially separated from the diffraction orders from which the shifted-beam is obtained. Such a distortion cannot be detected in the angular spectra. In the present case, these waves have negligible amplitudes. Hence, the angular spectrum gives a good estimation of the beam distortion. Otherwise, one should also consider the distortion analysis in the real space.

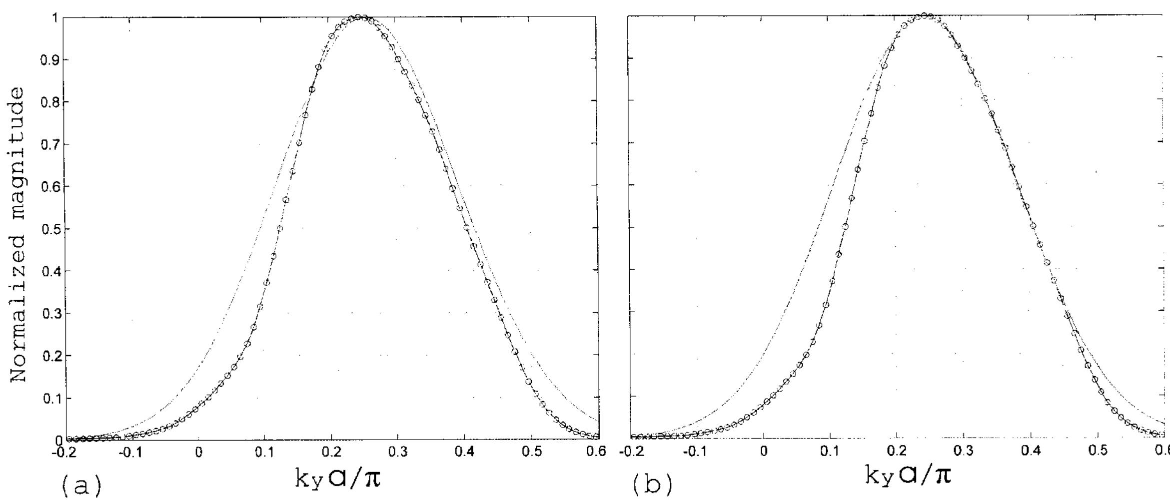

Figure 6.8: (a) Magnitude of the incident beam's angular spectrum (solid line) and normalized magnitude of the shifted beam's angular spectrum (circular markes), both projected onto the k_y axis. (b) Magnitude of the incident beam's angular spectrum displaced by $\Delta'_y = -0.3k_y$ (solid line) and normalized magnitude of the shifted beam's angular spectrum (circular markes), both projected onto the k_y axis.

We now proceed with the analysis of distortion. To illustrate the degree of distortion introduced by the PhC, we consider Fig. 6.8(a). The solid line denotes the magnitude of the incident beam's angular spectrum and the circular markers describe the normalized magnitude of the angular spectrum associated with the shifted beam at the output, both projected onto the k_y axis. The angular operation range covers the shaded region. The peak amplitude of the shifted-beam's spectrum is displaced by approximately $\Delta'_y = -0.03k_y$. This implies that the shifted-beam's propagation direction differ from the incident beam's by $\Delta\phi \approx 0.6°$. Furthermore, we observe a considerable distortion in plane-wave components with tangential wave vectors over the range $-0.1\pi/a < k_y < 0.15\pi/a$ and a slight distortion over the range $0.45\pi/a < k_y < 0.6\pi/a$. From Eq. (6.5) one concludes that such distortions are the result of two factors: In the first place, the shifted-beam's angular spectrum is shaped in accordance to the spectra of forward-propagating Bloch space-harmonics in the row of primitive cells $q = 0$, namely, the factor $\alpha_0^{(f)}(\mathbf{k}_f)U_0^{(4)}(\mathbf{k}_f)$ in Eq.(6.5). Hence, the distortion is in part due to the boundary conditions that define the (forward) Bloch-coefficient function and by Fourier coefficients that modulate such function in the row of primitive cells $q = 0$. In the second place, additional distortion results from reflections of Bloch space-harmonics in this same row of primitive cells. These reflections are not uniform but their amplitudes are defined by the spectra of backward-propagating Bloch space-harmonics in the row of primitive cells $q = 0$, namely, $\alpha_0^{(b)}(\mathbf{k}_b)U_0^{(4)}(\mathbf{k}_b)$. Thus, the distortion also depends on the boundary conditions at the output interface that define the (backward) Bloch-coefficient function and on the Fourier-coefficients that modulate such function in the row of primitive cells $q = 0$. Hence, apart from the boundary conditions at both interfaces, we note that the Fourier-coefficient function plays an important role in determining the distortion of the transmitted beam.

The solid curve in Fig. 6.8(b) denotes the incident Gaussian spectrum displaced by $\Delta'_y = -0.3k_y$ to fit the curve of the shifted beam at the output. Observe that within the range $0.17\pi/a < k_y < 0.47\pi/a$ (shaded region), there is practically no distortion other than the shift Δ'_y. The maximum distortion represents 7% of the normalized amplitude and corresponds to the lower limit of this range. To reduce the distortion one must specify the waist and propagation angle of the incident beam such that its spectrum locates the angular components with larger amplitudes in the low-distortion angular operation range. Hence, the specification for the incident Gaussian beam in order to achieve low distortion, taking into account a maximum deviation of $\pm 1°$ in the incidence angle, is given by

$$w_0 > 6.4a \quad \text{for} \quad \phi_i = 5.8° \pm 1°. \tag{6.6}$$

6.5.4 Power efficiency

The power fluxes carried by different diffraction orders are computed following the procedure explained in Section 4.4. The results, shown in Fig. 6.9, are normalized to the incident power flux, P_i. The figure shows the power flux at several points along the x axis. The three regions bounded by the vertical dashed lines are associated with the three different media. From left to right, the first and third regions correspond to the homogeneous dielectric media, while the second region corresponds to the PhC.

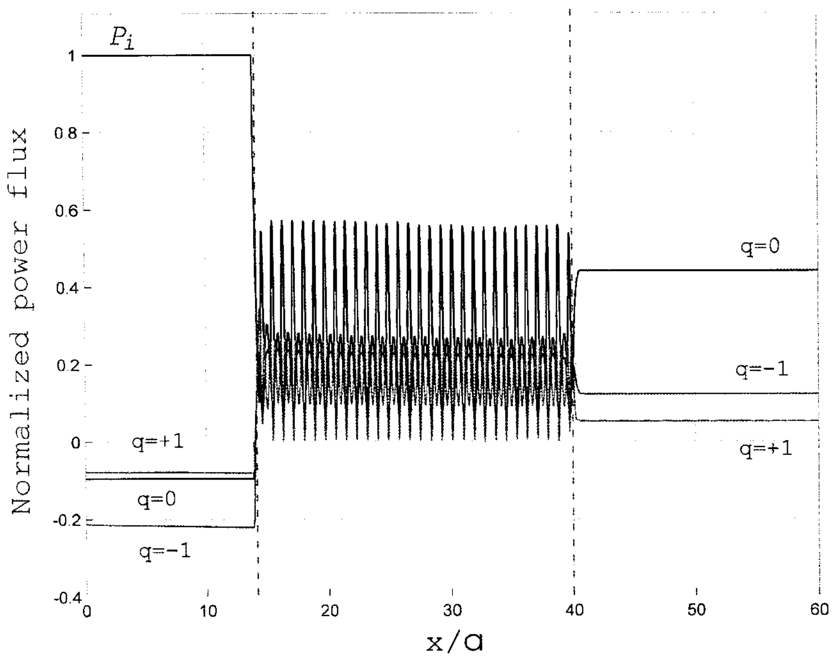

Figure 6.9: Normalized power flux of the three lowest diffraction orders as a function of x. The dashed lines bound the region where the PhC is located.

The power flux of the backward- and forward-diffraction orders, generated at the input and output interfaces, are denoted, respectively, by the values in the first and third regions. The zeroth, -1, and $+1$ (backward and forward) diffraction orders are labeled accordingly. On the other hand, the values in the second region are associated with the group of Bloch space-harmonics that generate both forward- and backward-diffraction orders. Particularly, the results for the second region may be helpful in obtaining an understanding of the energy-interchange process among the different Bloch space-harmonics. However, the analysis of power fluxes inside the PhC is beyond the scope of this thesis, and thus, we shall limit the analysis to obtain the device's power efficiency.

At the input interface, the power coupled into the PhC is estimated as $0.61P_i$; however, at the output interface the total transmitted power is $\mathcal{T} = 0.60P_i$. The reason for the difference is that part of the energy carried by the reflections is absorbed by the upper FDTD boundary (see Fig. 6.6). This implies that approximately $0.01Pi$ is reflected forward at the input interface and absorbed by the FDTD boundary. The power flux carried by the different diffraction orders generated at the output interface are $\mathcal{T}_0 = 0.44P_i$, $\mathcal{T}_{-1} = 0.11P_i$, and $\mathcal{T}_{+1} = 0.05P_i$, where $\mathcal{T}_q$ corresponds to the q-th diffraction order. The device's power efficiency, given as the ratio of the incident power to the power flux transmitted in the zeroth diffraction order, is approximately 44%.

From the previous power analysis, we note that the device's transmission efficiency is poor. One can detect two types of loss; one type is associated with the zeroth-order diffraction efficiency and the other type corresponds to the insertion loss. The former is 16% of the optical power whereas the latter is approximately 40%. The main part of the insertion loss is attributed to reflections at the input interface; the loss due to reflections at the output interface is estimated to be $0.02P_i$. This value was calculated by isolating the reflected electric field labeled A3 in Fig. 6.6 and the associated magnetic fields, in order to compute the power flux carried by them. It is therefore possible to reduce considerably the insertion loss by applying reflection suppression techniques to the input interface. For example, one can design a mode-matching interface as proposed by Witzens [74]. It consists of a stack of diffraction gratings designed to match the modes in both homogeneous and periodic media. Alternatively, the power efficiency may be improved by designing an interface for high transmission as suggested by Baba [75]. This technique consists of varying the shape or size of the air-holes at both input and output interfaces in order to improve the transmission.

6.6 Summary

In order to demonstrate the usefulness of the analysis technique developed in this thesis a PhC-based device has been proposed in this chapter and its operation as a possible beam-shifter examined. The purpose of a beam-shifter is to shift the incident beam's axis to a different position. The device is three-dimensional with finite dimensions and sits in free space.

In the proposed device, light propagates in the (x, y)-plane and is confined in the z-direction by means of total internal reflection. It was shown that the two-dimensional analysis is still relevant for such a device by taking into account factors such as out-of-plane radiation and conditions for vertical confinement. These two factors may affect the behavior of the guided mode. For example, the out-of-plane radiation, which is due to the Bloch space-harmonics with spatial frequencies above the light cone, represents a loss in the guided mode. On the other hand, the conditions of vertical confinement, which depend on the incidence angle in the (y, z)-plane, produce a scaling effect on the in-plane Bloch vector. For purposes of this thesis, we approached the analysis of the device making a paraxial approximation such that the effects of the vertical confinement (i.e., the in-plane Bloch-vector scaling) can be neglected. Furthermore, it was shown that for the proposed design only the Bloch space-harmonics in the 1BZ can radiate into free space and that their magnitudes are severely suppressed by the Fourier-coefficient function in the fourth frequency band. As a result, the out-of-plane radiation does not represent a significant part of the guided mode.

Specifications for the device were stated taking as reference the operation frequency $\lambda = a/0.425$. At this frequency, the device collimates the refracted beam providing fairly uniform shifts for plane waves with tangential wave-vector components within the angular operation range $0.06\pi/a < k_y < 0.54\pi/a$. Specifications for the input source, which is modeled as a Gaussian beam, are given such that the plane-wave components that form the beam's radius fall within the angular operation range. The effect of deviations from the operation frequency or lattice constant was also addressed. The selection of an adequate operation frequency (or lattice constant) range was discussed. The performance analysis was carried out for a monochromatic Gaussian beam of frequency $\lambda = a/0.425$ considering the worst case allowed by the specifications for such a beam.

The mechanism of light transmission at the output interface was investigated. The analysis provides an explanation of the physical grounds behind the distribution of the transmitted energy in the different diffraction orders generated at the output interface; it also states the importance of the Fourier-coefficient function in such a phenomenon. The distortion of the shifted beam at the output was quantitatively characterized in terms of its angular spectrum. It was shown that the beam distortion strongly depends on the angular profile of the forward- and backward-propagating Bloch modes and on the Fourier-coefficient function. This distortion is not desirable because it leads to insertion losses when coupling the output beam into subsequent devices, such as waveguides or an optical fiber. In order to minimize the beam distortion, a low-distortion specification for the incident Gaussian beam was deduced from the distortion analysis.

A power analysis was carried out using the methodology provided in Section 4.4. The effective power loss is estimated to be 56%. The insertion loss represents approximately 40% and the remaining loss factor (16%) is related to the diffraction efficiencies of the different beams diffracted at the output interface. The high insertion loss is due to the poor coupling efficiency between the incident Gaussian mode and the refracted Bloch mode. Methods for improving the power efficiency are suggested. They consist of reducing the insertion loss by using mode-matching or high transmission-efficiency interfaces, which are detailed in Refs. [74] and [75], respectively. The analysis of power fluxes was limited to the homogeneous media surrounding the PhC. The author believes that the energy-interchange phenomenon among the different Bloch space-harmonics deserves a more detailed study.

Chapter 7

Conclusions

In integrated optical systems, one may often find interfaces between homogeneous dielectric regions and PhCs. When light propagates across such interfaces, interesting reflection and refraction phenomena are observed; they play an important role in the operation of such systems. The study presented in this thesis is intended to contribute to an analytical understanding of reflection and refraction phenomena of arbitrary monochromatic fields at interfaces between homogeneous and periodic media, based on the analysis of their angular spectra (or **k**-space representation).

The use of **k**-space analysis is an effective technique for understanding the reflection and refraction phenomena; yet, it is often limited to providing qualitative estimations of the field's intensity and angular spectrum. In this thesis, a novel method of analysis is proposed for the quantitative evaluation of angular-spectrum distortions experienced by monochromatic fields when interacting with a PhC. The method is applicable to more general PhC field situations than similar approaches described by other authors. The most important capability offered by this technique is the ability to separate the field distribution into physically interpretable beams. It also allows one to carry out power analyses, which provide quantitative estimations of the reflectance, transmittance, and diffraction efficiencies at the interface between PhCs and homogeneous media. The method consists of obtaining the field's angular spectra from an FDTD simulation. The resulting spectra allow one to regard the fields inside a PhC as a collection of beams with different propagation directions and amplitude profiles. Then, by employing useful Fourier techniques, one can analyze each beam independently in real- and **k**-space. The analysis in the **k**-space is based on a mathematical expression for the angular spectra of arbitrary monochromatic fields in PhCs, derived in Chapter 3. It states that such fields can be represented as the product of a Bloch-coefficient function (which gives the expansion of the field in terms of Bloch modes) and the Fourier-coefficient function (which gives the expansion of the Bloch-modes in terms of plane waves). The former is determined by the angular spectrum of the incident field and the boundary conditions; the latter is characteristic of the PhC and can be obtained numerically using the PWE method.

This thesis approaches the analysis of reflection and refraction by considering semi-infinite PhCs with hexagonal- and square-lattice geometries, operated under negative refraction and super collimation conditions, respectively. Both PhCs present partial band gaps for particular ranges of incidence angle, which means that waves incident at such angles are completely reflected. This appears to be the first time that a detailed study of beam behavior (i.e., angular profile, distortion, and propagation angle) in PhCs has been given. The results of the analysis show that the characteristics of the beam refracted into the PhC strongly depend on the propagation angle and spectral width of the incident beam. When the plane-wave spectrum of the incident beam is wide, the resulting refracted beams' spectra broaden due to the scaling on the EFCs. Under such conditions, the Fourier-coefficient function distorts the spectral profiles of the refracted beams more severely, producing asymmetrical distributions. Moreover, when the angle of incidence approaches the edge with the partial-gap, the beam spectrum is cut off, causing a spectral clipping effect, which leads to additional distortion. At large incidence angles, anomalous refraction occurs. In this case, projective scaling may narrow (widen) the refracted beam spectra, producing wider (narrower) refracted beams. The reflection behavior is also studied. For incident plane waves that match modes inside the PhC, the reflections behave as expected according to the grating equation. However, the shapes and diffraction angles of the reflected beams are modified when the spectra of the refracted beam that satisfy the boundary conditions are distorted by the Fourier-coefficient function. Similarly, for incidence angles falling in the partial-gap, the reflections also behave according to the grating equation; yet, the shapes and diffraction angles of the reflected beams can be severely modified depending on whether or not the planes waves can penetrate the PhC.

Finally, in order to demonstrate the usefulness of the analysis technique developed in this thesis a PhC-based real device is proposed and its operation as a possible beam-shifter examined. The three-dimensional device has finite dimensions and sits in free space. Light propagates in the (x, y)-plane and is confined in the z-direction by means of total internal reflection. It is shown that the proposed two-dimensional analysis is still relevant for such a device by considering factors such as out-of-plane radiation and conditions for vertical confinement. Furthermore, the impact of a frequency or lattice-constant deviation is discussed. The effects of the finite thickness in the z-direction and frequency/lattice-constant inaccuracies are beyond the scope of this thesis. Hence, the PhC is regarded as perfectly periodic structure and a paraxial approximation is made on the perfectly monochromatic incident beam to approach the analysis. The mechanism of light transmission at the output interface is investigated. The analysis provides an explanation of the physical reasons for the distribution of the transmitted energy in the different diffraction orders generated at the output interface; it also shows the importance of the Fourier-coefficient function in such a phenomenon. Moreover, the distortion of the shifted beam at the output is quantitatively characterized in terms of its angular spectrum. It is shown that the beam distortion strongly depends on the angular profile of the forward- and backward-propagating Bloch modes and on the Fourier-coefficient function. Such a distortion is not desirable because it leads to insertion losses when the output beam is coupled into subsequent devices, such as waveguides. In order to minimize the beam distortion a low-distortion specification for the incident Gaussian beam is deduced from the distortion analysis. Furthermore, a power analysis is carried out using the methodology provided in Section 4.4. It reveals a large power loss of 56%, of which 40% corresponds to insertion loss and 16%

is associated with the diffraction efficiencies of the diffraction orders generated at the output interface. Methods for improving the power efficiency are suggested. They consist of reducing the insertion loss by using mode-matching or high transmission-efficiency interfaces, which are detailed in Refs. [74] and [75]. The analysis of power fluxes was limited to the homogeneous media surrounding the PhC. The author believes that the energy-interchange phenomenon among the different Bloch space-harmonics deserves a more detailed study.

Some of the distortion phenomena discussed in this thesis may adversely affect the performance of any PhC device. These effects have a considerable impact when the incident beam has a wide angular spectrum and when the magnitude of the effective index in the periodic medium is much smaller than the background refractive index – a situation that may often be found in integrated optics. The author hopes that the analysis presented in this work contributes to the general understanding of reflection and refraction of electromagnetic waves in dielectric PhC.

Appendix A

Orthogonality of Bloch modes

Consider the inner product defined by

$$\langle \mathbf{P}(\mathbf{r}), \mathbf{Q}(\mathbf{r}) \rangle = \int_{\mathcal{S}} \mathbf{P}(\mathbf{r}) \cdot \mathbf{Q}^*(\mathbf{r}) d^2\mathbf{r}, \tag{A.1}$$

where $\mathbf{P}(\mathbf{r})$ and $\mathbf{Q}(\mathbf{r})$ are complex vectorial functions, $*$ denotes complex conjugate, and $\mathcal{S}$ is an infinite two-dimensional region in which the two vectorial functions exist. In what follows, it is shown that two Bloch-modes with distinct Bloch-vectors, $\mathbf{k}$ and $\mathbf{k}'$, are orthogonal under the inner product defined above. The two Bloch modes are described by the following expressions:

$$\begin{aligned} \mathbf{P}(\mathbf{r}; \mathbf{k}) &= \sum_{\mathbf{G}} \mathbf{U}_{\mathbf{G}}^{(n)} \exp(j\,[\mathbf{G} + \mathbf{k}] \cdot \mathbf{r}) \\ \mathbf{Q}(\mathbf{r}; \mathbf{k}') &= \sum_{\mathbf{G}'} \mathbf{U}_{\mathbf{G}'}^{(m)} \exp(j\,[\mathbf{G}' + \mathbf{k}'] \cdot \mathbf{r}), \end{aligned} \tag{A.2}$$

where $\mathbf{U}_{\mathbf{G}}^{(n)}(\mathbf{k})$ is the Fourier-coefficient function of the n-th band. Substituting Eqs. (A.2) in Eq. (A.1), one finds

$$\begin{aligned} \langle \mathbf{P}(\mathbf{r}; \mathbf{k}), \mathbf{Q}(\mathbf{r}; \mathbf{k}') \rangle &= \sum_{\mathbf{G},\mathbf{G}'} \mathbf{U}_{\mathbf{G}}^{(n)}(\mathbf{k}) \cdot \mathbf{U}_{\mathbf{G}'}^{*(m)}(\mathbf{k}') \int_{\mathcal{S}} \exp(j\,[\mathbf{G} - \mathbf{G}' + \mathbf{k} - \mathbf{k}'] \cdot \mathbf{r}) d^2\mathbf{r} \\ &= \sum_{\mathbf{G},\mathbf{G}'} \mathbf{U}_{\mathbf{G}}^{(n)}(\mathbf{k}) \cdot \mathbf{U}_{\mathbf{G}'}^{*(m)}(\mathbf{k}') \delta\left(\mathbf{G}' - \mathbf{G} + \mathbf{k}' - \mathbf{k}\right), \end{aligned} \tag{A.3}$$

where the function $\delta(\cdot)$ is the Dirac delta function, which is undefined at the origin.

First we notice that since both $\mathbf{G}$ and $\mathbf{G}'$ are reciprocal lattice vectors their difference is also a reciprocal lattice vector. Furthermore, because $\mathbf{k}$ and $\mathbf{k}'$ are both wave vectors in the 1BZ, their difference coincides with a reciprocal lattice vector only when $\mathbf{k} = p\,\mathbf{g}/2$ and $\mathbf{k}' = -\mathbf{k}$, where $\mathbf{g}$ represents any of the two primitive vectors of the reciprocal lattice and p is an integer. However, $\mathbf{k} = p\,\mathbf{g}/2$ is the Bragg condition, for which modes are forbidden inside the crystal (i.e., all the energy of the Bloch-mode associated with $\mathbf{k}$ is coupled back to the Bloch-mode associated with $\mathbf{k}'$). Therefore, the argument of $\delta(\cdot)$ in Eq. (A.3) vanishes if, and only if, the following two equations are satisfied,

$$\begin{aligned} \mathbf{G} - \mathbf{G}' &= 0 \\ \mathbf{k} - \mathbf{k}' &= 0. \end{aligned} \tag{A.4}$$

From these conditions, it follows that Eq. (A.3) can be written as

$$\begin{aligned} \langle \mathbf{P}(\mathbf{r};\mathbf{k}), \mathbf{Q}(\mathbf{r};\mathbf{k}')\rangle &= \sum_{\mathbf{G},\mathbf{G}'} \mathbf{U}_{\mathbf{G}}^{(n)}(\mathbf{k}) \cdot \mathbf{U}_{\mathbf{G}'}^{*(m)}(\mathbf{k}')\delta_{\mathbf{G},\mathbf{G}'}\delta\left(\mathbf{k}-\mathbf{k}'\right) \\ &= \sum_{\mathbf{G}} \mathbf{U}_{\mathbf{G}}^{(n)}(\mathbf{k}) \cdot \mathbf{U}_{\mathbf{G}}^{*(m)}(\mathbf{k}')\delta\left(\mathbf{k}-\mathbf{k}'\right) \\ &= A^{(n,m)}(\mathbf{k},\mathbf{k}')\,\delta\left(\mathbf{k}-\mathbf{k}'\right), \end{aligned} \tag{A.5}$$

which indicates that the two Bloch modes are orthogonal with $A^{(n,m)}(\mathbf{k},\mathbf{k}')$ being the orthogonality constant for the orthogonality condition. However, notice that the orthogonality does not imply that the Fourier-coefficient functions are orthogonal as well.

Appendix B

Brillouin zone maps

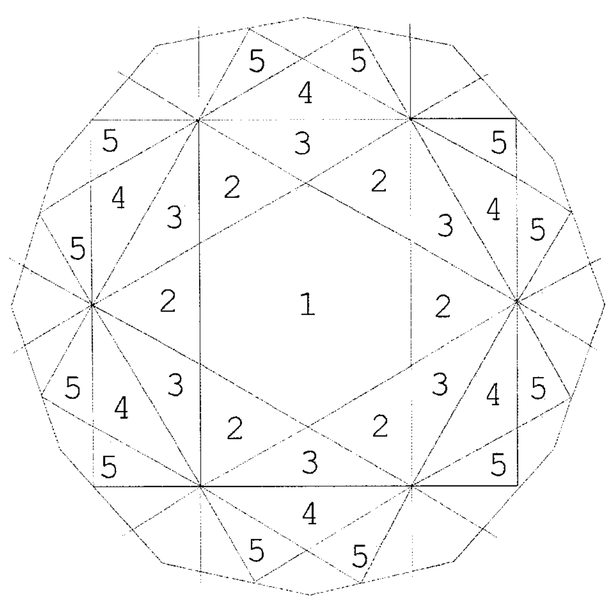

Figure B.1: The first seven Brillouin zones of the hexagonal lattice. The sixth and seventh BZs are not labeled.

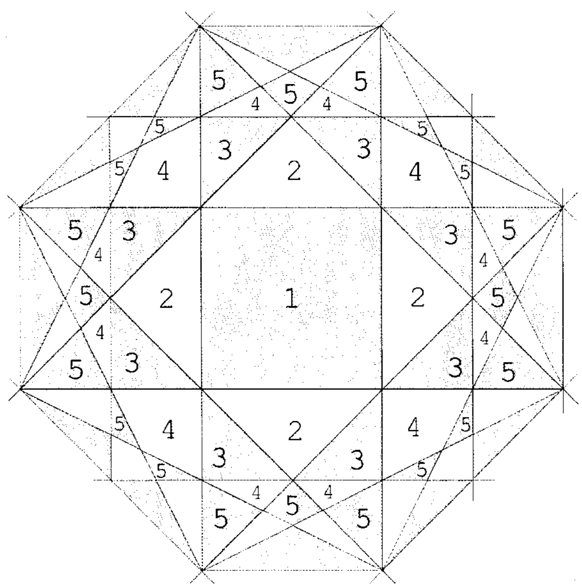

Figure B.2: The first seven Brillouin zones of the square lattice. The sixth and seventh BZs are not labeled.

Bibliography

[1] A. A. Oliner, "Periodic structures and photonic-band-gap terminology: historical perspectives," 29th European Microwave conference, Munich 1999.

[2] K. Ohtaka, "Energy band of photons and low-energy photon diffraction," Phys. Rev. B, Vol. 19, pp: 5057 (1979).

[3] J. Korringa, "On the calculation of the energy of a Bloch wave in a metal," Physica (Utrecht), Vol. 35, pp: 392, (1947).

[4] W. Kohn and N. Rostoker, "Solution of the Schrdinger Equation in Periodic Lattices with an Application to Metallic Lithium" " Phys. Rev. Vol. 94, pp: 1111 (1954).

[5] E. Yablonovitch, "Inhibited spontaneous emission in solid-state physics and electronics," Phys. Rev. Lett., Vol. 58, 2059, (1987).

[6] S. John, "Strong localization of photons in certain disordered dielectric superlattices," Phys. Rev. Lett., Vol. 58, 2486, (1987).

[7] E. Chow, S. Y. Lin, S. G. Johnson and J. D. Joannopoulos, "Quantitative analysis of bending efficiency in photonic-crystal waveguide bends at $\lambda = 1.55\mu$m wavelengths," Optics Lett., Vol. 26, pp: 286, (2001).

[8] A. Chutinan, M. Okano, and S. Noda, "Wider bandwidth with high transmission through waveguide bends in two-dimensional photonic crystal slabs," App. Phys. Lett., Vol. 80, 1698, (2002).

[9] M. Augustin, H.J. Fuchs, D. Schelle, E.B. Kley, S. Nolte, and A. Tnnermann, "High efficiency waveguide bends in photonic crystals with a low in-plane index contrast," Optics Express, Vol. 11, pp: 3284, (2003).

[10] M. Notomi, A. Shinya, S. Mitsugi, E. Kuramochi, and H-Y. Ryu "Waveguides, resonators and their coupled elements in photonic crystal slabs," Optics Express, Vol. 12, pp: 1551, (2004).

[11] O. Painter, R. K. Lee, A. Scherer, A. Yariv, J. D. OBrien, P. D. Dapkus, and I. Kim, "Two-Dimensional Photonic Band-Gap Defect Mode Laser," Science, Vol. 284, pp: 1819, (1999).

[12] S.Y. Lin, V.M. Hietala, L.Wang, and E.D. Jones, "Highly dispersive photonic band-gap prism," Optics Lett., Vol. 21, pp:1771, (1996).

[13] H.Kosaka "Superprism phenomena in photonic crystals," Phys. Rev. B., Vol. 58, pp:10096, (1998).

[14] M. Notomi, "Theory of light propagation in strongly modulated photonic crystals: Refractionlike behavior in the vicinity of the photonic band gap," Phys. Rev. B, Vol. 62, 10696, (2000).

[15] S. Foteinopoulou, and C.M. Soukoulis, "Negative refraction and left-handed behavior in two-dimensional photonic crystals," Phys. Rev. B, Vol. 67, 235107, (2003).

[16] C. Luo, S.G. Johnson, and J.D. Joannopoulos, "Subwavelength imaging in photonic crystals," Phys. Rev. B, Vol. 68, 045115 (2003).

[17] E. Cubukcu, K. Aydin, E. Ozbay, S. Foteinopolou, and C.M. Soukoulis, "Subwavelength Resolution in a Two-Dimensional Photonic-Crystal-Based Superlens," Phys. Rev. Lett., Vol. 91, 207401 (2003).

[18] H.Kosaka, "Self-collimating phenomena in photonic crystals," Phys. Rev. Lett., Vol. 74, pp: 1212, (1999).

[19] H. Kosaka, T. Kawashima, A. Tomita, T. Sato, and S. Kawakami "Photonic-crystal spot-size converter," Appl. Phys. Lett., Vol. 76, pp: 268, (2000).

[20] S. Shi, A. Sharkawy, C. Chen, D. M. Pustai, and Dennis W. Prather, " Dispersion-based beam splitter in photonic crystals," Optics Lett., Vol. 29, pp: 617, (2004).

[21] S. J. McNab, N. Moll, and Y. A. Vlasov, " Ultra-low loss photonic integrated circuit with membrane-type photonic crystal waveguides," Optics Express, Vol. 11, pp: 2927, (2003).

[22] N.W. Ashcroft and N.D. Mermin. *Solid State Physics*, Brooks/Cole, 1976.

[23] K. Sakoda. *Optical Properties of Photonic Crystals*, Springer, 2001.

[24] K.M. Ho, C.T. Chan, and C.M. Soukoulis, "Existance of a photonic gap in periodic dielectric structures," Phys. Rev. Lett., Vol. 65, 3152 (1990).

[25] H.S. Souzer, J.W. Haus, and R. Inguva, "Photonic bands: Convergence problems with the plane-wave method," Phys. Rev. B,, Vol. 45, 13962 (1992).

[26] R.D.Meade, A.M.Rappe, K.D.Broomer, and J.D. Juannopoulos "Accurate theoretical analysis of photonic band-gap materials," Phys. Rev. B,, Vol. 48, 8434 (1993).

[27] S.G. Johnson and J.D. Joannopoulos, "Block-iterative frequency-domain methods for Maxwell's equations in a planewave basis," Optics Express, Vol. 8, pp: 117 (2000).

[28] D. Hermann, M. Frank, K. Busch, and P. Wolfle, "Photonic band structure computations," Optics Express, Vol. 8, pp: 167 (2001).

[29] S. Guo and S. Albin, "Simple plane wave implementation for photonic crystal calculations," Optics Express, Vol. 11, pp: 167 (2003).

[30] E. Yablonovitch, T.J. Gmitter, and K.M. Leung, "Photonic band structure: The face-centered-cubic case employing nonspherical atoms," Phys. Rev. Lett., Vol. 67, 2295, (1991).

[31] Z.Y. Li, J. Wang, B.Y. Gu, "Creation of partial band gaps in anisotropic photonic-band-gap structures," Phys. Rev. B., Vol. 58, pp: 3721 (1998).

[32] A. Yariv and P. Yeh. *Optical Waves in Crystals*, Wiley Interscience, 2003.

[33] M. Born and E. Wolf. *Principles of Optics*, Cambridge (7th Edition), 1959.

[34] H.T.Chien, and Z.Ye, "Negative-refraction-like behavior revealed by arrays of dielectric cylinders," Phys. Rev. E, Vol. 70, 026608 (2004)

[35] L.Wu, M.Mazilu, and T.Krauss, "Beam steering in planar-photonic crystals: From superprism to supercollimation,"IEEE J. of Lightwave Tech., Vol. 21, pp: 561, (2003).

[36] L.Wu, M.Mazilu, T. Karle, and T.Krauss, "Superprism phenomena in planar photonic crystals,"IEEE J. of Quantum Elect., Vol. 38, pp: 915, (2002).

[37] J.Witzens, M. Loncar, and A.Scherer, "Self-collimation in planar photonic crystals,"IEEE J. of Sel. Topics in Quantum Elect., Vol. 8, pp: 1246, (2002).

[38] J.Witzens, and A.Scherer, 'Efficient excitation of self-collimated beams and single Bloch modes in planar photonic crystals," J. Opt. Soc. Am. A, Vol. 20, pp:935, (2003).

[39] X.Yu, and S.Fan, "Bends and splitters for self-collimated beams in photonic crystals," App. Phys. Lett., Vol. 83, 3251, (2003).

[40] D. Labilloy, H. Benisty, C.Weisbuch, T. F. Krauss, D. Cassagne, C. Jouanin, R. Houdre, U. Oesterle, and V. Bardinal, "Diffraction efficiency and guided light control by two-dimensional photonic-bandgap lattices," IEEE J. of Quantum Electronics, Vol. 35, pp.1045 (1999).

[41] E. Popov, B. Bozhkov, and M. Neviere, "Almost perfect blazing by photonic crystal rod gratings," Applied Optics, Vol. 40, pp.2417 (2001).

[42] T. Suzuki and P.K.L. Yu, "Tunneling in photonic band structures," J. Opt. Soc. Am. B, Vol. 12, pp: 804, (1995).

[43] E. Istrate, A. A. Green, and E. H. Sargent, "Behavior of light at photonic crystal interfaces," Phys. Rev. B, Vol. 71, 195122 (2005).

[44] V. Heine, "On the General Theory of Surface States and Scattering of Electrons in Solids," Proc. Phys. Soc. (London), Vol. 81, pp:300 (1963).

[45] R.O. Jones, "Model calculation of surface states in silicon," J. Phys. C: Solid State Phys., pp: 1615, Vol. 5 (1972).

[46] Yia-Chung Chang, "Complex band structure of Zinc-Blende materials," Phys. Rev. B, Vol. 25, pp: 605 (1982).

[47] A. Taflove and S.C. Hagness. *Computational Electrodynamics*, Artech House Publishers, 2000.

[48] K. Srinivasan and O. Painter , 'Momentum space design of high-Q photonic crystal optical cavities," Optics Express, Vol. 10, pp:670, (2002).

[49] K. Srinivasan and O. Painter , 'Fourier space design of high-Q cavities in standard and compressed hexagonal lattice photonic crystals," Optics Express, Vol. 11, pp: 579, (2003).

[50] Z. Zhang and M. Qiu "Small-volume waveguide-section high Q microcavities in 2D photonic crystal slabs," Optics Express, Vol. 12, pp: 3988, (2004).

[51] Y. Akahane, T. Asano, B. Song and S. Noda,"High-Q photonic nanocavity in a two-dimensional photonic crystal," Nature, Vol. 425, pp:944, (2003).

[52] J.P. Berenger, "A perfectly matched layer for absorption of electromagnetic waves," J.Comput.Phys. Vol. 114, pp: 185, (1994).

[53] D.N. Sullivan. *Electromagnetic simulation using the FDTD method*, IEEE Press, 2000.

[54] J.W. Goodman. *Introduction to Fourier Optics*, McGraw Hill (2nd Edition), 1996.

[55] T. Martin, "An improved near- to far-zone transformation for the finite difference time domain method," IEEE Transactions on antennas and propagation, Vol. 46, pp:1263 (1998).

[56] Z.Y. Li, and K.M. Ho, "Light propagation in semi-infinite photonic crystals and related waveguide structures," Phys. Rev. B, Vol. 68, 155101 (2003).

[57] L.C. Botten, T.P. White, C. Martijn de Sterke, R.C. McPhedran, A.A. Asatryan and T.N. Langtry, "Photonic crystal devices modelled as grating stacks: matrix generalizations of thin film optics," Optics Express, Vol. 12, pp:1592 (2004).

[58] L.C. Botten, T.P. White, A.A. Asatryan, T.N. Langtry, C.Martijn de Sterke, and R.C. McPhedran, "Bloch mode scattering matrix methods for modeling extended photonic crystal structures. I. Theory," Phys. Rev. E, Vol. 70, 56606 (2004).

[59] T.P. White, L.C. Botten, C.Martijn de Sterke, R.C. McPhedran, A.A. Asatryan, and T.N. Langtry, "Bloch mode scattering matrix methods for modeling extended photonic crystal structures. II. Applications," Phys. Rev. E, Vol. 70, 56607 (2004).

[60] S. Xiao, M. Qui, Z. Ruan and S. He, "Influence of the surface termination to the point imaging by a photonic crystal slab with negative refraction," App. Phys. Letters, Vol. 85, pp:4269 (2004).

[61] Z. Ruan, M. Qiu, S. Xiao, S. He, and L. Thyln, "Coupling between plane waves and Bloch waves in photonic crystals with negative refraction," Phys. Rev. B, Vol. 71, 045111 (2005).

[62] K. Ohtaka, T. Ueta, and K. Amemiya, "Calculation of photonic bands using vector cylindrical waves and reflectivity of light for an array of dielectric rods," Phys. Rev. B, Vol. 57, pp:2550 (1998).

[63] K. Sakoda, "Transmittance and Bragg reflectivity of two-dimensional photonic lattices," Phys. Rev. B, Vol. 52, pp:8992 (1995).

[64] K. Sakoda, M. Sasada, T. Fukushima, A. Yamanaka, N. Kawai, and K. Inoue, "Detailed analysis of transmission spectra and Bragg-reflection spectra of a two-dimensional photonic crystal with a lattice constant of 1.15 um," J. Opt. Soc. Am. B, Vol. 16, pp:361 (1999).

[65] D. Labilloy, H. Benisty, C. Weisbuch, T. F. Krauss, R.M. De La Rue, V. Bardinal, R. Houdr, U. Oesterle, D. Cassagne, and C. Jouanin, "Quantitative Measurement of Transmission, Reflection, and Diffraction of Two-Dimensional Photonic Band Gap Structures at Near-Infrared Wavelengths," Phys. Rev. Lett., Vol. 79, pp:4147 (1997).

[66] H. Benisty, C. Weisbuch, D. Labilloy, M. Rattier, C. J. M. Smith, T. F. Krauss, R. M. De La Rue, R. Houdre, U. Oesterle, C. Jouanin, and D. Cassagne, "Optical and Confinement Properties of Two-Dimensional Photonic Crystals," J. of Lightwave Tech., Vol. 17, pp.2063 (1999).

[67] Saleh and Teich *Fundamentals of Photonics*, John Wiley and Sons, 1991.

[68] C. Luo, S.G. Johnson, and J.D. Joannopoulos "All-angle negative refraction without negative effective index" Phys. Rev. B, Vol. 65, 201104(R) (2002).

[69] S. Shirai, K. Kimura, Y. Irita, N. Naito, T. Serikawa, S. Kohda, and N. Yamauchi "Optical beam shifter module with high extinction ratio for 1024-input-port optical switching network,"SPIE Photonic Switching, Vol. 1807, pp:328 (1992).

[70] X. Chen and, C.H. Li, "Lateral shift of the transmitted light beam through a left-handed slab," Phys. Rev. E, Vol. 69, 066617 (2004).

[71] K. Noguchi, "Optical Free-Space Multichannel Switches Composed of Liquid-Crystal Light-Modulator Arrays and Birefringent Crystals," J. of Lightwave Tech., Vol. 16, pp:1473 (1998).

[72] S.G. Johnson, S. Fan, P.R. Villeneuve, and J.D. Joannopoulos, "Guided modes in photonic crystal slabs," Phys. Rev. B, Vol. 60, pp:5751 (1999)

[73] R. Ferrini and R. Houdre, "Radiation losses in planar photonic crystals: two-dimensional representation of hole depth and shape by an imaginary dielectric constant," J. Opt. Soc. Am. B, Vol. 20, pp:469 (2003).

[74] J.Witzens, M. Hochberg, T. Baehr-Jones, and A.Scherer, 'Mode matching interface for efficient coupling of light into planar photonic crystals," Phys. Rev. E, Vol. 69, 046609 (2004)

[75] T.Baba and D.Ohsaki, "Interfaces of photonic crystals for high efficiency light transmission," J. App. Phys., Vol. 40, pp:5920 (2001).